Investigations on THM effects in buffer, EDZ and argillaceous host rock

Final Report

Verantwortung für Generationen
Responsibility for Generations

DBE TECHNOLOGY GmbH

Investigations on THM effects in buffer, EDZ and argillaceous host rock

Final Report

Jobmann, M., Breustedt, M., Li, S., Polster, M., Schirmer, S.

DBE TECHNOLOGY GmbH
Eschenstraße 55
D-31224 Peine

November 2013

The research work that is the basis of this report was funded by the German Federal Ministry for Economic Affairs and Energy (BMWi = Bundesministerium für Wirtschaft und Energie) under contract no. FKZ 02E 10086. The authors alone, however, are responsible for the contents of this study.

Table of contents

1 Introduction and objectives

In the Federal Republic of Germany the final disposal of heat-generating radioactive waste in clay formations is investigated as an alternative to the reference concept in a salt formation. The main concern when switching to a clay host rock is the high amount of heat released from the canisters into the clay rock over a long period of time. It is still an open question to what extent the host rock formation is affected by the released heat and if this is a threat to safety.

The released heat from the canisters is a load on the whole barrier system, which consists of the geotechnical barriers (buffer and plugs) and the geological barrier. The temperature has a direct impact on the buffer, the excavative damaged zone (EDZ) and the surrounding host rock. The buffer has specific thermo-physical properties that significantly influence the temperature evolution in the near field so that a temperature load on the buffer is of special concern. Thus, with regard to thermal criteria, the buffer plays a significant role for the design of the emplacement fields. An open question is whether the use of admixtures could enhance the thermo-physical properties so that the heat release into the host rock would be more efficient.

Due to the permanent heat release and the continuous emplacement of additional canisters, the in-situ stress state in the vicinity of the emplacement boreholes continuously varies during the operational period and beyond. It is an open question how the EDZ of emplacement boreholes evolves in the long term with regard to its fissure system and mainly its permeability. A closure of the EDZ and a corresponding decrease in its permeability are necessary to enhance the tightness of the barrier system, especially to avoid a preferential pathway through the EDZ around the openings.

The host rock has specific properties that are necessary to ensure a safe enclosure of the waste. A change in the host rock temperature may change these properties irreversibly. This is especially valid for the most reactive rock components, which are the fine grained clay matrix and the organic components. A high amount of organic compounds is characteristic for clay formations. If the thermal maturation is advanced, an additional artificial heating over longer periods of time may have the effect that the limit where oil generation starts is exceeded. It is still to be clarified whether the heat input from the waste canisters is so high that this limit is exceeded and that oil in an amount worth extracting is generated.

Depending on the pressure and temperature conditions, a mineral transformation or the formation of new minerals may occur, which would change the chemical and mineralogical conditions. Artificial heating could accelerate transformation processes and change the retardation properties of the host rock. Currently, there is no information available about the potential changes of the host rock properties due to the specific heat input of a repository in a clay formation in Germany.

One important task to be performed with regard to the German safety requirements is the demonstration of the integrity of the geotechnical barriers and of the geological barrier. The only way to demonstrate the long-term integrity of the geological barrier is to carry out predictive calculations. These kinds of calculations must have a sound basis of rock-specific constitutive laws together with a well calibrated parameter set that represent the real physical host rock behaviour. To identify suitable constitutive laws and corresponding parameters, in-situ experiments are being performed in the Mt. Terri and Meuse/Haute-Marne URLs in Switzerland and France. These experiments are well equipped with sensing systems that allow a comparison of measured and simulated results for rock parameter identification and corresponding model calibration.

2 Buffer investigations

2.1 Influence of admixtures on thermal bentonite behaviour

According to common repository concepts (Jobmann et al., 2007a), heat-generating radioactive waste is disposed of in purpose-built metal containers that are enclosed by a so-called geotechnical barrier to avoid direct contact with the host rock. The barrier usually consists of clays rich in smectites, e.g. bentonite, which has excellent swelling and thus sealing properties. One disadvantage is the very low thermal conductivity even when highly-compacted. Thus, the heat generated by the radioactive waste dissipates only very slowly.

The thermal conductivity of bentonite increases with increasing water content. The amount of water and water migration in clay stones is very low due to their low permeability, and saturation of the barrier proceeds much more slowly. The initial heat generated directly after disposal, which determines the repository design, will dissipate through the unsaturated barrier corresponding to its thermal properties. Pacovsky et al. (2007) as well as Vašíèek (2007) first tested graphite as an admixture to Czech clays and found it to be useful to enhance thermal conductivity.

The possibilities to accelerate the heat flow through a barrier consisting of bentonite available in Germany and admixtures have been investigated and are described in the following subchapters.

2.1.1 Materials, sample preparation and measurement conditions

One possibility to increase the thermal conductivity of the barrier is the admixture of a material with high thermal conductivity. Graphite seems to be the preferred additive because of its high temperature stability and low chemical reactivity.

The thermal conductivity of natural bentonite usually shows only little response to temperature change. The thermal conductivity of quartz and graphite, however, decrease considerably with increasing temperature. Calcium-Bentonite, Sodium-Bentonite as well as Friedland clay, commercially available quartz sand, and three types of graphite (powder graphite, precious graphite, and graphite flakes) were selected. The grain size of the quartz sand was about 0.3 mm. The bentonite-quartz mixtures were prepared with quartz contents between 0 and 50%. Mixtures with higher quartz content led to problems during sample preparation. Cylindrical samples with a diameter of 30 mm and a thickness of 10 mm were prepared in a cell using a pressure of 15 MPa. The sample preparation was performed under vacuum to avoid closed pores filled with air. The samples were not exactly plane-parallel, so that each sample had to be finished by plane-parallel grinding prior to its installation in the divided bar device. At higher quartz contents quartz grains broke out of the sample surface producing holes that interfered with the heat transfer into and out of the sample and led to incorrect values of thermal conductivity. The bentonite-graphite mixtures were prepared in the same manner with graphite contents between 0 and 95% graphite. Because of its fineness there were no break-outs during plane-grinding.

Six test samples with different bentonite and quartz contents as well as ten test samples with different bentonite and graphite contents were prepared, and the thermal conductivity was measured as a function of temperature between 35 and 150°C. Details of the method applied are described in (Jobmann & Buntebarth, 2009). Each measurement was performed by applying a uniaxial pressure of 2 MPa. Micro-fissures that might have formed during unloading after sample compaction were closed again, thus significantly reducing the contact resistance within the measurement device. This ensured comparable measurement conditions for all test samples.

During the measurements, all test samples released the free or adhesively bound water with a maximum of 6% weight loss. The water release decreased linearly with increasing admixture content and together with the applied pressure, the sample thickness was reduced by a maximum of 3% which was taken into account when determining the thermal conductivity.

2.1.2 Properties of individual materials

To prepare a suitable mixture of the selected materials, the first step was to determine the thermal properties of the pure components using samples prepared under the same conditions as the mixtures. As described above, this was not possible for pure quartz sand due to sample preparation problems. Conductivity values for quartz up to about 10 $Wm^{-1}K^{-1}$ were reported (MolTech 2008) and thus, a considerable influence on the conductivity of mixtures was assumed. As expected, the thermal conductivity of graphite is much higher than those of the different types of bentonite and the clay. In addition, the thermal conductivity of the precious graphite was five times higher than those of the bentonites and Friedland clay, but only about 50% of that of the graphite flakes (Fig. 2-1).

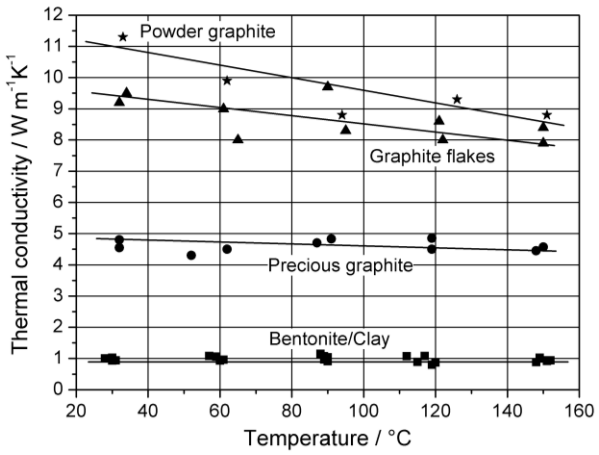

Fig. 2-1: Thermal conductivities as a function of temperature of three different kinds of graphite compared with values of bentonite.

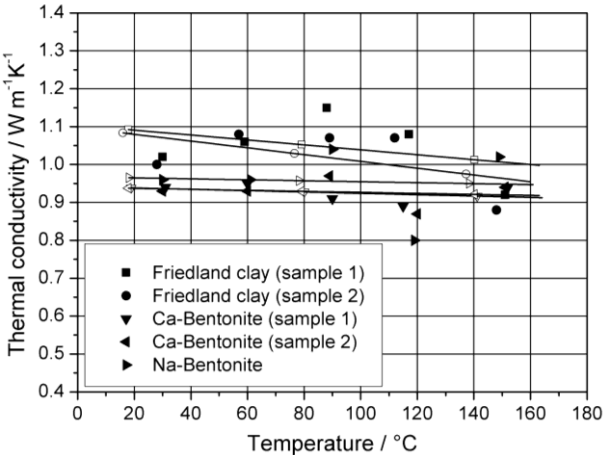

Fig. 2-2: Thermal conductivities of Ca-Bentonite, Na-Bentonite, and Friedland clay samples as a function of temperature.

The dependence on temperature increases at higher levels of thermal conductivity (Fig. 2-1). The thermal conductivity of powder graphite decreases between 20 and 100°C by about 20%. Almost no temperature dependence was observed for the bentonites (Fig. 2-2), and only a very small dependence for the Friedland clay. Since powder graphite yields the highest thermal conductivities and the calcium-bentonite shows the smallest scattering of the measured values, both materials were selected for further investigations.

2.1.3 Properties of bentonite-quartz mixtures

The thermal conductivity of the bentonite-quartz mixtures slightly increases with increasing quartz content (Fig. 2-3, Fig. 2-4). At a quartz content of 50%, the thermal conductivity is increased by a factor of only about 1.5. The observed decrease of thermal conductivity at increasing temperature remains more or less the same at all levels of thermal conductivity. The temperature dependence can be described as

$$\lambda^{-1} = A + BT \qquad (2\text{-}1)$$

Tab. 2-1: Coefficients for Eq. (1)

Quartz Content [%]	A [m K W^{-1}]	B [10^{-3} m W^{-1}]
5	0.95	0.75
10	0.86	0.44
10	0.84	0.39
15	0.82	0.83
20	0.82	0.57
30	0.82	0.54
50	0.70	0.41
50	0.67	0.73

The scattering of the measurements is mainly due to the water release during the measurements. The coefficients A and B of equation (1) are given in Table 1. Measurement of parallel samples with 10 and 50% quartz indicated good reproducibility. The increase in thermal conductivity with the quartz content was not linear (Fig. 2-4).

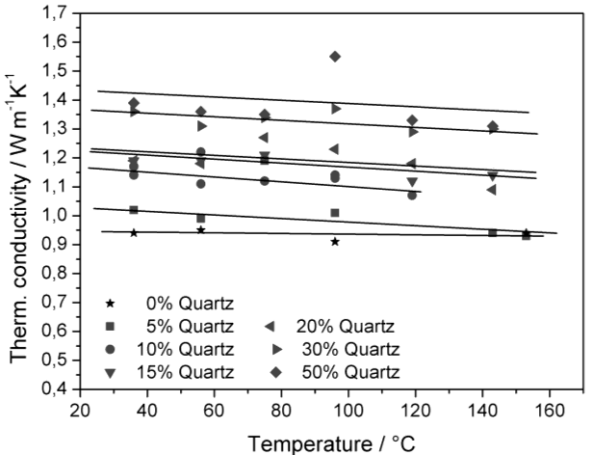

Fig. 2-3: Thermal conductivity of test samples with different quartz contents as a function of temperatures between 35 and 150°C.

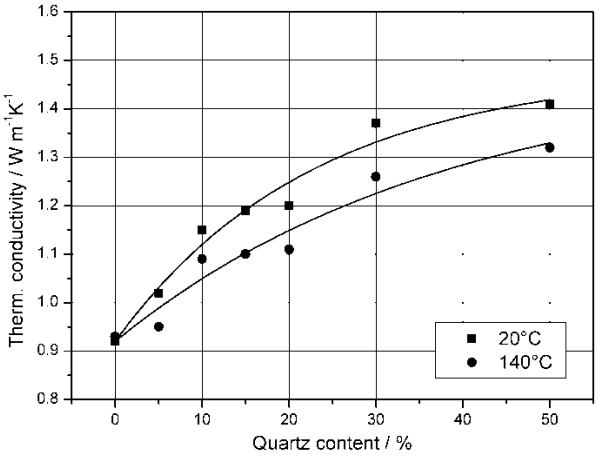

Fig. 2-4: Thermal conductivity of test samples at temperatures of 20 and 140°C as a function of quartz content.

The values at 20°C and 140°C were calculated using Equation (2-1) with the coefficients given in Table 2-1. For the dependence of the thermal conductivity λ_{bq} [$Wm^{-1}K^{-1}$] on the quartz content n_q [%], the following relationship was found:

$$\lambda_{bq} = \lambda_0 + 2t_1 * (1 - \exp(-n_q / t_2)) \tag{2-2}$$

where λ_0 is the value for pure bentonite, t_1 = 0.28 is an empirical constant and t_2 is the temperature-dependent parameter. Referring to Fig. 2-3, the temperature dependence is linear and therefore t_2 was found to be:

$$t_2 = a_1 + a_2 T \tag{2-3}$$

Where a_1 = 0.13 and a_2 = 19.3 are empirical constants.

2.1.4 Properties of bentonite-graphite mixtures

As for the bentonite-quartz mixtures, the thermal conductivity increases with increasing graphite content, but more steeply (Fig. 2-5). While the temperature dependence of the thermal conductivity of bentonite-sand mixtures does not vary with composition, it varied strongly with increasing graphite content, since graphite has a strong temperature dependence of thermal conductivity. The higher the graphite content, the stronger the decrease in thermal conductivity with increasing temperature. Within the investigated temperature range, the measured values were fitted by a linear function according to equation (1). The coefficients are given in Tab. 2-2.

Tab. 2-2: Coefficients for Eq. (1)

Graphite Content [%]	A [m K W^{-1}]	B [10^{-3} m W^{-1}]
5	0.699	0
10	0.460	3.67
20	0.299	1.88
30	0.167	3.27
50	0.0944	3.14
80	0.0770	3.31
95	0.0775	2.77

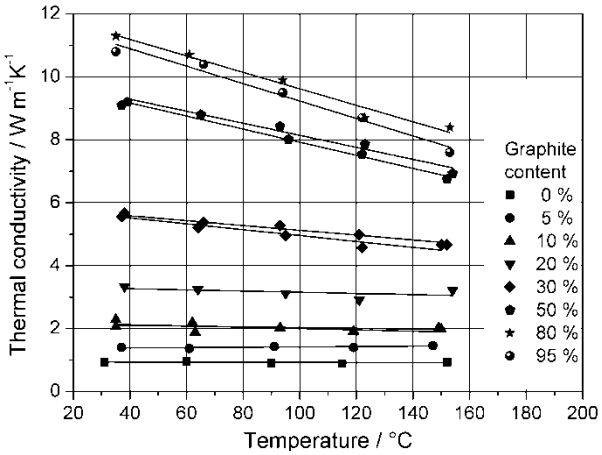

Fig. 2-5: Thermal conductivity as a function of temperature of test samples with different graphite contents between 35 and 150°C.

The relation between thermal conductivity at 20°C and graphite content was non-linear, especially at higher graphite contents (Fig. 2-7). Between 20 to 50% graphite content the thermal conductivity is most sensitive to changing graphite content and the relation can be considered as quasi-linear. Every sample has a different water content due to the water-bearing bentonite and the water-free graphite which contains only small amounts of adsorbed water on grain surfaces. Thus, the water content decreases with increasing graphite content (Fig. 2-6). The water content decreases from 8.4 to 0.1% between 5 and 95% graphite.

The density of the samples varies due to the lower density of the bentonite. Also, the particle arrangement and thus the structure were different for each mixture compacted at the same compaction pressure. The density of the samples varied between 2200 and 2010 kg m^{-3} at graphite contents between 5 and 95% (Fig. 2-6).

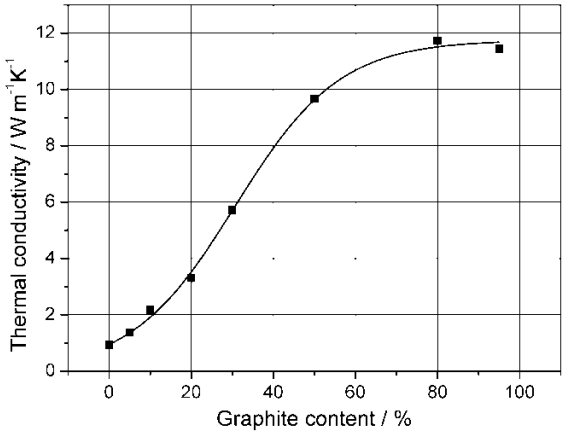

Fig. 2-6: Thermal conductivity of test samples at a temperature of 20°C as a function of graphite content. The samples were compacted at 150 MPa each.

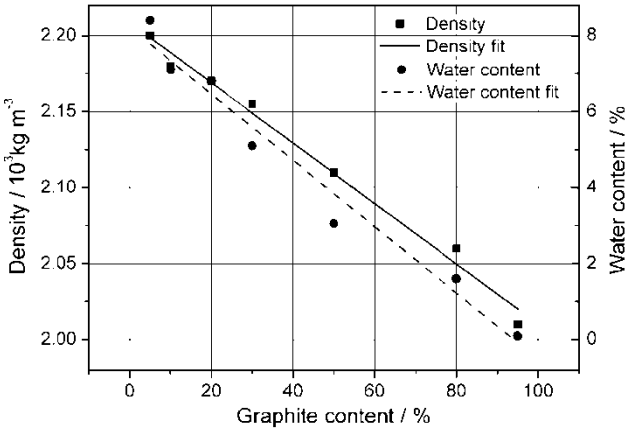

Fig. 2-7: Density and water content of the different test samples as a function of graphite content.

Using the curve from Figure 2-7, the dependence of thermal conductivity of bentonite-graphite λ_{bg} [$Wm^{-1}K^{-1}$] on the graphite content n_g [%] can be described as:

$$\lambda_{bg} = c_1 / (1 + \exp(-c_2 * (n_g - c_3))) \quad (2\text{-}4)$$

with c_1 = 11.74, c_2 = 0.079, and c_3 = 30.74 as empirical constants.

2.1.5 Reference mixture

As part of a newly developed final disposal concept for heat-generating radioactive waste in clay formations in Germany (Jobmann et al., 2007b), the geotechnical isolation barrier has been assumed to have at least the same thermal conductivity as the host rock. One possible clay formation in Germany is the so-called Opalinus clay, which has been investigated quite thoroughly by Nagra (Nagra, 2002). The mean value of thermal conductivity has been found to be 2.5 $Wm^{-1}K^{-1}$. For this reason a reference mixture of bentonite and graphite was selected from Figure 2-7 that had a graphite content of about 15%. Using this mixture, additional test samples were prepared and measured. The reference mixture contained 85% Ca^{2+}-bentonite and 15% graphite. The thermal conductivity determined as a function of temperature, water content, and density (and thus the degree of compaction) is shown in Fig. 2-8 to Fig. 2-10.

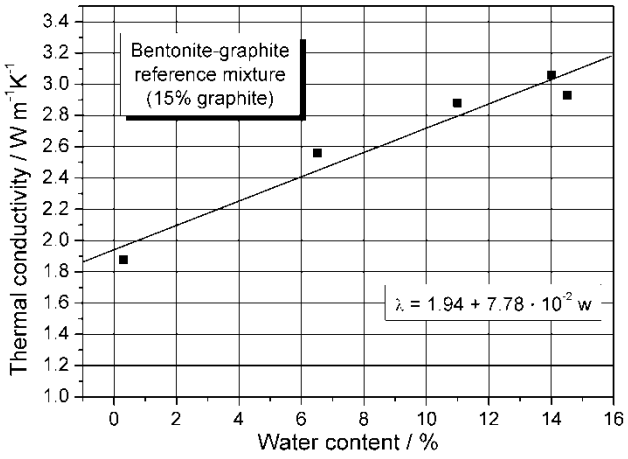

Fig. 2-8: Thermal conductivity of reference samples (85% bentonite, 15% graphite) as a function of water content.

In order to get samples with various water contents, the Ca^{2+}-bentonite was exposed to water-saturated air for one or several days. The hydrated bentonite was mixed with graphite, compacted at 150 MPa and the properties were determined immediately. The water content was calculated from the mass loss at 150°C. Suitable samples could be prepared up to a water content of about 14%. At higher water content, the samples became plastic, and a suitable compaction could not be achieved. The relationship of thermal conductivity λ [$Wm^{-1}K^{-1}$] and water content w [%] was linear as expected (Fig. 2-8) and can be described by equation (5), for water contents between 0 and 14%:

$$\lambda = 1.94 + 7.78 \cdot 10^{-2}\, w \qquad (2\text{-}5)$$

The temperature dependence of the thermal conductivity of a 15% admixture sample is shown in Fig. 2-9.

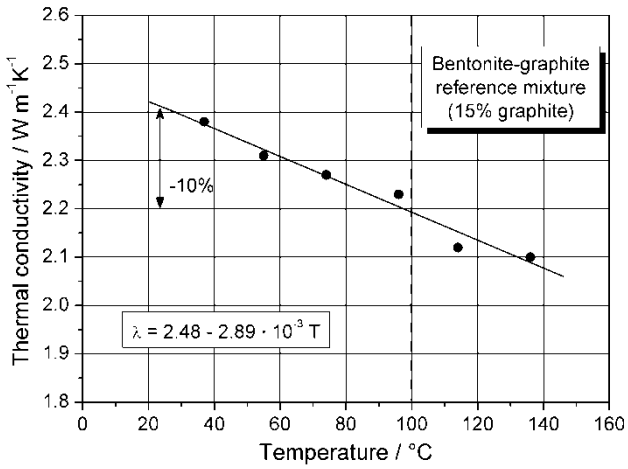

Fig. 2-9: Thermal conductivity of a reference sample (85% bentonite, 15% graphite) as a function of temperature.

The decrease in thermal conductivity with increasing temperature is similar to the previous results (Fig. 2-5). In the range between 20 and 100°C, the thermal conductivity decreases by about 10%. The linear relationship between λ [$Wm^{-1}K^{-1}$] and T [°C] is described by equation (6), valid between 20 and 140°C:

$$\lambda = 2.48 - 2.89 \cdot 10^{-3}\, T \qquad (2\text{-}6)$$

Important for the thermal design of a geotechnical barrier is the dependence of thermal conductivity on pre-compaction and thus on density. For this purpose, the thermal conductivity as well as the density were determined as a function of applied pressure. From both functions, the relation between thermal conductivity and density was calculated (Fig. 2-10). The relation is non-linear and λ

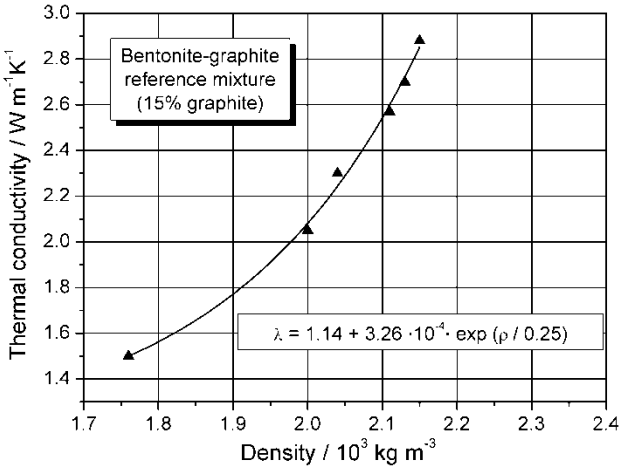

Fig. 2-10: Thermal conductivity of a reference sample (85% bentonite, 15% graphite) as a function of density.

[W $m^{-1}K^{-1}$] can be calculated by equation (7) as a function of density ρ [kg m^{-3}] valid between 1700 and 2200 kg m^{-3}.

$$\lambda = \lambda_0 + c_1 \cdot \exp(\rho/c_2) \qquad (2\text{-}7)$$

with λ_0 = 1.14 [$Wm^{-1}K^{-1}$], c_1 = 3.26 10^{-4}, c_2 = 0.25

All relationships found were combined to be used for a thermal design of engineered geotechnical barriers as follows:

$$\lambda = \lambda_{bg} + 3.26 \cdot 10^{-4} \cdot \exp((\rho-\rho_0)/\ 0.25) - 2.89 \cdot 10^{-3}\ (T-T_0) + 7.78 \cdot 10^{-2}\ (w-w_0) \qquad (2\text{-}8)$$

with λ_{bg} taken from equation (4). The other terms describe the change of thermal conductivity due to variation in density, temperature, and water content.

2.2 Influence of swelling pressure on buffer stress evolution

Within the framework of the Temperature Buffer Test (TBT) at the Äspö URL in Sweden, where two electrically heated canisters were installed in a vertical borehole and surrounded by a bentonite and sand-bentonite buffer (Akesson, 2012). The mechanical behaviour of the bentonite buffer was investigated with a focus on the bentonite swelling. The thermo-hydraulic buffer evolution has already been investigated in earlier work (Yildizdag et al., 2008). Coupled thermo-hydro-mechanical simulations with swelling according to Grob's Law (Konietzky, 2000) were performed using the FLAC3D (Itasca, 2000) code. The significance of the model parameters was evaluated by means of a global sensitivity analysis. Based on the most significant parameters, an automatic model calibration was performed using the software "optiSlang", which allows numerical sensitivity studies for non-linear problems using optimized stochastic sampling strategies. Details can be found in (Dynardo, 2010; Will, 2006). The software is able to offer a sampling-based sensitivity analysis to identify important parameters, to quantify their influence and to generate a so-called "best design" in comparison with measurement results taken in-situ. In Fig. 2-11 the workflow for parameter calibration is illustrated. optiSlang acts as controlling software that generates FLAC3D runs by itself by automatically changing the input parameters based on given ranges.

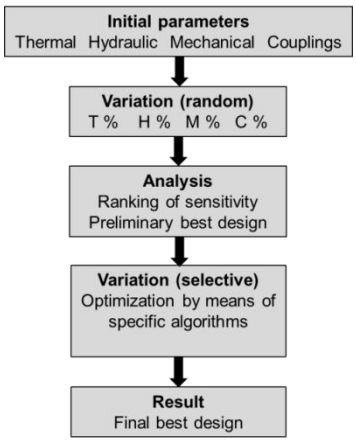

Fig. 2-11: Workflow for parameter calibration used by optiSlang.

2.2.1 Model description

The model covers one axisymmetric segment of the borehole and the surroundings, which is equivalent to a 2D axisymmetric model. The model domain, the dimensions, and discretization are shown in Figure 2-12. In the vicinity of the heaters, the discretisation is fine (node spacing ~0.1m within a radius of 5m), and the zone size increases with increasing distance to the heaters. The figure also shows also the materials used. Tab. 2-3 lists the mechanic, thermal and hydraulic constitutive models assigned to the different materials in the FLAC

model. The Äspö diorite host rock as well as the heater and buffer system are modelled assuming a simple elastic mechanical behaviour.

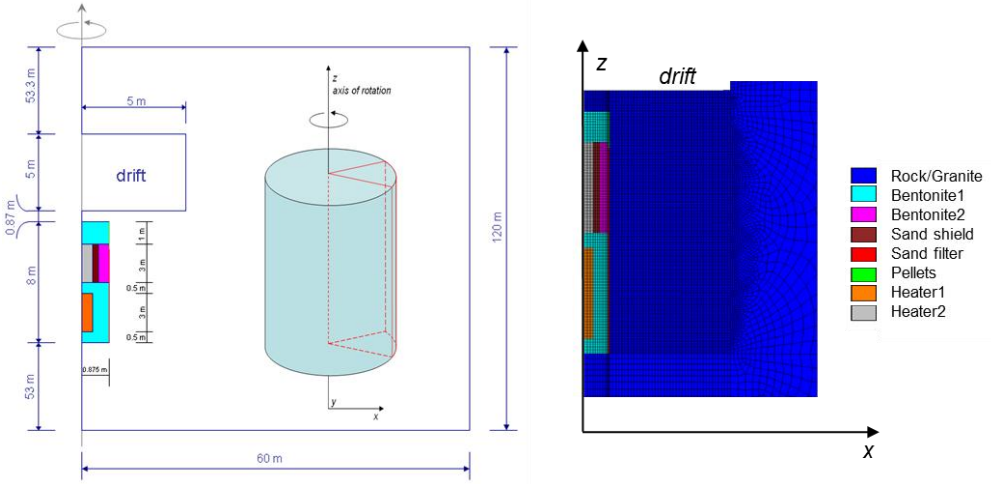

Fig. 2-12: Model domain, dimension (red border, left), and discretization (56350 zones, left)

For the bentonite buffer, the total strain ε is a superposition of elastic strain and swelling strain:

$$\varepsilon = \varepsilon_s + \varepsilon_e \tag{2-9}$$

The heat conduction is isotropic for all materials. Water tightness is assumed for the diorite host rock and the heaters; hence, no flow model is applied to these materials. For the remaining materials, isotropic fluid flow is applied.

Tab. 2-3 Consititutive models

Material	Mechanic	Thermal	Hydraulic
Äspö diorite	elastic	Isotropic Heat Conduction	No flow
Bentonite1	elastic, swelling		Isotropic Darcy Flow
Bentonite2			
Pellets	elastic		
Sand			
Sand filter			
Heater			No flow

Two different approaches for the swelling strain in the bentonite buffer were tested, both describing the swelling process phenomenologically. Both swelling laws are implemented in FLAC by a FISH-routine. The FISH-routine for the first law was written by Konietzky (2000), the FISH-routine for the second law is an outcome of this project.

One dimensional swelling law of Grob:
According to Grob (1972) the swelling strain is related to the actual compression stress via a logarithmic swelling law:

$$\varepsilon_s = C \cdot log \frac{\sigma_{aktuell}}{\sigma_{max}} \quad ,\sigma_{aktuell} < \sigma_{max}$$
$$\varepsilon_s = \varepsilon_{s,max} \quad ,\varepsilon_s > \varepsilon_{s,max} \tag{2-10}$$

For stresses above σ_{max} the swelling strain is 0. At very low actual stresses the swelling strain ε_s is limited to a maximum value $\varepsilon_{s,max}$ in order to avoid unrealistically high swelling strains. For the sake of simplicity, the swelling is assumed to be isotropic.

Saturation-dependent swelling pressure
According to the swelling pressure tests (Fig. 2-13), the swelling pressure σ_s is directly proportional to the degree of saturation S with σ_{sat} being the swelling pressure at saturation:

$$\sigma_s = S \cdot \sigma_{sat} \tag{2-11}$$

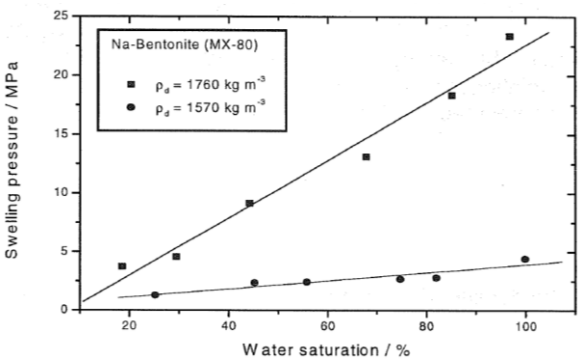

For the initial stress state at the test site, which is located ~460 m below the ground surface, isotropic conditions are assumed: $\sigma_V = \sigma_H = \sigma_h$ = 14 MPa. A significant suction is exerted by the buffer system.

Fig. 2-13: Swelling pressure as a function of the degree of water saturation for Na-Bentonite with different dry densities after Studer et al. (1984) and Börgesson (1995).

As a mechanical boundary condition the movement of gridpoints at the bottom of the model and at the radial plane is prevented by fixing the displacement in all directions to zero. At the heater borehole axis, gridpoints can only move along the z-axis. At the top of the model, the gridpoints are free to move but their behaviour is controlled by the introduced overburden load of ~12.4 MPa. At the tangential model planes a zero normal velocity allows only for a movement within the respective tangential plane. The temperature is fixed to 20°C at all model edges, except for the longitudinal axis of the heater borehole. There, the temperature is free to change. A power of 1500–1600 W was applied to the heaters. The heating scheme is described in (Akesson, 2012).

2.2.2 Preliminary analysis

To get a suitable set of input parameters as initial values, the input parameter should be based on the laboratory measurement results. For each parameter a range has to be specified within which optiSlang is allowed to change the parameter during its analysis. To identify the important parameters for the transient processes and to reduce the overall calculation time, a simulation time of about 200 days was assumed to be adequate for this test of automatic model calibration.

Parameter variation

Table A1.1 in appendix 1 shows the model parameter and the ranges of variation. It is assumed that the values measured for the parameters in the laboratory are rather certain Therefore these parameters were varied only within a small range of 20%. All other parameters were varied within a range of 50%. The fixed heads in the sand filter were varied up to the fixed pressure applied to the lower injection points, assuming that the pore pressure applied to the injection points is spreading quite well in the permeable sand. The lower limit is chosen to be almost double of the atmospheric pressure.

Objective function

The distance between the measured (x_{obs}) and the calculated data (x_{calc}) is evaluated using an objective function, which is the sum of the equally weighted Euclidian distance calculated for selected temperature, radial and axial stress sensors:

$$d(x_{calc}, x_{obs}) = \sqrt{\sum_{i=1}^{n} \left(x_{calc,i} - x_{obs,i}\right)^2} \tag{2-12}$$

In table A1.2 in appendix 1 the sensors selected for parameter identification are listed.

Coefficients of importance

The coefficient of importance (Coi) is a prediction value to explain the influence of a single input parameter (density, thermal conductivity, etc.) on a chosen output parameter (e.g., the measured stress at a single sensor). Depending on the regression model, the Coi is defined by:

$$R^2{}_{-colc,obs} = R^2_{calc} - \frac{\sum_{k=1}^{N}(\gamma^{(k)}(x_{calc}) - \mu x_{obs})^2}{\sum_{k=1}^{N}(x^{(k)}(x_{calc}) - \mu x_{obs})^2} \quad (2\text{-}13)$$

Preliminary results

Fig. 2-14 shows the parameters with the highest influence on the overall objective function. Different parameters are relevant for the single Euclidian distances of the individual temperatures and the stresses:

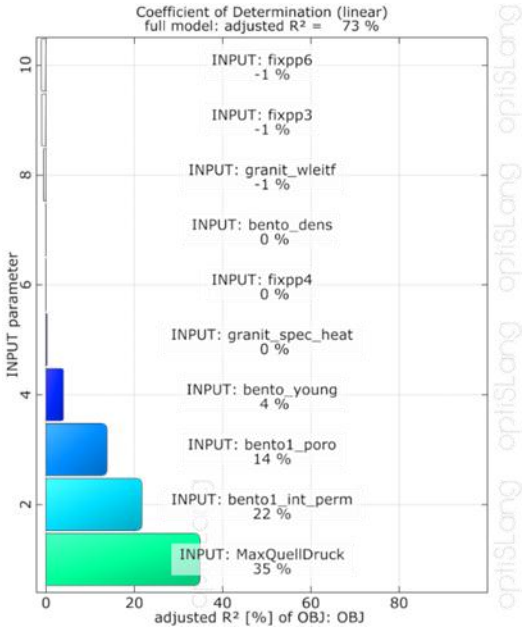

Fig. 2-14: Most influential parameters of the preliminary sensitivity analysis

Stress:
(1) Maximum swelling pressure
(2) Intrinsic permeability bentonite 1
(3) Porosity bentonite 1
(4) Young modulus bentonite
(5) Maximum swelling deformation
(6) Specific heat capacity host rock
(7) Young modulus sand filter
(8) Young modulus sand

Temperature:
(1) Thermal conductivity host rock
(2) Thermal conductivity bentonite
(3) Intrinsic permeability bentonite 1
(4) Porosity bentonite 1
(5) Specific heat capacity host rock
(6) Parameter C of Grob (for swelling law)

The axial stresses at the two sensors named PB217 and PB226 are governed by a different ranking of the relevant parameters. Both sensors were influenced by a saturation that was too low, which changed only after water injection at the upper tubes of the sand filter had begun. This resulted in a particular stress build-up that differed from the stress evolution at the other sensors. The fitting of the measured and the calculated curves was not sufficient. Especially the calculated stresses do not lie within the range of the measured stresses. The correlation of the measured and the calculated curves was quite poor as well.

2.2.3 Final analysis

In view of the unsatisfactory fitting of calculated and measured curves in the first analysis, a second analysis was performed using different parameter ranges and a slightly different modelling of the swelling process. It was supposed that one reason for the very high calculated stresses could be an insufficient simulation of the swelling process. Therefore the range of the Grob's model parameter "Maximum Swelling Pressure" was changed and an additional parameter was introduced, which represents a threshold for the swelling (swell_sat), ensuring that swelling does only take place when the saturation exceeds the initial saturation of the bentonite. The density of the materials was assumed to be known and was therefore not varied during the analysis. Different ranges and corrected initial values for the thermal conductivity were used. The changed parameter set is given in Table A1.3 in the appendix.

Some of the installed stress sensors showed signal characteristics dedicated to physical effects which cannot be reflected by the current model. The measured values varied far from

the calculation results, maybe due to unexplainable effects. For this reason, sensors PB201, PB214, PB218, PB217, PB226 and PB228 were not considered any longer. The remaining sensors are shown in Table A1.4 in the appendix. For the evaluation the same objective function was used as before. 41 calculations were carried out with the new approach.

After the simulation of the swelling process had been repeated, the fit of the calculated stress values improved substantially. The measured values are within the range of the calculation results. Fig. 2-15 (left) shows the results of sensor PB213 before and after the change in swelling pressure simulation. As can be seen in the first view of the calculated values (gray), the measured value (black) for sensor PB213 deviates completely from the distribution of the other values. The deviation is up to 35 MPa. The second view shows the same measured value with the new swelling process. The shape of the measured curve shows a good consistency with the shape of the calculated curve. Even slight fluctuations of the stress are represented in the numerical model as can be seen for example around day 30 or 75. The variance of the input parameters results in an upper limit of the calculated stress at -25 MPa and a lower limit at -2.0 MPa (at 200 days). The other sensors have similar characteristics so that they could be used for the second analysis as well.

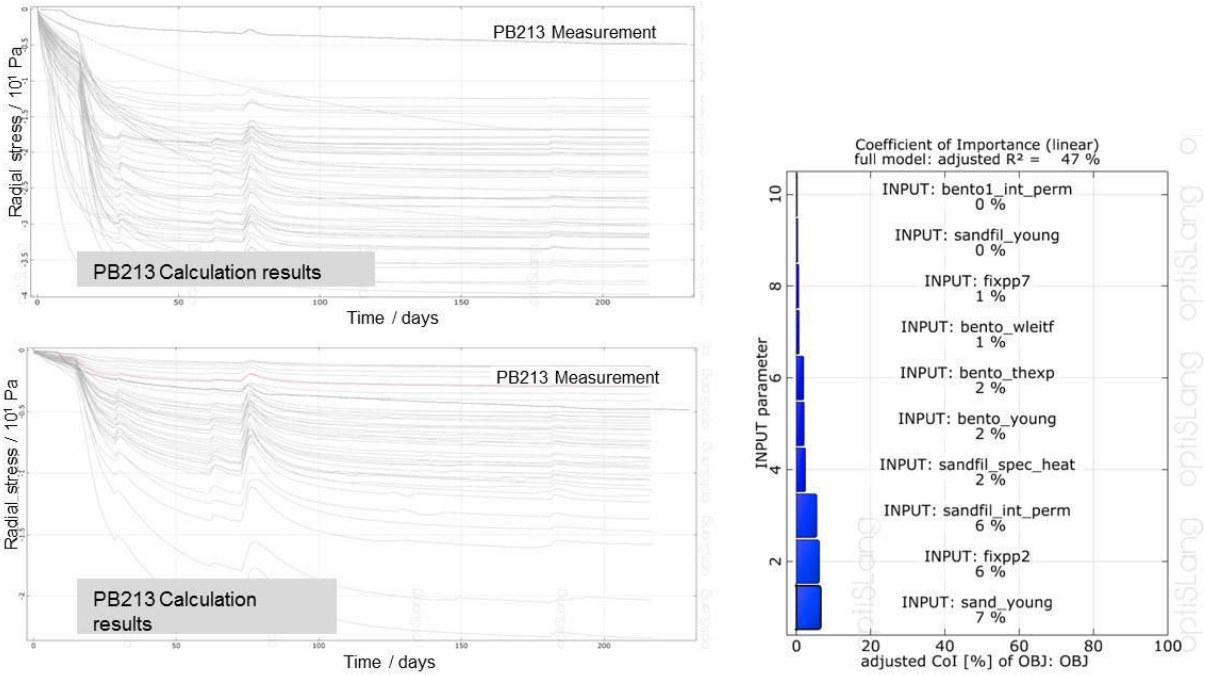

Fig. 2-15: Radial stress at PB213 before and after the change of swelling simulation (left) and most influential parameters of the final analysis (right).

Fig. 2-15 (right) shows the parameters with the most influence on the overall objective function of the second sensitivity analysis. The ability to forecast the model reaction is quite low. Only 47% of the variation of the signals can be explained by correlation to the variation of the input parameters. There is no controlling parameter identified. The most important parameter is the Young's modulus of the sand. Looking at the influence of the sand Young's modulus (Fig. 2-16), not all sensors were influenced. This means that there are other effects that still cannot be explained by the current numerical model. This statement is confirmed when looking at selected sensors. At some sensors, the most important parameter is not the Young's modulus of the sand. One example is given below (Fig. 2-17). The graphic on the right shows the measured axial stress for sensor PB208 and the results of the calculation. The chart on the left shows the coefficient of importance for this sensor. As can be seen, the decisive parameter is not the Young's modulus of the sand but the fixed pore pressure in the sand. The "Coefficients of Importance" for the Young's modulus of the sand for sensor PB208 is equal to zero.

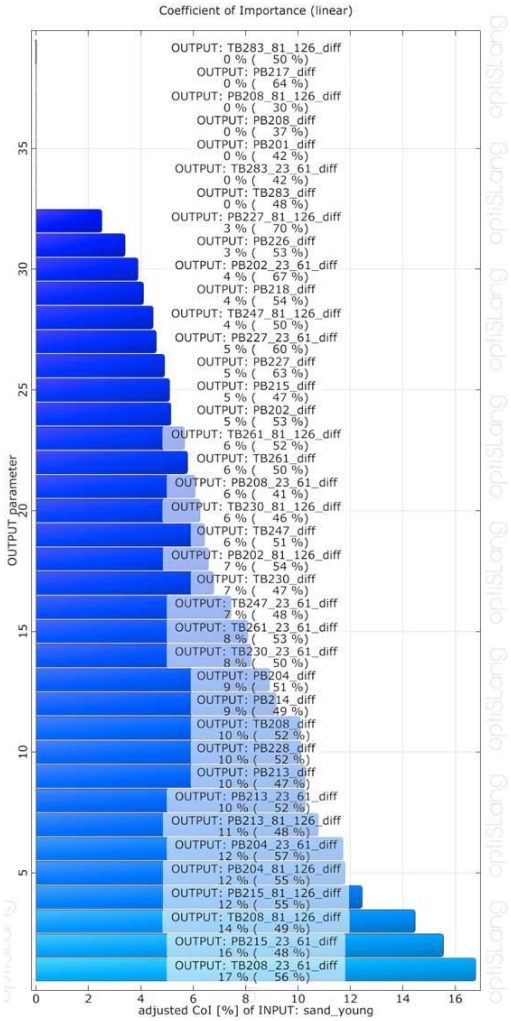

Different decisive parameters have been identified for all sensors and especially for the stress sensors. They are listed in Tab. 2-4. What becomes obvious is that the Young's modulus of the sand can only be clearly identified as a sensitive parameter for the temperature sensors (TBs). For the stress sensors, no clear assignment of a sensitive parameter is pos-possible. This confirms the hypothesis that not all of the physical effects can be explained by the current numerical model.

Tab. 2-4: CoI of the sensors considered (most important parameters)

Sensor	Parameter	CoI [-]	Ability to forecast R^2 [%]
TB208	Young's modulus sand	10	52
TB230	Young's modulus sand	7	47
TB247	Young's modulus sand	6	51
TB261	Young's modulus sand	6	50
TB283	Young's modulus sand	8	48
PB208	Fixed pore pressure boundary Sand 1	8	37
PB227	Thermal Exp. Coeff. Bentonite	15	47
PB202	Heat Conductivity Granite	7	53
PB204	Thermal Exp. Coeff. Bentonite	9	51
PB213	Young's modulus sand	10	47
PB215	Thermal Exp. Coeff. Bentonite	8	47

Fig. 2-16: Influence of the sand young modulus to the output functions

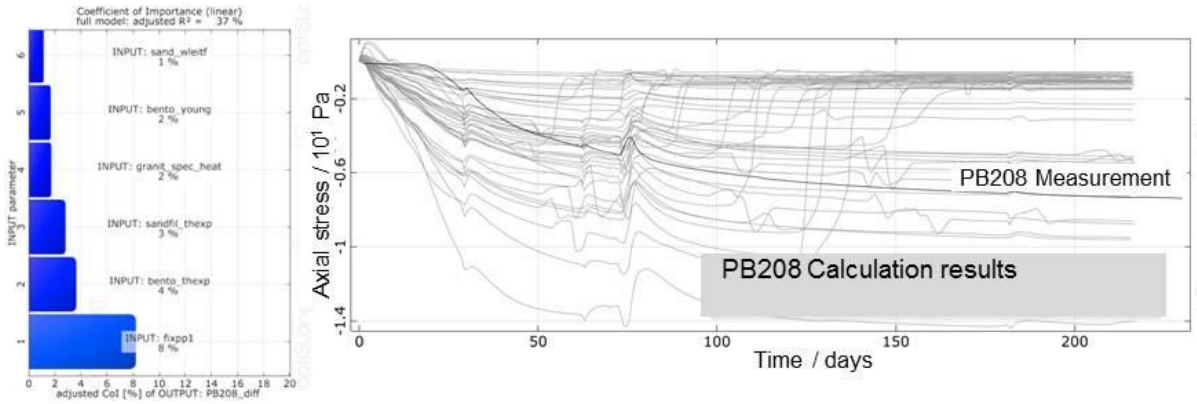

Fig. 2-17: Coefficient of Importance and axial stress at PB208

As a result of the analysis a best design parameter set was identified. (Appendix 1, Figure A1.1). The simulation of the stress has improved with the use of the new way of modelling the swelling process. After excluding the sensors that did not show effects that could be rep-resented by the model, all measured values lay in the centre of the variation range of the calculation results. The parameters identified for the best design are within the predefined lower and upper boundaries of the parameter range. Some parameters are in the upper and lower 10% limits of the variation but they still do not reach the maximum or minimum value. This confirms that the assumed range of the parameters is suitable. The models's qualitative representation of the radial stress over time by the model is more or less sufficient. The model values of the radial stress represent the failures of the heater shown in the measured

values (Fig. 2-18). In case of a failure, the stress decreased. This effect is adequately represented by the model while the stress development up to 200 days is underestimated. An exception is sensor PB204 where the calculated stress is too high. The deviation between measured and calculated values varies between 1.25 MPa (sensor PB204) and 2.85 MPa (sensor PB213).

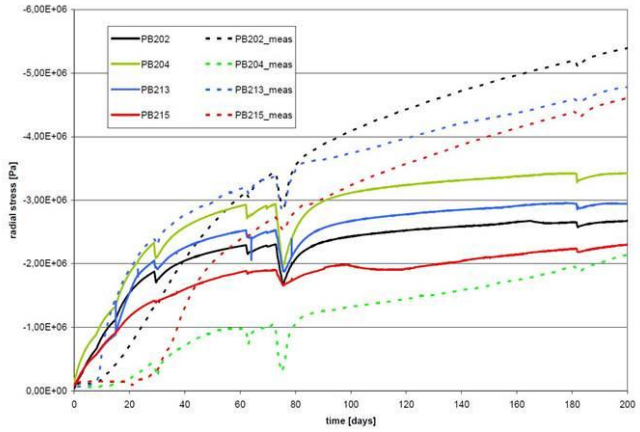

Fig. 2-18: Considered radial stress sensors, measurement vs. calculation

The analysis of the two remaining sensors for the measurement of the axial stress is difficult. Fig. 2-19 shows the comparison of sensor PB208 and PB227. The failure of the heater around day 73 causes a decrease in stress in the measured values of sensor PB208. This effect is not well represented in the calculation. The calculated stress at the time of 200 days is underestimated by about 5 MPa. Contrary to expectations, sensor PB227 shows a major increase in stress from day 60 to day 73. The model reacts with only a very small decrease in stress starting from day 73.

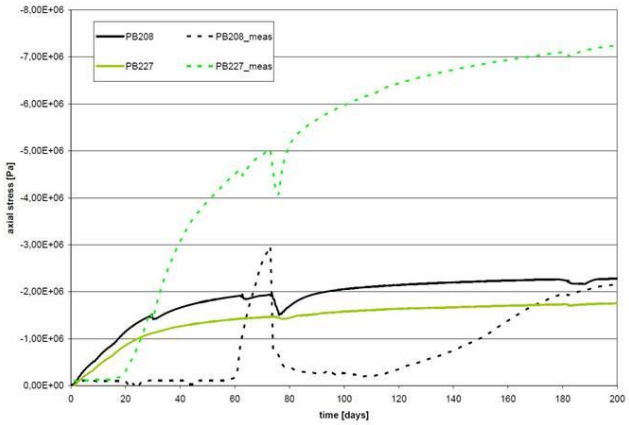

Fig. 2-19: Considered axial stress sensors, measurement vs. calculation

After the final analysis, a best parameter set could be defined. With this design, the Euclidian distance between the measured and calculated values became minimal. For the current best design parameter set, the radial stresses are within a realistic range and can be regarded as an adequate assessment of the stress within the experiment. The axial stresses still show contradictions. The measurement uncertainty and probably the disturbing effects (especially temperature effects) from the adjoining Canister Retrieval Test were not taken into account. No unequivocal sensitive parameters for the entire model could be defined yet. Reasons could be an insufficient number of parameter sets or, more probable, an incomplete consideration of all physical effects in the numerical model. This needs further investigation.

2.3 Particle based mechanical buffer model

A methodology to simulate the thermo-mechanical behaviour of claystone, especially of the EDZ, by applying a discrete element numerical code (PFC) has been developed. PFC is based on the distinct element method (Cundall & Strack, 1979) and can be used to study rock damage by building particle assemblies and checking the breakage of bonds under stress. Rocks are modelled by spherical particles of varying diameters bonded together to simulate intergranular cohesion. The “parallel bond” used is assumed to behave as a cylindrical piece of material with a finite radius, connecting two discrete elements that can break

apart if the normal stress or the shear stress inside the bond exceeds its normal or shear strength (Itasca, 2003). The contact forces between particles are computed for each contact in the assembly. With the resulting forces and moments acting on the particles, the Newtonian equations of movement can be solved for each particle. However, there is a drawback as PFC models are limited in size by the very large number of particles needed to model even a comparatively small volume of rock.

A particle based material model for the Opalinus clay is already available. Currently, a simulation of a borehole disposal system consisting of canister, clay based buffer, borehole casing, EDZ and intact host rock is done by using a combination of continuous (FLAC3D) and discontinuous numerical simulations with different computer codes (PFC, UDEC, 3DEC). The results are described in chapter 3.2.3.

A more difficult situation appears when the EDZ evolution next to sealing elements consisting for example of bentonite is to be simulated. In current closure concepts for drifts and shafts in clay formations, the support of the underground excavation is assumed to be taken out at the locations where bentonite plugs are planned. This means that there is a direct contact between the sealing material and the host rock and its EDZ without any casing at the contact zone as planned for the emplacement boreholes. In order to be able to simulate the EDZ and contact zone behaviour more precisely, a particle based mechanical material model for a bentonite plug has been developed to allow for a particle-particle contact zone.

The macroscopic behaviour of a particle based material depends on the interactions at the microscopic level. It is easy to assign specific microscopic properties to the particles of a DEM model. However, it is difficult to choose the properties in such a way that the behaviour of the resulting synthetic material reflects the behaviour of the intended physical material. The input characteristics of the microscopic components are usually not known. For continuous simulation models (e.g. finite element method), it is possible to derive the required properties (e.g. Young's modulus, strength, etc.) directly from measurements which have been performed on laboratory samples. Due to the interaction in the area of the individual particles, however, this approach is not suitable for the DEM method. First, the relevant behaviour of the simulated physical material has to be set. Then, the relevant microscopic properties are to be identified by means of calibration. During calibration, for example using a biaxial and/or Brazilian test, the measured material properties are compared with the simulation results until a best fit is obtained. Based on 2D simulations, a first calibration process has been performed with a material generation in a rectangular vessel. It forms an isotropic system, where the particles are well connected with each other at a specified confining pressure. The material generation is done as follows:

1. The material vessel (consisting of 4 walls) is densely filled with particles (Fig. 2-20). In this step, the particles and the walls are frictionless. The particles are half the size of their final size and are placed randomly, so that they do not overlap. Then the radii are increased to their final values and the system is allowed to reach static equilibrium. The number of arithmetic steps required depends on the model size, where larger models require more steps. All particles have to be in contact with their neighbours, and the force distribution throughout the assembly has to be nearly constant before the next step can be taken.
2. The next step is the installation of the specified isotropic stress. The radii of all particles are changed continuously to achieve a specified isotropic stress.
3. The third step reduces the number of the so-called "floating particles". These are particles with less than three contacts. They often appear in mechanically compacted samples of particles with varying radii and are randomly distributed. For the subsequent step, it is desirable to reduce the number of floating particles so that a denser network of bonds is obtained.

4. If the contact and parallel bonds are set, they are installed throughout the assembly between all particles that are in physical contact or in near proximity. Then, all particles are allocated the specified friction coefficient. The specimens can now be subjected to material testing.

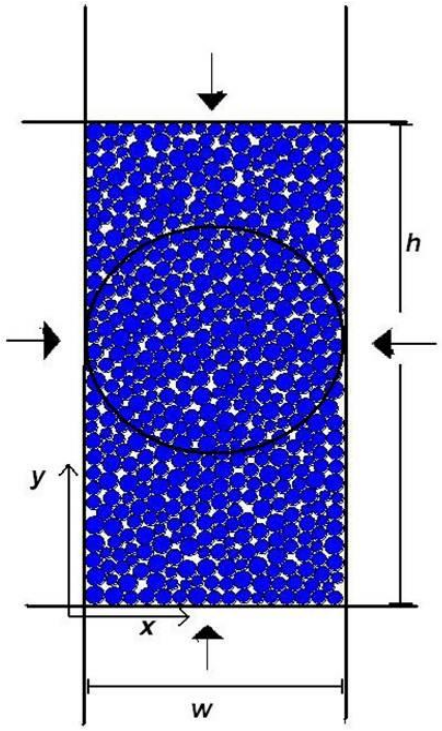

During the biaxial test the, upper and lower walls move towards each other, and in the Brazilian test, the left and right walls converge, which causes a stress build-up. The stresses and strains within the sample are measured using two procedures: (i) The average values from three measurement circles within the sample (top, middle, and bottom) are computed, and (ii) the forces on the walls and outer dimensions of the specimens are determined (wall measurements provide a more uniform averaged response over the entire specimen surface).

As the system is sensitive to the loading rate, a rate was chosen that was slow enough to ensure that the system has enough time to adjust to the force redistribution that accompanies each non-linear movement.

Fig. 2-20: Particle based material sample limited by solid but movable walls.

Biaxial test

The biaxial test is performed on a rectangular segment (Fig. 2-20). The top and bottom walls are loaded with a defined stress. The side walls are controlled by a servomechanism to get a constant confining stress. The biaxial test is carried out as follows:

- In a first stage, the particles are allowed to settle. The sizes obtained in the end are taken as the initial values to be used in the computation of stresses and strains during the following loading phase.
- After the settlement phase is finished, a load is exerted on the specimen by moving the walls towards each other at a specific velocity.
- The loading phase continues until the break-up criterion is reached. This break-up criterion is the deviatoric stress. During the test, the deviatoric stress is monitored, and the maximum value is recorded. Normally, this value will increase to a maximum and then decrease. At this point, the specimen breaks, and the test is terminated.

During the test, the monitored values are: (i) stresses and strains, (ii) energy (energy exerted on the specimen by the walls, energy stored at all contacts, energies stored in all parallel bonds, and the total strain energy), and (iii) number of cracks initiated during the test.

After the biaxial test is completed, the macroscopic Young's modulus and the Poisson's ratio, which both correspond to a specific state of stress, are computed together with the peak strength, which is defined as the maximum value of axial stress. In addition to this, the total number of cracks in the specimen at peak load is determined.

Brazilian test

The Brazilian test is based on the simulated specimen described above. The first step is analogous to the biaxial test (settlement stage, exerting the axial and confining stresses). Then, the specimen is trimmed into a circular shape by deleting the particles around the disc indicated in Fig. 2-20, with a diameter selected so that the disc is in contact with the lateral walls. The top and bottom walls are moved apart to ensure that they do not disturb the test.

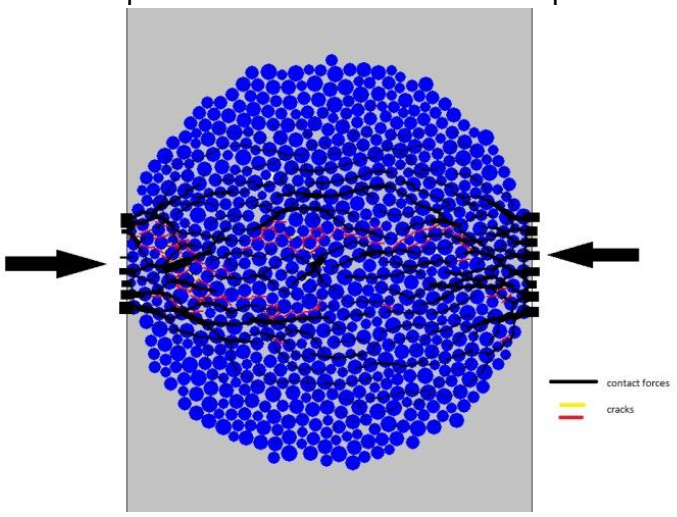

Fig. 2-21: Illustration of contact forces and developed crack at the end of a test run.

The left and the right walls are now moved toward each other with a specific velocity. The average and the maximum forces are monitored until the maximum force exceeds the specimen's failure strength. As an example, Fig. 2-21 shows the contact forces developed as well as cracks at the end of a test. Finally, the peak force (F_f) and the total number of cracks in the specimen are determined. The peak force is used to calculate the tensile strength.

$$(\sigma_t) = \frac{F_f}{\pi R}$$

With R = radius of the disk.

Results

In the beginning, the micro-properties of the particles and bonds are set to the same values as the laboratory results of bentonite (IBeWa, 2011; Johannesson, 2008; Börgesson et al., 1995; Rautioaho & Korkiala-Tanttu, 2009).

Tab. 2-5: Input parameters based on laboratory results (in red) and calculated macroscopic specimen parameters

Initial microscopic input parameters		Calculated macroscopic specimen parameters
Particles	Parallel bonds	
Young's modulus: $E_c = 4{,}1\ GPa$ Friction coefficient: $\mu = 0{,}6$ Poisson's ratio: $\nu = 0{,}27$ Tensile strength: $\sigma_f = 0{,}96\ MPa$ Density: $\rho = 2010\ kg/m^3$	Young's modulus: $E_p = 4{,}1\ GPa$ Normal strength: $\overline{\sigma}_c = 0{,}95\ MPa$ Average shear strength: $\overline{\tau}_c = 3{,}05\ MPa$	Young's modulus: $E = 2{,}86\ GPa$ Poisson's ratio: $\nu = 0{,}16$ Tensile strength: $\sigma_t = 0{,}047\ MPa$
Final microscopic input parameters		
Particles	Parallel bonds	
Young's modulus: $E_c = 8{,}20\ GPa$ Friction coefficient: $\mu = 0{,}3$ Poisson's ratio: $\nu = 0{,}27$ Tensile strength: $\sigma_f = 0{,}96\ MPa$ Density: $\rho = 2010\ kg/m^3$	Young's modulus: $E_p = 8{,}20\ GPa$ Normal strength: $\overline{\sigma}_c = 0{,}95\ MPa$ Average shear strength: $\overline{\tau}_c = 3{,}05\ MPa$	**Young's modulus: $E = 4{,}08\ GPa$** **Poisson's ratio: $\nu = 0{,}19$** **Tensile strength: $\sigma_t = 1{,}08\ MPa$**

Based on the initial input parameters, the calculated macroscopic Young's modulus of the specimen was 70%, the Poisson's ratio was 60%, and the Tensile strength was only 50% of the laboratory values. Obviously, the microscopic values have to be set completely different from the macroscopic properties of the entire specimen. To get a better understanding of how to set the microscopic parameters, test series were run where only one microscopic parameter per test run was changed (Schirmer, 2013). After the most dominant microscopic parameters had been identified, which turned out to be the Young's modulus of the parallel bonds and the friction coefficient, and after a considerable number of calculation runs, a pa-

rameter set was identified that led to a macroscopic mechanical behaviour of the specimen similar to values determined in the laboratory (Tab. 2-5).

Based on this calibration, a mechanical material model for a particle based bentonite material is available. This material model does not yet include the development of a swelling pressure as described for instance in section 2.2.1. In the following subchapter 3.2.3, particle based 2D simulation of the EDZ around underground boreholes in Opalinus clay is described as a further step in the development of a model for host rock and engineered barriers in a clay formation that is completely particle based.

3 EDZ investigations

3.1 Permeability evolution

According to previous conceptual design studies, waste disposal in vertical emplacement boreholes is the preferred disposal concept (Jobmann et al., 2007, 2009). One issue regarding borehole disposal is that due to the drilling and the associated disturbance and damage in the area surrounding the emplacement boreholes, the favourable properties of the clay formations could change, and the rock could lose part of its barrier function. Stress redistribution will lead to the creation of a so-called excavation damaged zone (EDZ), the properties of which depend on the initial stress field, the material properties, the existence of natural fracture zones or local inhomogeneities of the rock mass, and the geometry of the boreholes. Right after excavation, an EDZ with cracks and fissures forms around the borehole. An EDZ represents a potential pathway for radionuclides due to its increased porosity and crack permeability. A key question to be answered within a safety analysis is how the EDZ around an emplacement borehole evolves as a function of time and stress and what this means with regard to its permeability. A major issue in this context is the considerable amount of heat that, due to radioactive decay, dissipates into the host rock and induces thermal stresses and possibly temperature enhanced creep of the host rock. The latter may lead to a (self-)sealing of the excavation-induced cracks and fissures (Blümling et al., 2007; Buehler et al., 2003). In the framework of the SELFRAC project, sealing and healing mainly of the plastic Boom clay and partly of Opalinus clay was investigated. A rather fast sealing (but not healing) of the Boom clay was found and a much slower sealing of Opalinus clay (Bastiaens et al., 2007). Davy et al. (2007) investigated the permeability of macro-cracked argillite and found that – when the flowing liquid was water – a swelling of the clay particles led to an additional sealing of fractures. Dedecker et al. (2006) proposed a calculation method for hydraulic properties of cracked Callovo-Oxfordian clay using two coupled finite difference computer codes.

An important task is to evaluate the thermo-mechanical impact of a filled, and thus heated, emplacement field on individual boreholes and their EDZ, especially on open emplacement boreholes that are being prepared to take up waste canisters. Therefore, laboratory investigations were performed resulting in a description of the permeability and effective porosity, i.e. the pore space relevant to fluid flow, of cracked samples as a function of confining pressure, thus simulating the closing of EDZ cracks by creep behaviour of a clay host rock.

3.1.1 Material and methods

The investigated Opalinus clay samples came from the Mont Terri rock laboratory in Switzerland. The depth level is approximately 200 m below surface level. The samples were taken from borehole BHE-D25 drilled in the side wall of a gallery called MI-niche at a borehole depth range of 5-6 m. The horizontal borehole cuts the natural bedding of the clay at an angle of approx. 45°. The drill core samples obtained were packed in suitable plastic tubes directly after drilling. In order to protect them against mechanical damage and extensive drying, the annular space between the tube and the drill core was filled with epoxy resin (Fig. 3-1). Nevertheless, an influence from drilling and stress relaxation cannot be excluded. The investigations were carried out according to the following steps: (i) preparation of samples from the different drill cores of Opalinus clay, (ii) determination of the initial gas permeability and effective porosity, (iii) artificial damage of the samples by tensile strength tests, and (iv) determination of permeability and effective porosity along drill core axis (45° to bedding) of the cracked samples for different restraint conditions.

Artificial damage – methodology and application

In preparation for the permeability tests, cylindrical samples with a diameter of 50 mm and 100 mm were drilled out of the available cores. The orientation of the samples in relation to

the bedding of the clay is shown exemplarily for samples D25-3 and D25-4 in Figure 3-1. The 100-mm samples from cores D25-1 and D25-7 were taken with the same orientation as D25-3, which is parallel to the core axis.

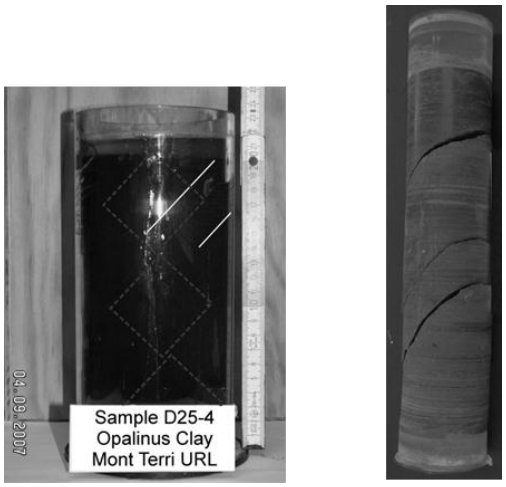

Fig. 3-1: Opalinus clay samples: D25-4 before drilling, including orientation and D25-3 with cracking along the natural bedding

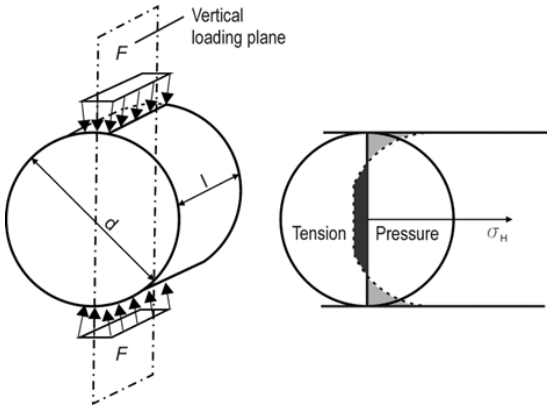

Fig. 3-2: Sketch of the test configuration and the stress distribution over the sample (Davy et al., 2007)

For the generation of cracks in the sample, a test method called 'indirect tensile stress test for rock samples – Brazilian test' was applied. The test was developed by the German Society for Earth Work and Soil Engineering for the use in rock mechanics. Figure 3-2 shows a sketch of the test configuration and the stress distribution over a test sample. The tensile strength σ_t [N] can be determined by equation (1) (DGED, 1985):

$$\sigma_t = 0.636\ F\ /\ (d l) \qquad (3\text{-}1)$$

F is the force applied in [N], d is the diameter and l the length of the sample, both in [mm]. The test requires samples with a diameter of ≥ 50 mm and a length to diameter ratio of approximately 1. During the tests, the samples were not completely damaged but the load was continuously increased and stopped immediately after cracking. Thus, the cylindrical shape was kept for the subsequent permeability and porosity tests. This kind of test was applied in order to artificially create cracks with increased permeability in the samples (Fig. 3-3 and 3-4).

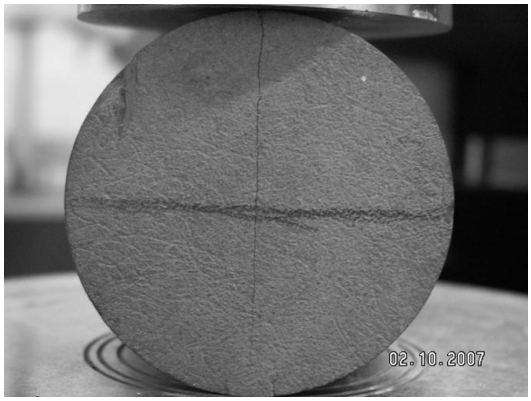

Fig. 3-3: Cracked sample

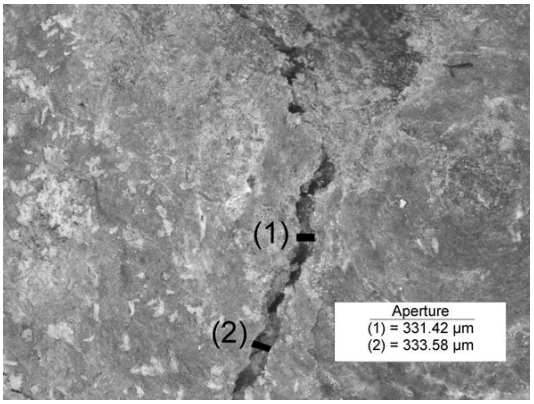

Fig. 3-4: Crack of sample D25-1.1

Determination of permeability and effective porosity

The determination of permeability is conventionally based on the measurement of a steady state flow process under constant test conditions. The steady state requirement leads to a

high experimental effort for the measurement of low flow rates and the keeping of constant test conditions over long test durations, especially for specimens of very low permeability. Therefore, a test concept based on the monitoring of an impulse-induced unsteady flow process was applied for the determination of the permeability of the Opalinus clay (Häfner et al., 1996). This test configuration is schematically shown in Fig. 3-5.

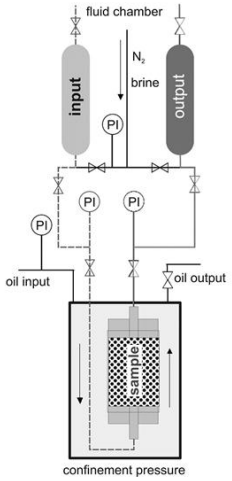

Fig. 3-5: Schematic diagram of the test configuration.

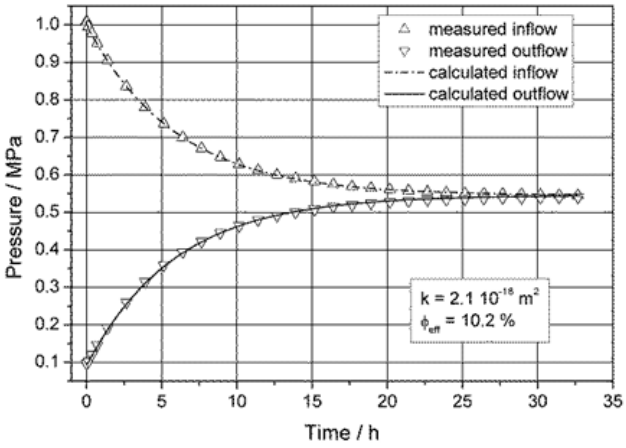

Fig. 3-6: Measured and calculated pressure curves for permeability and effective porosity identification.

A sample is completely covered by a rubber seal and installed in a pressure cell. An inflow and outflow gas pressure chamber are connected to the test cell, both having a known volume. The inflow chamber is adjusted to a defined gas pressure and the outflow chamber is adjusted to atmospheric pressure. Both chambers are opened at the same time and the pressure development in both chambers resulting from pressure compensation through the sample is recorded. The knowledge of the exact volumes of the test equipment (inflow and outflow chamber, sample, lines), the viscosity and compressibility of the fluid, the compressibility of the test equipment and the time-dependent pressure evolution measured in the input and output chamber are essential for the determination of the permeability and effective porosity. Taking these data into consideration, a numerical model of the flow process was generated for each test to calculate the two time-dependent pressure curves. The identification of permeability and effective porosity was performed by fitting the measured and calculated pressure curves. A fitting of measured data is shown in Fig. 3-6.

The test method allows the identification of the samples' permeability for gases and liquids in the range of $1 \cdot 10^{-12} > k > 1 \cdot 10^{-24}$ m² and of the effective porosity down to 0.1 Vol%. The main features of the test method applied are the short test duration for very low gas and liquid permeabilities (hours to days) and the simultaneous determination of the permeability and effective porosity. The permeability investigations on the Opalinus clay samples were done by applying a confining pressure (p_c) from 0.25 MPa to 5.0 MPa. Dry nitrogen was used with a gas injection pressure varying from $p_t = p_c$-0.2 to p_c-0.3 MPa. It has to be pointed out that the test method describes a flow process through a partly saturated porous medium. Due to these two-phase flow conditions, the determined gas permeability represents the potential flow process and thus should be taken as *effective* gas permeability.

3.1.2 Results and discussion

Initial properties

Prior to cracking the samples, several initial properties were determined in order to get information on the untreated situation. In addition to permeability, the total and effective porosity as well as the water content and water saturation of each sample was determined. Tab. 3-1 gives an overview of sample properties.

Tab. 3-1: Initial properties of samples

Sample	Length [mm]	Diameter [mm]	Direction of measurement	Density (wet) [g cm^{-3}]	Mass (wet) [g]	Grain density [g cm^{-3}]	Initial total porosity [%]	Initial water content [wt. %]	Initial saturation [Vol%-]	Tensile strength [MPa]
D25.1.1	27.6	38.6	axial	2.343	75.69	2.60	12.6	3.1	57	1.09
D25.3.1	28.8	49.4	axial	2.378	131.23	2.60	10.7	2.4	52	1.80
D25.3.2	27.2	49.4	axial	2.356	122.74	2.60	11.5	2.4	48	2.49
D25.3.3	27.4	49.4	axial	2.343	122.95	2.60	12.0	2.4	46	2.02
D25.4.1	51.5	49.4	axial	2.454	242.25	2.60	6.9	1.4	50	2.13
D25.4.2	50.4	49.5	axial	2.329	225.90	2.60	11.7	1.4	28	-
D25.7.1	100.0	92.5	axial	2.372[1]	1672.26	2.60	10.6	2.0	44	1.30

[1]determined from the average of the dry density

The total porosity was determined by using the densities. All initial values are shown in Fig. 3-7. The initial water content (wt.%) of the samples was between 1.4% and 3.1%. In the framework of earlier laboratory investigations on thermal parameters, the initial water content of similar samples from the same borehole was measured between 2.3% and 4.1% (Buntebarth, 2004).

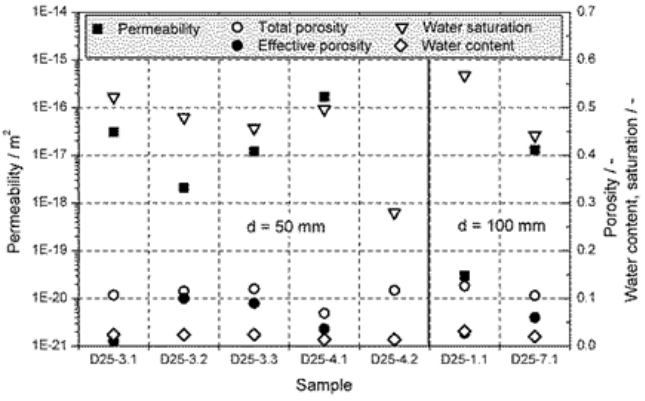

Fig. 3-7: Initial hydraulic properties of the test samples

This indicates that even though the samples were well-coated, a slight drying could not be avoided during storage. Together with the total porosity of 6.9 Vol% to 12.6 Vol%, this equals a water saturation of 28 Vol% to 57 Vol%. The corresponding gas permeability was between 3.2 10^{-20} m^2 and 1.9 10^{-16} m^2. Compared with the others, the gas permeability of sample D25-1.1 is very low (3.2 10^{-20} m^2). It was assumed that this is mainly due to the high water saturation (Fig. 3-7) impeding the gas flow. The saturation of sample D25-4.2 is comparatively low which is due to a pre-existing damage of the sample. Due to this damage, the initial permeability and effective porosity could not be determined precisely.

Tensile strength

In order to generate artificial cracks for permeability measurements, all samples were exposed to a uniaxial pressure that was continuously increased from 0 MPa up to their individual tensile strength limit and above. When comparing the results of the tensile strength measurements (Fig. 3-8), a strong variation of the maximum tensile strength is obvious for all the individual test samples. For the Opalinus clay, tensile strength values between 1.09 MPa and 2.49 MPa were obtained. Possible reasons for these differences could be different pre-existing damage of the samples due to the drilling process or a slightly varying orientation of the application of force relative to the bedding planes. Generally, the obtained values correspond very well with the investigation of Mathier et al. (1999) and NAGRA (2002), who found values between 1.2 and 2.7 MPa.

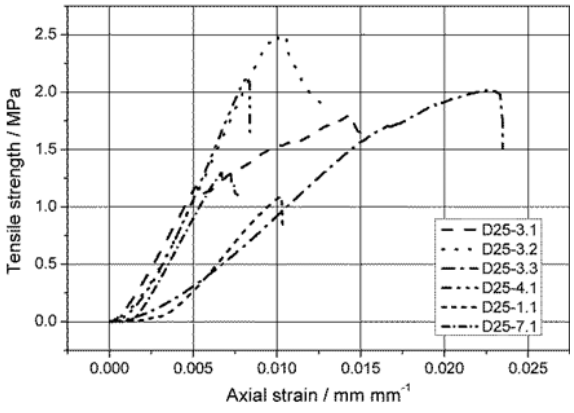

Fig. 3-8: Strength-strain diagram of the test samples

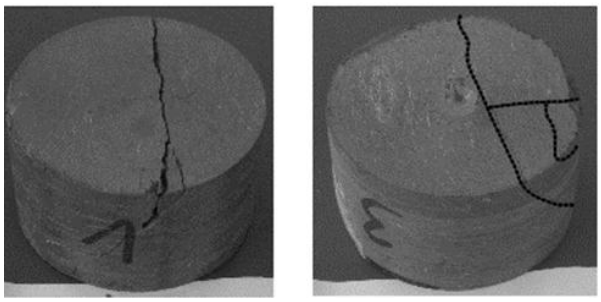

After the tensile strength of a sample had been exceeded, cracks that act as predominant pathways for fluids formed on a more or less distinct crack plane. Fig. 3-9 illustrates the cracks generated.

Fig. 3-9: Examples of generated cracks

Permeability and porosity as a function of confining pressure

After crack generation, the samples were put into a triaxial pressure cell, and the permeability and effective porosity were measured as a function of the stepwise increasing confining pressure. The results of the permeability and effective porosity measurements are shown in Figure 3-10 and Figure 3-11.

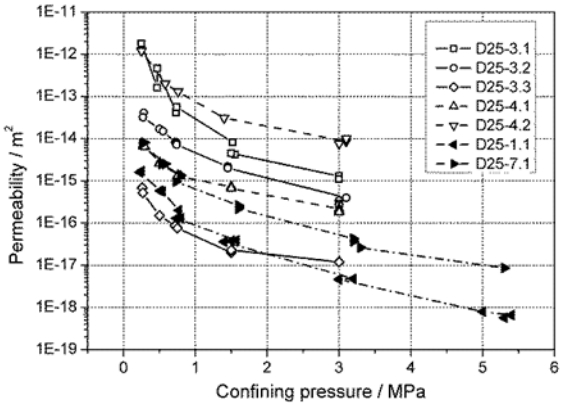

Fig. 3-10: Permeability versus confining pressure

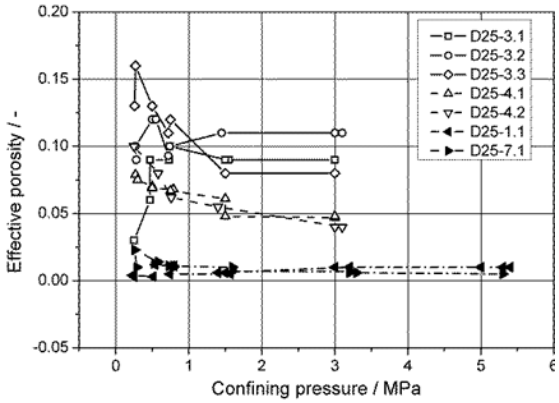

Fig. 3-11: Effective porosity versus confining pressure

The characteristics of the permeability graphs were quite similar for all samples. Although the initial permeability levels varied, the permeability reduction for each sample due to stepwise crack closing was about two orders of magnitude at pressures between 0.25 MPa and 3 MPa. Up to a confining pressure of about 1.5 MPa, the permeability decreased rapidly. Then, it decreased more slowly up to 3 and 5 MPa. One could assume that the lower decrease is due to matrix compaction rather than to crack closing, but looking at the initial values prior to cracking (Fig. 3-7), it is obvious that the initial values are not reached at 1.5 MPa except for sample D25.3.3. Thus, it seems as if the crack is not completely closed and that due to a rough crack surface there is still a small remaining space for the gas to flow through. The different starting levels of permeability are due to the fact that the initial cracking of the samples could not be controlled so that not all samples were damaged in the same way. As explained above, the samples had different pre-existing damages and tensile strengths. For two of the samples, the confining pressure was increased up to 5.5 MPa resulting in a further continuous decrease in permeability. The measured decrease in permeability is in line with results obtained by Zhang et al. (2008).

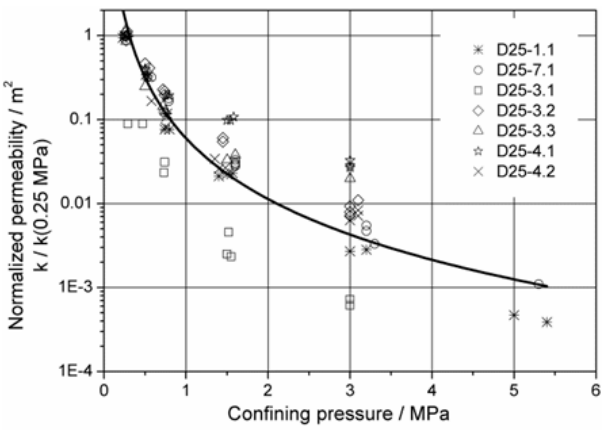

Fig. 3-12: Permeability reduction versus confining pressure

The permeability values correspond well with those found by Bossart et al. (2004). In this study, the EDZ of drifts in the underground rock laboratory at Mont Terri was investigated where the mean EDZ permeability was between 10^{-15} and 10^{-14} m^2. For a better comparison of the permeability development, the measurements for each sample were normalized to their start values at 0.25 MPa (Fig. 3-12). Generally, the permeability decrease for all samples can be described by equation (3-2).

$$k \,/\, k(0.25\ \text{MPa}) = a\, p^b \qquad (3\text{-}2)$$

With k = permeability [m^2], p = confining pressure [MPa], and the empirical parameters a = 0.06 and b = -2.404.

Looking at Figure 3-12, it is not possible to clearly distinguish between crack closure effects and matrix compaction effects on permeability as discussed above. In order to check the behaviour of the Opalinus clay not only under increasing pressure but also under decreasing pressure conditions, the permeabilities of the samples D25-1.1 and D25-7.1 were measured at stepwise decreasing pressure from 5.3 MPa down to 3.0 MPa and 0.25 MPa. As can be seen in Figure 3-13, the reduction in permeability seems to be an irreversible process. Going down from 5.3 to 3 MPa no increase in permeability was observed. It was not until the lowest confining pressure of 0.25 MPa was reached that a slight increase in permeability was measured. This led to the assumption that during pressurization, some kind of sealing process took place, which resulted in a permanent crack closure.

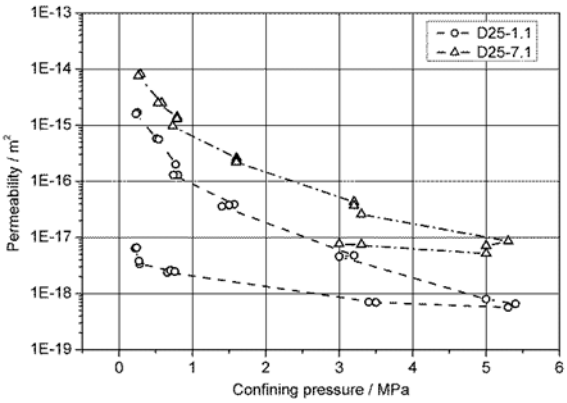

Fig. 3-13: Permeability versus confining pressure on loading and de-loading path.

Looking at the effective porosity values (Fig. 3-11) measured during confining pressure increase, the view is a bit different. On the one hand, a distinction can be made between the three different sample types (D25-3.x, D25-4.x, and D25-x.1). For each type, the level of effective porosity is a bit different ranging from about 0.01 for the D25-x.1 samples to about 0.1 for the D25-3.x ones (Fig. 3-11). A similar distinction cannot be made when looking at the permeability plot only (Fig. 3-10). On the other hand, it can be seen that for two samples, the effective porosity unexpectedly increased at the beginning of the measurements at low confining pressure. This effect can be interpreted either as a result of an expulsion of water or as a result of a drying process, as several times, a technically dry gas flew through the sample over a longer period of time. Due to the gas flow during the measurement, water escaped from of the sample resulting in a higher effective porosity. At larger pressure steps, this effect was not observed any more, which led to the assumption that crack closing increased and prevented the displacement of any remaining water (Jobmann et al., 2009).

Permeability and porosity as a function of time at constant pressure

The permeability does not only depend on confining pressure but on time as well. At some of the applied pressure levels, the permeability of a sample was measured after different periods of time without changing the pressure. Generally, the permeability decreased over time, which indicates some kind of “creep” behaviour of the Opalinus clay, which resulted in a slight closure of cracks. To visualize this time dependence, the permeability values obtained for each sample at the different pressure levels were normalized to the first value (Fig. 3-14). Except for sample D25-4.2, the values obtained at a constant pressure show a decrease in permeability over time. Within a time period of 100 hours the permeability reduction is about

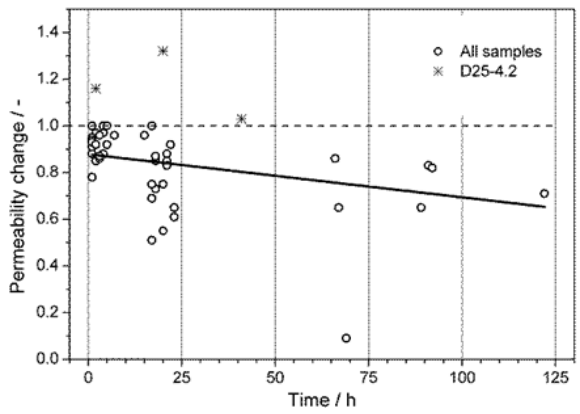

Fig. 3-14: Permeability versus time at constant pressure

30 %, and it can be assumed that the permeability is reduced even further over longer time periods. The different behaviour of D25-4.2 in this context was assumed to be the result of drying and/or the escape of water already explained above. The pre-existing fracturing observed in this sample led to a higher permeability before the permeability was reduced by the compaction process. It can be said that on the one hand the reduction of permeability depends on the reduction of available pore space. On the other hand the permeability could be further reduced if there is some “creep” behaviour that changes the connectivity of the remaining pore space.

3.2 Permeability – porosity relationship based on fractal dimension

In addition to the laboratory investigations described in the previous chapter, a methodical approach to calculate the permeability of damaged rock has been developed. The methodology is based on the theory of rock mass characterization by fractals, its calibration on laboratory data of Opalinus clay, and an application with respect to a 450-m deep generic repository site in Germany, situated in a clay formation.

3.2.1 Characterization of a fissure network by fractals

At the beginning of the nineties, the theory of rock mass characterization by fractals was developed at the University of Clausthal. Pape et al. (1984) gave a description of the role of fractal quantities for physical properties of porous media. They introduced the pigeonhole model (Fig. 3-15) that characterizes the pore space geometry by a bundle of capillaries representing the basic structure of a cascade of self-similar wall structures. In the following years they developed this theory further and proposed relations for fractal characterization of geometric properties such as porosity and tortuosity (Pape & Schopper, 1988) as well as for calculating interlayer conductivity of porous mineral systems (Pape et al., 1987a). The geometric parameters porosity, pore radius, and tortuosity mainly govern pore space transport processes such as flow of fluid or electric current as well as diffusion of dissolved components. Katz & Thompson (1984) showed that pore spaces of sandstones can be well described by fractals and are self-similar over 3 to 4 orders of magnitude in length down to about $10^{-3}\mu m$, and thus valid even for very low porosities. Pape & Schopper (1987) extended their fractal model to fissured granite systems by giving a fractal description of the Falkenberg granite micro-fissure system (Pape et al., 1987b) indicating that this model is valid for porous media and fissure systems as well. In Pape et al. (1981, 1982, and 1983), it was demonstrated that the pigeonhole model gives an adequate description of pore geometry relating permeability and capillary pressures.

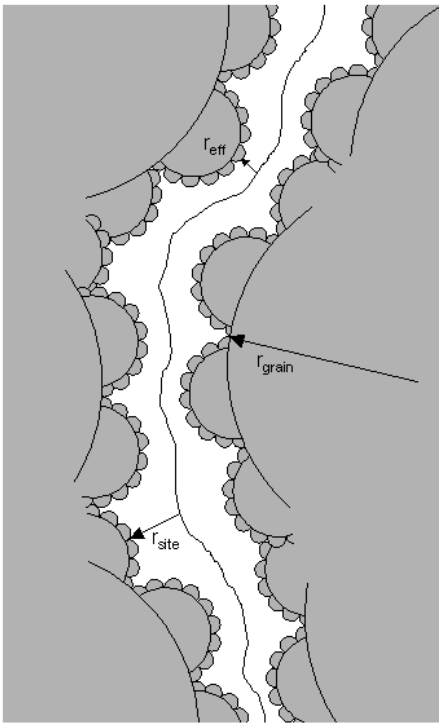

Fig. 3-15: Pigeonhole model of a sedimentary rock

Pape et al. (1999) gave a general and petrophysically justified relation between porosity and permeability that allows the calculation of permeability from porosity or pore-radius distribution for a wide range of sandstones. In addition, an indication was given for the possibility of applying this method to metamorphic and igneous rocks. Assuming that the pore space of rocks is hierarchically structured over a wide range of scales, the pore space can be reflected by the pigeonhole model, a sketch of which is given in Fig. 3-15.

The self-similarity of this model is expressed by the ratio $v = r_{i+1}/r_i$ $(r_i<1)$ with r_i being the radius of the hemispheres of the *i*-th generation (Pape et al., 1987b). Each of these is parent to *N* hemispheres of radius r_{i+1}. Mandelbrot (1977) showed that self-similarity is the basis for fractal behaviour and the fractal dimension is given by $D = \log N / \log (1/v)$. The pigeonhole model consists of two groups of spheres representing grains with a radius r_{grain} and pores with a radius r_{site} forming a cascade of hemispherical sub-structures. Small channels which are described by the effective hydraulic radius r_{eff} of a corresponding capillary connect those pores. The different radii r_{grain}, r_{site}, and r_{eff} are size parameters of the porous medium.

Pape et al. (1984 and 2000) gave an empirical relation of these radii valid for a wide range of sedimentary rocks:

$$r_{grain}/r_{site} = (r_{grain}/r_{eff})^c \quad \text{with } 0 < c < 1 \tag{3-3}$$

with *c* the structural coefficient (for sandstones c = 0.39). This relation was confirmed by (Pape et al., 1999 and 2000) after analysing a huge amount of sandstones.

3.2.2 Permeability-porosity relation

The well-known Kozeny-Carman equation is a fundamental expression for calculating permeability from pore size parameters (Kozeny, 1927; Carman, 1956):

$$k = r_{eff}^2 \ / (8F) \tag{3-4}$$

with r_{eff}, the effective pore radius and *F*, the formation factor first introduced by Archie (1942), defined as the ratio of geometrical tortuosity Λ^2 and constrictivity σ times porosity Φ, where Λ is the path-length elongation (Pape et al., 1987b):

$$F = \frac{\Lambda^2}{\sigma \cdot \Phi} \tag{3-5}$$

The formation factor is thus a geometric parameter describing the impediment of transport processes in a porous system. Inserting equation (3-5) into (3-4) yields:

$$k = r_{eff}^2 \cdot \sigma \cdot \Phi \ / (8\Lambda^2) \tag{3-6}$$

Referring to Pape et al. (1987b), Λ^2 behaves as a fractal and depends on the ratio of r_{eff} and r_{grain}, including the exponent *D* known as the fractal dimension:

$$\Lambda^2 = 1.34\ (r_{grain}/r_{site})^{2(D-2)} = 1.34\ (r_{grain}/r_{eff})^{2c\cdot(D-2)} \tag{3-7}$$

where *D* describes the active hydraulic pore system (*D** in Pape et al., 1987b). The effective pore radius is related to porosity by (Pape et al., 2000):

$$\Phi = 0.5\ (r_{grain}/r_{site})^{(D-3)} = 0.5\ (r_{grain}/r_{eff})^{c(D-3)} \tag{3-8}$$

The constrictivity σ can be defined as the ratio of effective porosity to total porosity and can be determined from the fractal dimension D^* of the hydraulic flow channel system inside the pores (D^{**} in Pape et al., 1987b), equation (30) with first term = 1):

$$\sigma^{-1} = \frac{\Phi}{\Phi_{eff}} = \left(\frac{r_{site}}{r_{eff}}\right)^{(D^*-2)} = \left(\frac{r_{grain}}{r_{eff}}\right)^{(1-c)(D^*-2)} = \left(\frac{r_{grain}}{r_{eff}}\right)^{0.5(1-c)(D-2)} \tag{3-9}$$

The shape of the surface of the hydraulic capillaries is smoother than the surface of the real pore space. Thus, D^* is smaller than the general fractal dimension D of the porous rock and their relation can be approximated by $2\text{-}D^* \cong (2\text{-}D)/2$ (Pape et al., 2000). Equation (3-8) combined with (3-9) yields:

$$2\Phi_{eff} = \left(\frac{r_{grain}}{r_{eff}}\right)^{c(D-3)-0.5(1-c)(D-2)} \tag{3-10}$$

Then (r_{grain}/r_{eff}), determined from (3-10), is inserted into (3-7):

$$\Lambda^2 = 1.34\left(2\Phi_{eff}\right)^{\frac{c(D-2)}{c(D-3)-0.5(1-c)(D-2)}} \tag{3-11}$$

Using (3-9) and inserting (3-11) into equation (3-6) yields – after simplification – an expression for calculating the permeability k including the geometric size parameters "effective pore radius" r_{eff} and "effective porosity" Φ_{eff}, a structural and thus material coefficient c, and the fractal dimension D (Jobmann & Billaux, 2010):

$$k = 9.33\cdot 10^{-2}\cdot r_{eff}^2\cdot \Phi_{eff}\cdot\left(2\Phi_{eff}\right)^{\frac{c(D-2)}{c(D-3)-0.5(1-c)(D-2)}} \tag{3-12}$$

For different sandstones c was found to be $0.24 < c < 0.7$ and for granite c was determined as 0.8 (Pape & Schopper, 1988; Pape et al., 1999). For sandy clays the fractal dimension was reported as $D = 2.61$ and for fractured hard rock D was found to be $2.65 < D < 2.91$ (Bagde et al., 2002). According to Mandelbrot (1977) one could say: the higher the fractal dimension D the more rugged the material under investigation and thus the more intense the fissuring. In order to determine values for c and D for fissured Opalinus clay, laboratory investigations on damage-induced permeability have been used. In Jobmann et al. (2009) Opalinus clay samples taken from the Mont Terri underground research laboratory in Switzerland, were artificially cracked during a tensile strength test in order to simulate a fissured rock mass in an excavation damaged zone (EDZ).

The fissured samples were put into a triaxial pressure cell and the permeability and effective porosity were determined as a function of stepwise increasing confining pressures, i.e. decreasing open spaces in the samples. The measurement results are shown in figure 3-16 where the permeability was cross-plotted to the effective porosity (Jobmann et al., 2009). The different starting levels of permeability are due to the fact that the initial cracking of the samples could not be controlled so that not all samples were damaged in the same way. The new permeability-porosity relation, equation (3-12), was applied and data fitting was performed in order to get best values for the parameters c, D, and r_{eff}. Fortunately, all four measured data sets could be fitted by the same parameter set for c and D, notwithstanding the different ranges of permeability and effective porosity. The curvature of the four graphs was controlled by c and D, while varying r_{eff} yielded an adjustment of the graphs to the level of permeability and thus damage and fissuring, respectively. The best fit was obtained for the structural coefficient $c = 0.6$ and the fractal dimension $D = 2.80$. The latter is in the range of

fractal dimensions for fissured hard rock mentioned above which is plausible as both describe a fissured system.

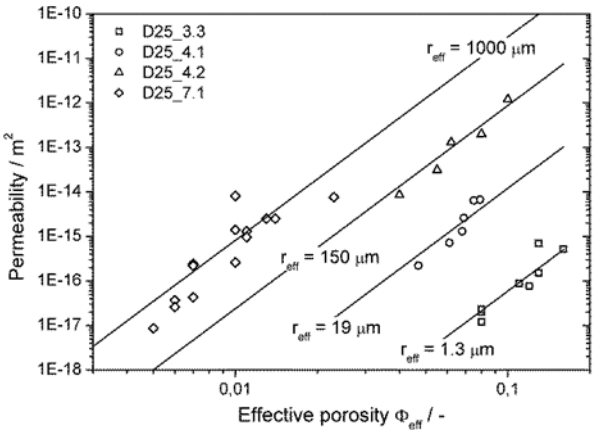

Fig. 3-16: Permeability - porosity relationship for fissured Opalinus clay applying equation (3-12)

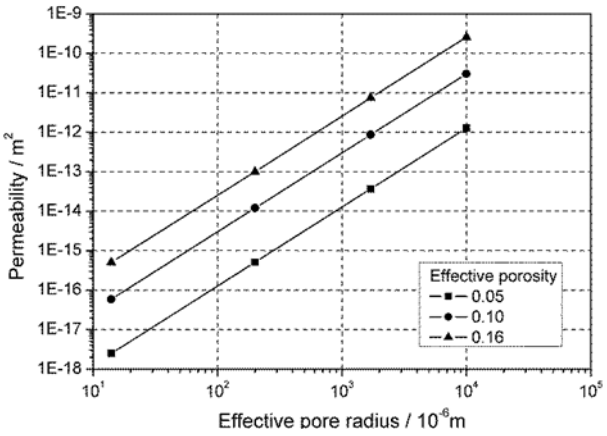

Fig. 3-17: Permeability of fissured Opalinus clay versus pore radius for different effective porosities

The dependence of permeability on effective pore radius is illustrated in Fig. 3-17. The relation was plotted for three different but representative effective porosities and the best fit values for *c* and *D*. On a double logarithmic scale, the relationship is linear showing that the pore radius changes over a wider range than the effective porosity and is thus more dominant.

3.2.3 Application for calculating EDZ permeability in Opalinus clay

Due to the fact that the influence of pore radius turned out to be more dominant than that of effective porosity (Fig. 3-17), a computer code that does not only provide porosity information but is able to calculate crack apertures as well has to be applied. The Particle Flow Code (PFC) developed by Itasca is able to provide the necessary data.

Characterization of EDZ by a granular model

Clay exhibits granularity on multiple length scales. Depending on its water content, the predominant process of cataclastic deformation occurs on the microscopic scale of clay particles (µm) and clay minerals (nm). Simulating these particles directly would limit the investigations to models of very small sizes, even on the best supercomputers. Currently, the EDZ of an emplacement borehole with a diameter of 1.5 m cannot be simulated on the microscopic scale. Therefore, the model needs to be transferred to a mesoscopic scale. At this scale, the discrete elements (namely, spheres) are thought to represent volume elements of a clay continuum.

To develop a constitutive law, the numerical model has to be assessed and compared with experimental data. For this purpose, the results of uniaxial and triaxial compression tests as well as of tensile tests were used. The development of a time-dependant model for PFC can be found in (Billaux et al., 2004), describing the long-term behaviour of the Opalinus clay. Degradation (or healing) of the clay over time is simulated by the shrinkage (or expansion) of the parallel bonds as a function of the stresses acting on them. In addition, the model allows the creation of a new bond whenever two particles come in contact. Therefore, bonds can degrade and break but they can also be created and strengthened, simulating the opening, closure and sealing of cracks. The properties of the Opalinus clay were obtained by calibration to laboratory data (Billaux, 2009). The particles have diameters varying between 8 and 12 mm, and a density of 2950 $kg \cdot m^{-3}$.

A major task in repository design and operation is to analyse the thermo-mechanical impact of a filled and thus heated emplacement field on individual boreholes, especially on open emplacement boreholes that are being prepared to take up new waste canisters. In order to identify crack occurrence and its evolution around individual emplacement boreholes a complete emplacement field was simulated with respect to its thermo-mechanical impact on one observation borehole. The work was performed by applying the numerical computer code FLAC^{3D} (Itasca, 2005), which is able to simulate the 3D thermo-hydro-mechanical behaviour of the host rock. Here, coupled thermo-mechanical simulations predicted the temperature and stress evolution around a full, 60-borehole repository section, considering a realistic disposal sequence of filling one emplacement borehole per month (Billaux, 2009). The model was 3000 m long by 2500 m wide and had a depth of 670 m, providing enough space around the repository section to absorb boundary effects. Roller mechanical boundaries were used on the bottom and vertical sides, with a free surface at the top. Temperature was imposed at the bottom and top of the model, while the vertical sides were adiabatic. Stresses and temperatures were initialized using the known vertical gradients.

In order to simulate the crack development in the near field around the observation borehole, the computer code PFC described above was used. A small area around the observation borehole was chosen as the model area. It was discretized by spherical particles of varying diameters which are bonded together. The thermo-mechanical impact on the observation borehole was obtained from a large continuum model using the FLAC3D code. A successive emplacement of canisters in the boreholes of an emplacement field was assumed to calculate the THM conditions at the observation borehole. These calculations were used in terms of initial and boundary conditions for the PFC computations.

Particle – continuum coupling

The continuous model was used to provide two types of boundary conditions: (i) the temperature field throughout the PFC model and (ii) the mechanical conditions at the boundaries of the PFC model. This means that the continuous model must output the full temperature field in the PFC region at regular intervals in time. The temperatures are then interpolated on all the particles.

The “stresses” in the PFC model are computed based on the boundary conditions provided by the FLAC^{3D} run. Thus, the stresses close to the borehole are effectively computed twice, once in FLAC^{3D} and once in PFC. The PFC boundary conditions are implemented by "slaving" the boundary particles to the velocities of the FLAC^{3D} grid points corresponding to the particle model limits. These velocity-controlled particles do not correspond to boundaries in the FLAC^{3D} model, as this model is full: it represents both, the part that is filled with particles and the borehole itself.

Once the casing is in place, it is simulated (continuum model) by putting a stiff material in the borehole volume (modulus equal to ten times the modulus of the Opalinus clay). The effect of a stiff material is simulated in the PFC model by implementing inner and outer boundaries. The emplacement of the casing takes place three months after excavation in which case the cask emplacements, and therefore heating of the borehole, start immediately after the casing. At the time of emplacement, the heat source in the “observation borehole” is activated, and the corresponding mesh is given realistic heat propagation properties. The thermal field outside the borehole is then generated by FLAC^{3D}, to be read by PFC.

Calculation results

In Fig. 3-18, all cracks around the emplacement borehole developed before lining are shown. The mean calculated extension of the EDZ is about 60 cm. For a safety analysis, fissures that are connected to each other and to the borehole and are thus able to act as a potential pathways for radionuclides are of special interest. For this reason, all cracks without any connection were deleted. The results are plotted in Fig. 3-19. In addition, eight angular zones were chosen to better analyse and visualize the crack development in the expected heterogeneous stress field. In order to observe the future development of the EDZ in response to the thermo-mechanical impact of the adjacent heated boreholes, a simulation period of 100 years was chosen.

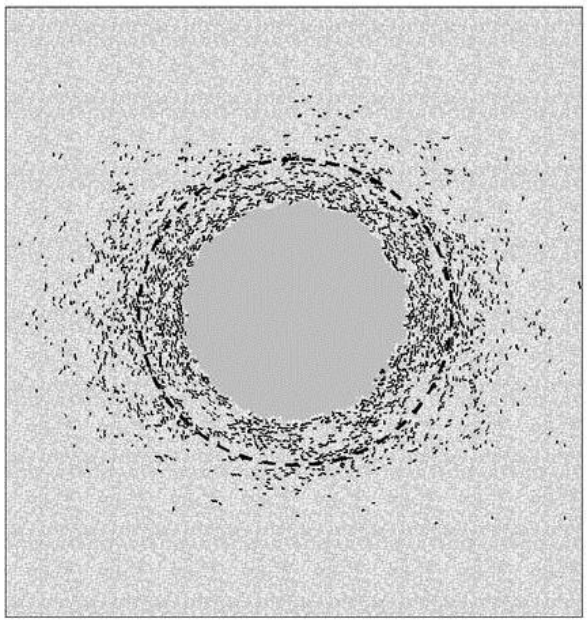

Fig. 3-18: All calculated cracks around the open borehole using PFC

Due to the outer mechanical load, a closing of the fissures was expected during this time period. Fig. 3-20 shows the crack situation after 100 years. Compared with the situation after lining, the main changes occurred in sectors 5, 7, and 8. In fact, the expected closure of fissures could be observed but was limited; meaning that a certain amount of connected fissures still remained after 100 years. It should be noted that all cracks in these figures are connected to the borehole.

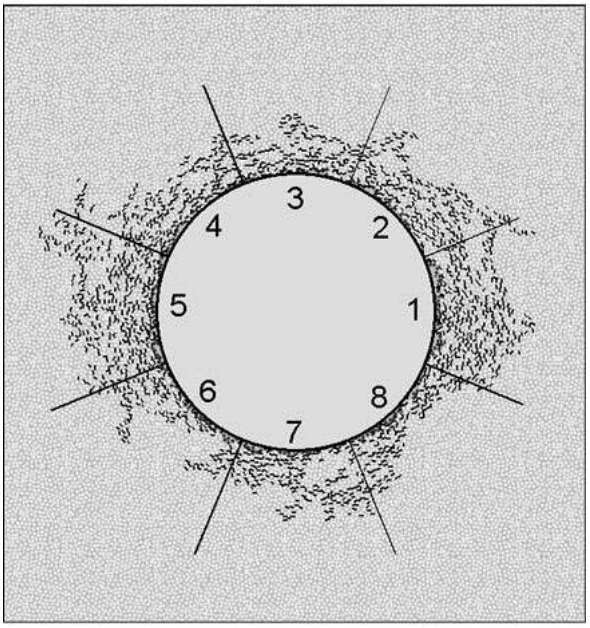

Fig. 3-19: Connected cracks around the borehole after lining (0.25 years)

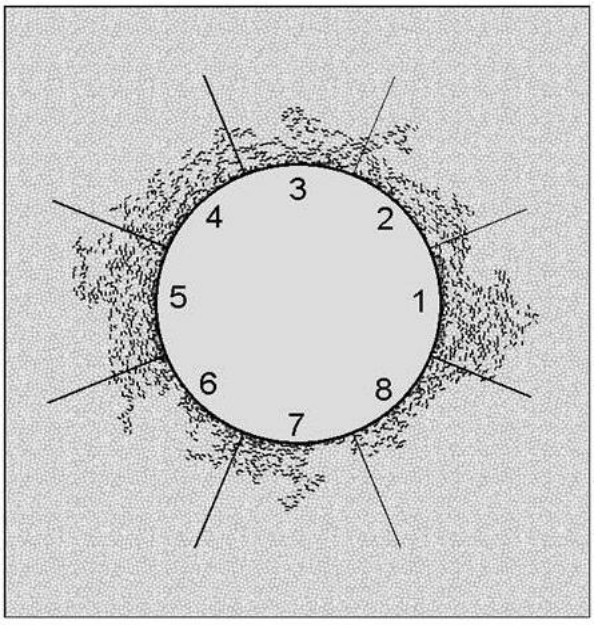

Fig. 3-20: Connected cracks around the borehole after 100 years

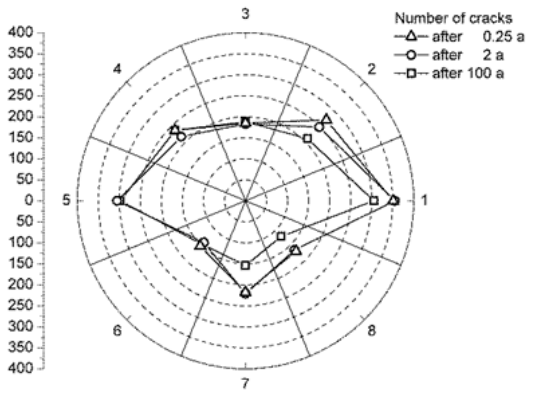

Fig. 3-21: Number of cracks around the borehole for three different time steps

In Fig. 3-21, the number of cracks is shown in a polar diagram for three different points in time: 3 months, 2 years and 100 years. A closure of fissures mainly occurred in sectors 1, 2, 7, and 8, whilst in the left sectors the amount of cracks remained more or less constant indicating a slight heterogeneous crack recovery. A more detailed analysis can be found in (Billaux, 2009). An important question in terms of a long-term safety analysis is the dimension of permeability of the fissure system in the EDZ and its evolution over time. Based on the PFC calculations it was possible to determine the pore space created by the cracks and thus the effective porosity Φ_{eff} of the fissure system as well as the fracture apertures r_{eff}. Knowing both values, equation (3-12) was applied and the permeability was determined from just the geometric parameters and the fractal dimension. In Fig. 3-22 and Fig. 3-23, the corresponding parameters Φ_{eff} and $2 \cdot r_{eff}$ (aperture) are plotted for the different angular sectors. The values were averaged, for each angular sector, over the inside of the EDZ, i.e. for all the particles included in the outline of the "connected cracks" domain.

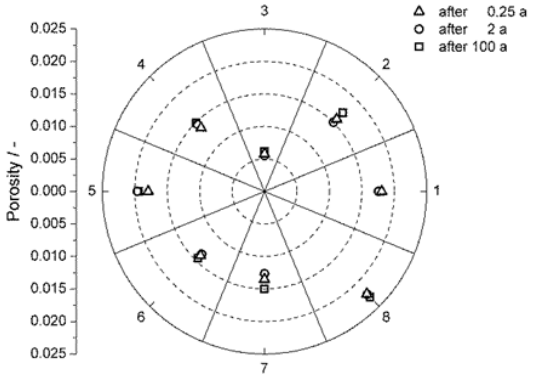

Fig. 3-22: Effective porosity around the borehole for three different time steps

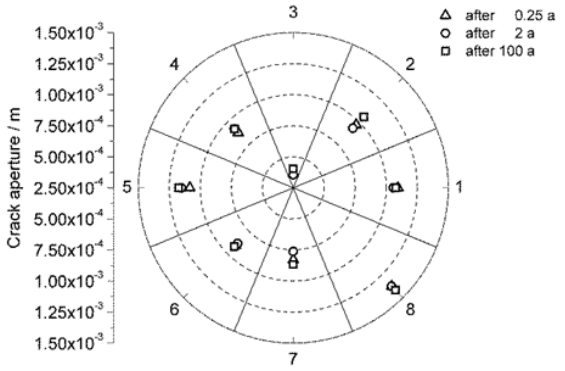

Fig. 3-23: Crack aperture around the borehole for three different time steps

Compared to the change of the number of cracks over time (Fig. 3-21), the change in crack aperture and porosity is not that obvious. Applying equation (3-12) by using the calculated porosities and crack apertures as well as the parameters for fractal rock mass characterization (*c* and *D*) obtained from the lab test calibration (see Fig. 3-16), the permeability of the individual angular sectors could be determined. The results are plotted in figure 3-24. The permeability varies between $10^{-17}m^2$ (sector 3) and $10^{-13}m^2$ (sector 8). Looking at these two sectors and comparing the number of cracks (Fig. 3-21), the crack apertures (Fig. 3-23), and the calculated permeabilities (Fig. 3-24), it is clear that permeability varies mostly with crack apertures, and much less with the number of cracks. The mean value for the EDZ was calculated to be $1.7 \cdot 10^{-14}m^2$. This value corresponds well with those found by Bossart et al. (2004). In this study, the EDZ of drifts in the URL at Mont Terri was investigated and the mean EDZ permeability was between 10^{-15} and $10^{-14}m^2$, for more or less open drifts.

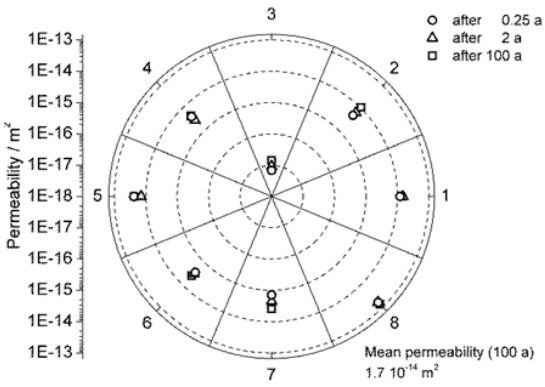

Fig. 3-24: Permeabilities around the borehole for three different time steps

4 Host rock investigations

4.1 Material and rock property changes

The thermal load of the far field is characterized by a significant long-term temperature increase in the clay formation. In the long term, this temperature increase affects the conditions of the rock, i.e., of the minerals, and of the pore water and, thus, changes the rock properties. The thermal load to be expected in a clay formation is shown in Fig. 4-1. According to this, the temperature increase has mostly faded after approximately 10,000 years.

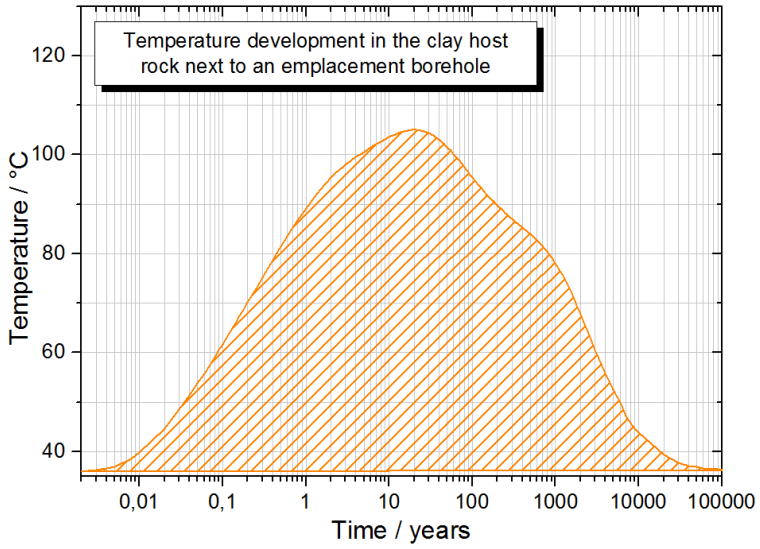

Fig. 4-1: Temperature impulse to be expected by emplacing radioactive waste in a clay formation

It is assumed that the expected changes are relatively small if this maximum temperature has already occurred in the clay formation during its burial history - which still needs to be investigated for promising clay formations in Germany. The temperature impact can cause temporary or irreversible changes in the geologic barrier. In particular, this concerns the most reactive rock components, i.e. the organic substances that are usually present in clay formations and the fine-grained clay mineral matrix.

Associated minerals and pore water in clay formations are usually not in chemical equilibrium. Depending on the pressure and temperature conditions, mineral metamorphism and reformation takes place which has the effect that the chemical/mineralogical material content of the clay approximates a chemical equilibrium. A temperature increase would accelerate the metamorphic processes. As an example, the most reactive process, i.e., the illitisation of smectites upon temperature increase has been investigated.

Suitable clay formations are characterized by high contents in pyrite and organic carbons that are sufficient to generate hydrocarbons. The hydrocarbon potential is high but thermal maturing has only progressed so far that oil is beginning to form as shown by the Kerogen type ratios. The extent to which the heat released by the waste canisters artificially accelerates maturing and, thus, oil formation has been investigated.

4.1.1 Illitisation of smectites

The effects of thermal influence on a claystone formation containing smectite (Upper Pierre Shale, Colorado) were investigated by Pytte and Reynolds (1989) on a fraction of < 0.5 µm. Although the authors do not give any information about the grain size distribution of the sili-

cate minerals, it can be assumed that the fraction <0.5 µm has the highest smectite content. Depending on the distance to the contact zone with a basalt intrusion and, thus, to the temperature source, the illite content decreases from 90% illite in mixed-layer illite/smectite (I in I/S) at a distance of 5 m and a temperature of 300°C to 25% I in I/S at a distance of 15 m and a temperature of approx. 120°C (Figure 8.1 in Pytte and Reynolds 1989). In this context, this is of particular importance because from the thermometamorphic overprinting event, the duration of the temperature increase is also known. It takes approx. 3,500 years for the temperature to increase by 20°C from the initial rock temperature (Figure 8.2 in Pytte and Reynolds 1989). 104 years after the thermometamorphic event, the temperature had decreased back to the initial rock temperature of approx. 30°C.

Plotting the duration of the thermal overprinting against the respective temperature led Pytte and Reynolds (1989) to the following equation:

$$S^4 = S_0^4/(1+4\ 74.2\ t\ S_0^4\ A\ e^{(-2490/T-Ea/RT)}) \qquad (4\text{-}1)$$

$A = 5.2 \cdot 10^7\ sec^{-1}$, Ea = activating energy (33 kcal/Mol), S_0 = initial S content, S = actual S content in I/S, t = time, T = temperature, R = general gas constant

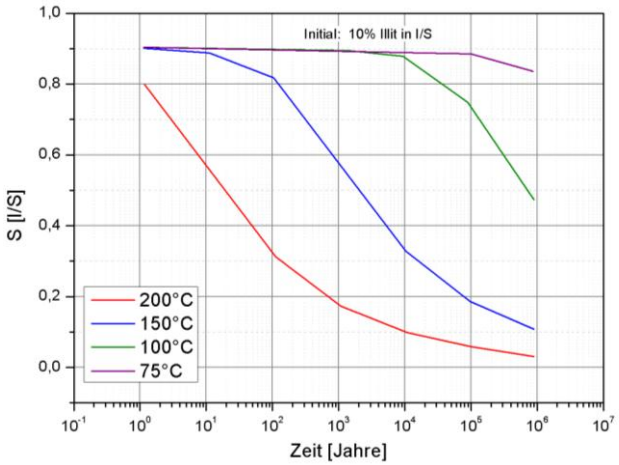

Assuming an initial content of 90% smectite in I/S, the actual smectite contents at 200°C, 150°C, 100°C, and 75°C were calculated as a function of time. The results are shown in Fig. 4-2.

Fig. 4-2: Relation between rock temperature and smectite in I/S alternating strata as a function of time in a clay formation influenced by external thermal input, according to Pyte and Reynolds (1989)

Fig. 4-2 shows that at temperatures of 200°C, half of the smectites have transformed into illite after 20 years, a process that at temperatures of 150°C takes approx. 3,500 years. At temperatures of 100°C and 75°C, illitisation does not become apparent for at least 10^4 and 10^5 years respectively. Taking into account that the temperature impulse induced by a repository has faded after about 10,000 years and that the temperature remains above 75°C for only about 1,000 years and taking further into account that the region where the temperature is increased is restricted to several metres around the respective emplacement boreholes, it can be assumed that no significant illitisation occurs within the geologic barrier. This assumption is confirmed by Huang et al. (1993), who determined the potassium (K) consumption at increasing temperatures in a comprehensive and often quoted study, which lead to a measure of the reaction kinetics of the illitisation reaction. The calculations showed that even at a low K content of 200 ppm, complete illitisation does not start until after 10,000 years, i.e. at the end of the temperature impulse induced by the repository. At 50°C and a K content of 1,000 ppm in the pore water, even one million years are not enough to initiate this process.

4.1.2 Sorption properties

Quantifiable conclusions about the retention properties of claystones at increased temperatures are best drawn from experimentally determined values about the sorption behaviour or

the distribution coefficient (Kd) of elements or radionuclides compared with individual silicate minerals. In accordance with their frequency in the claystone, they can be used to form an overall picture of the retention properties of a deep formation. However, the corresponding data currently available from literature are incomplete, are restricted to a few radionuclides or heavy metals, and are not equally relevant for all silicate minerals. Mengel (2006) plotted the experimental data available on the sorption properties of various clay minerals against the temperature. Fig. 4-3 shows the distribution coefficient (Kd) as a function of time for various radionuclides and clay minerals. The term ‚REE' comprises lanthanide elements, which – in their chemical composition and their properties – are similar to trivalent transuranic elements.

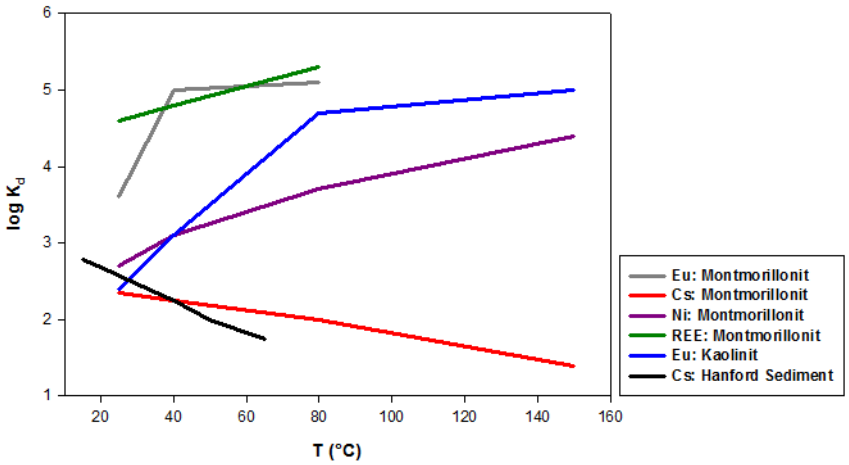

Fig. 4-3: Temperature dependency of the distribution coefficients (Kd) of Cs, Eu, Ni, and REE compared with montmorillonite and kaolinite (Tertre et al. 2005, Tertre et al. 2006) as well as for Cs compared with the sediments at the Hanford Site (Liu et al. 2003).

The figure shows that – if the temperature of the claystone increases – sorption for europium, nickel, and the trivalent transuranic elements can be expected to increase. A decrease in sorption capacity can only be expected for caesium. All in all, it can be said that the sorption capacity and, thus, the retention capacity increase with increasing temperatures.

4.1.3 Alteration of organic carbon

The transformation of organic material into hydrocarbons (oil and gas) is controlled by temperature and thus by the burial history of the sediments. The temperature influence is twofold:

1) The higher the temperature the higher the transformation rate and
2) The longer the material is exposed to higher temperature the more complete is the transformation into hydrocarbons

When determining the status of coalification of the organic material, information about the burial history of specific sediments can be obtained. The status of coalification is determined by measuring vitrinite reflection. Under several simplified conditions, vitrinite reflections can also be calculated from assumed burial history data. This allows the calculation of the transformation of organic material due to the heat input of a final repository.

In order to be able to calculate the extent to which the heat or temperature impulse caused by the repository changes the degree of maturity of organic components, a model needs to be generated and calibrated against measurement data.

In the past decades, vitrinite was found in a number of reflectance measurements during carbon and oil prospection in the Ruhr-Karbon (Carboniferous) and in various parts of the Niedersächsisches Becken (basin in Lower Saxony). Within the scope of these measurements, positive reflection anomalies were found, which could clearly be related to intrusive

bodies. These intrusive rocks introduced heat into the sediments for a long time and have, thus, significantly increased the degree of maturity of the organic components (Fig. 4-4, left).

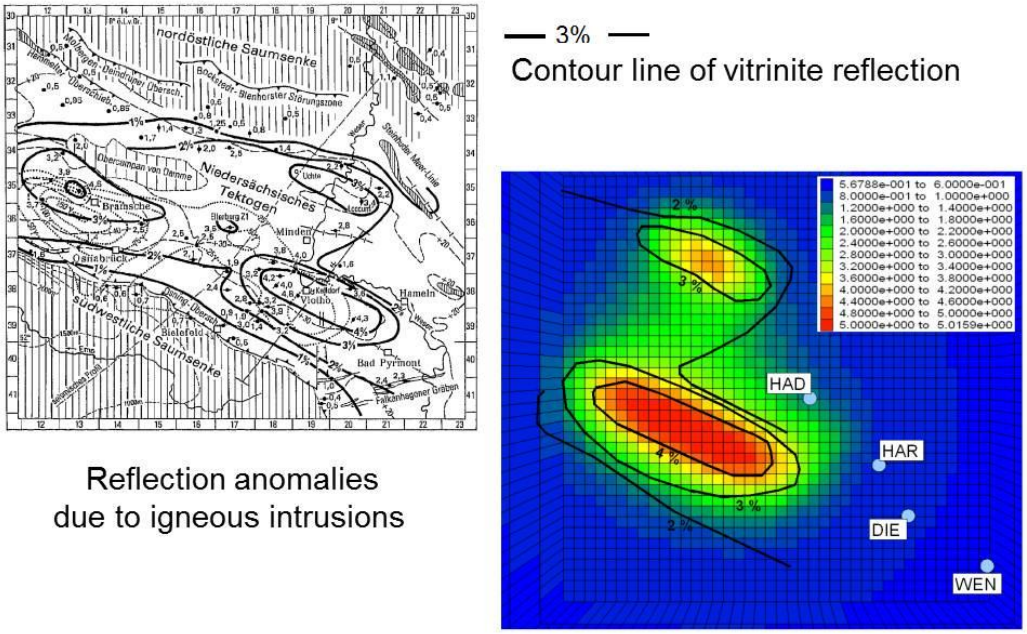

Fig. 4-4: Vitrinite reflections at the boundary Rhaetian/Lower Jurassic measured and calculated over two intrusive bodies in the Niedersächsisches Becken (Deutloff et al., 1990)

The formation of the intrusive bodies and the corresponding heat introduction into the sedimentary rock were simulated by means of a numerical 3D model. The related increase in maturity was calculated using both, the well-known Lopatin method, which relies on the determination of the “Time Temperature Index” (TTI), (Waples, 1980), as well as the kinetic reaction approach after Sweeney & Burnham (1989, 1990). The results were integrated into the model (Jobmann et al., 2007). Through parameter modification, the maturity process could be reproduced in such a way that it was adequately enough adapted to the measurement values (Fig. 4-4, right). In four boreholes in the vicinity of the intrusions (Haddessen, Harderode, Dielmissen, Wenzen), vitrinite reflection measurements have been performed. The calculated values of vitrinite reflections differ at a maximum by 18% from the measurements, which is assumed to be a sufficient approximation with regard to uncertainties.

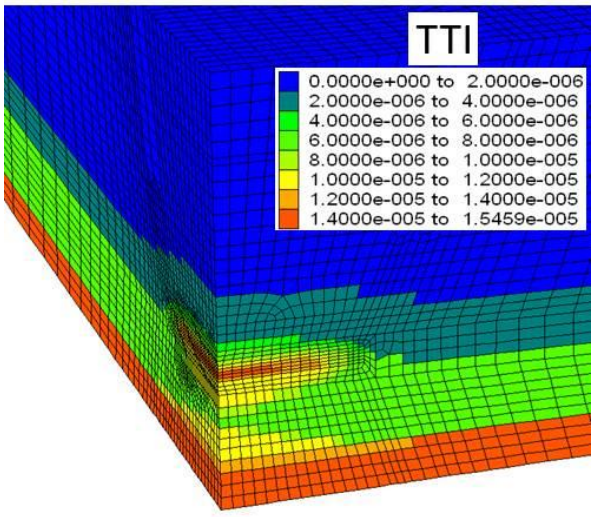

Fig. 4-5: Calculated change in vitrinite reflection caused by an artificial temperature impulse due to a repository

After calibration to natural events and to the related measurements of the vitrinite reflection capacity, the increase in maturity caused by the thermal input of the radioactive waste can be estimated. Fig. 4-5 shows a section of the 3D model with a finer discretization in the area of the repository. The calculations were carried out using the code FLAC3D. The colour legend shows the increase in maturity based on the Lopatin method, i.e. the difference to the degree of maturity prior to repository construction. The numerical values, especially the maximum value of TTI = $1.5 \cdot 10^{-5}$, is at least five orders of magnitude smaller than normal measured values (Jobmann et al., 2007).

These results show that the theoretical increase is so small that it is absolutely impossible to determine it with any precision. The level and duration of the temperature impulse through the repository are far from sufficient to modify the degree of maturity to even a small extent.

4.2 Hydro-mechanical rock response to excavation

In Switzerland, Opalinus Clay, a potential host rock formation for a nuclear waste repository, is intensively studied in the Mont Terri Underground Rock Laboratory. During the 2008 extension of the URL, the construction works were repeatedly interrupted to implement monitoring systems for a mine-by experiment. Prior to the excavation of a 24-m-long tunnel, the surrounding area was instrumented with 36 different monitoring systems comprising approximately 200 sensors. Key features of this tunnel were chosen similar to the current Swiss HLW disposal concept: circular section, full-face excavation following the geologic bedding, support by a thin layer of shotcrete. For the mine-by experiment, 26 boreholes were equipped with 7 multipoint extensometers, two multi segment inclinometer chains, and 26 pore pressure chambers (Fig. 4-6 and Fig. 4-7).

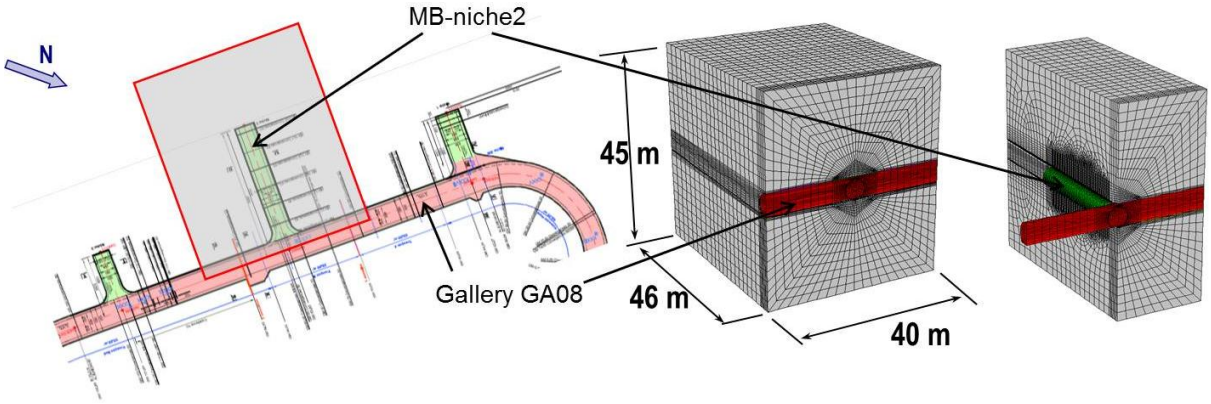

Fig. 4-6: Gallery 08 and the corresponding numerical model used for simulating the mine-by test; left: general site layout and model boundaries (gray rectangle), center: 3D-model total, right: 3D-model detail

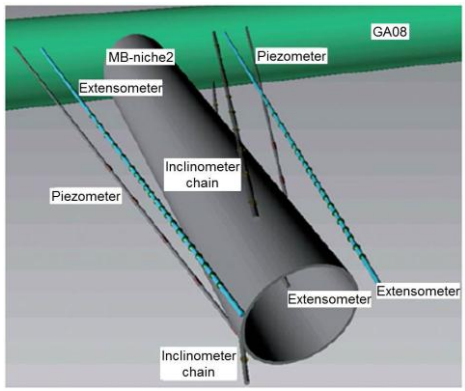

Fig. 4-7: Illustration of Mb-niche2 and some surrounding observation boreholes (modified after Vietor et al., 2010)

DBE TECHNOLOGY GmbH participated in the mine-by test with the aim to investigate the hydro-mechanical (HM) reaction of the Opalinus clay due to drift excavation. Based on a suitable constitutive model for the host rock, calculations have been performed as blind predictions before distribution of the measured data (phase I) and the interpretive modelling afterwards (phase II). Using the as-built geometry and reported excavation progress and sequences, a 3D-model (FLAC3D) was applied. The model includes the geometry of the horseshoe-shaped gallery GA08 and the test drift called MB-niche2 with a circular cross-section and a diameter of 4.5m (Fig. 4-6).

For the mechanical model, an elasto-plastic model with anisotropic strength behaviour was used. It distinguishes between matrix and bedding strength including strain-hardening & -softening. The elastic behaviour is isotropic. Time-dependent (rheological) behaviour is not

included. For the fluid model, a homogeneous porous medium is assumed with single-phase fluid flow after Darcy's law with anisotropic hydraulic conductivity. After rock failure, the hydraulic conductivities were increased by a factor of 10 to 100. The hydro-mechanic coupling was realized by applying the effective stress approach after Terzaghi (1936) with the Mohr-Coulomb failure criterion

$$\sigma' = \sigma - \alpha \cdot p \tag{4-2}$$

With σ' = effective stress, σ = total stress, α = Biot coefficient, and p = pore pressure. The pore-pressure changes due to volumetric strain or fluid content changes after:

$$\frac{1}{M} \cdot \frac{\partial p}{\partial t} + \frac{n}{S_r} \cdot \frac{\partial S_r}{\partial t} = \frac{1}{S_r} \cdot \frac{\partial \xi}{\partial t} - \alpha \frac{\partial \varepsilon}{\partial t} \tag{4-3}$$

With M = Biot modulus, n = porosity, S_r = saturation, ξ = fluid content, ε = volumetric strain, t = time. Main findings during the interpretive modelling phase were particularly (Vietor et al., 2010):

- measurable pore pressure decrease already at an excavation front distance of approx. 4 x $\varnothing_{drift}$ (excavation diameter = 4.5 m)
- measurable deformation (compression) of host rock already at an excavation front distance of approx. 2.5 x $\varnothing_{drift}$ to ½ x $\varnothing_{drift}$
- for distances < ½ x $\varnothing_{drift}$ to excavation front clearly measurable dilation (volumetric strain increase) and rapid pore pressure decrease.

These effects observed in situ indicate a very strong hydro-mechanical coupling. Hence, within the scope of a back analysis, several rock-mechanical and hydro-mechanical parameters were varied to improve the predictive model, in particular deformation behaviour and the degree of HM behaviour.

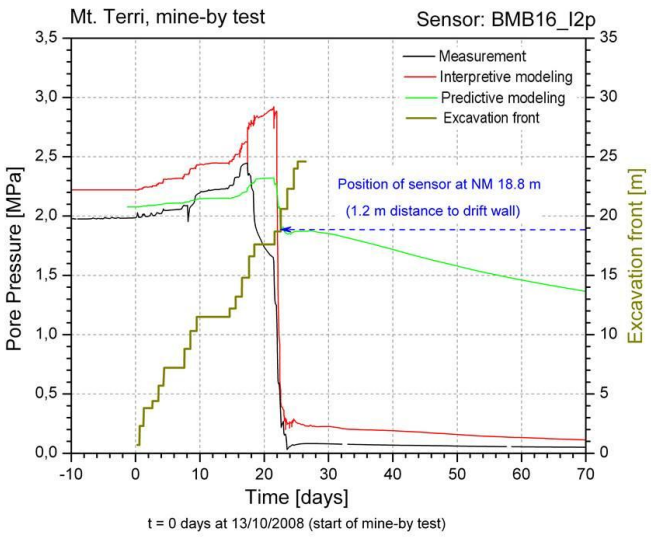

Table 4-1 gives an overview of the parameters used for predictive and final interpretive mod-modelling. The use of parameter sets combining (i) reduced drained stiffness, (ii) reduced shear and tensile strength and (iii) a reduced compressibility of the pore fluid led to an appropriate description of the host rock behaviour compared with blind prediction.

Fig. 4-8: Evolution of pore pressure, comparison of measured with calculated data for sensor BMB16-I2

Tab. 4-1: Parameters used for predictive and final interpretive modelling

Mechanical Parameters		
Density (dry) ϑ / kg / m^3	2 330	
Youngs' Modulus E / MPa	7 000 /1/ (4 000 *)	
Poisson ratio ν / -	0.29 /1/	
Pre-failure behaviour / Peak strength	Matrix	Bedding
Angle of Friction ϕ / °	24	21 /2/
Cohesion c / MPa	4.0	1.0 /2/
Tensile strength R_t / MPa	1.2 (1.0)	0.6 /1/ (0.5)
Dilation angle / °	0 (= ϕ)	0 (= ϕ/2)
Post-failure behaviour	Matrix	Bedding
Residual Angle of Friction ϕ_r / °	21 *	20 /2/
Residual Cohesion c_r / MPa	2.0 * (1.0 *)	0.1 /2/
Residual Tensile strength R_{tr} / MPa	0.1 * (0 *)	0.1 * (0 *)
Residual Dilation angle / °	0 (= ϕ_r)	0 (= ϕ_r /2)

Hydraulical Parameters		
Hydraulic Conductivity k / m/s (intact rock)	∥	2e-13 /1/
	⊥	0.7e-13 /1/
Porosity Φ / %		13.7 /1/
Fluid bulk modulus K / MPa		1 000 (2 000)
Biot coefficient b / -		0.6 (1.0)

Fluid density = 1 000 kg/m^3

Fluid viscosity = 1 mPa*sec

/1/ (Bock, 2008)
/2/ (Popp et al., 2008)
* Assumption

Modification from predictive to interpretive modeling

The comparison of results shows that the modelling approach chosen captures the effects observed in situ quite well compared with the blind prediction results. The pore pressure evolution, i.e., the onset and rate of pressure increase ("sensitivity") as well as the rapid pore pressure decrease correspond well with the in-situ observations (Fig. 4-8 and Fig. 4-9). Nevertheless, the magnitude of the maximum pore pressure is overestimated by the model. This is assumed to be most likely due to an earlier beginning of fracture-initiation in-situ prior to modelling.

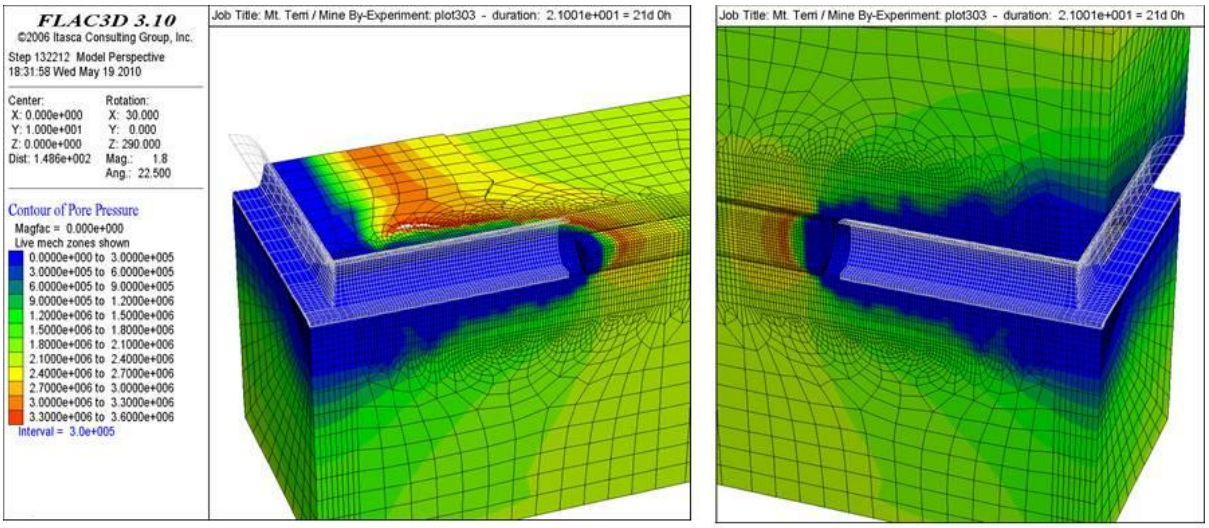

Fig. 4-9: Pore pressure field [Pa] during excavation, vertical cross-section along Niche2, left: northern part of the model, right: southern part

The modelling approach that assumes lower rock stiffness is able to reproduce the elastic rock response (onset and magnitude, Fig. 4-10). But even assuming low strength behaviour of the rock, the remaining plastic deformation after stress release is still slightly underestimated by the model. It has to be noted that the elasto-plastic constitutive model applied is

not able to reproduce further increase in time-dependent (rheological) deformation, which has been observed in-situ and is probably due to delayed visco-plastic response.

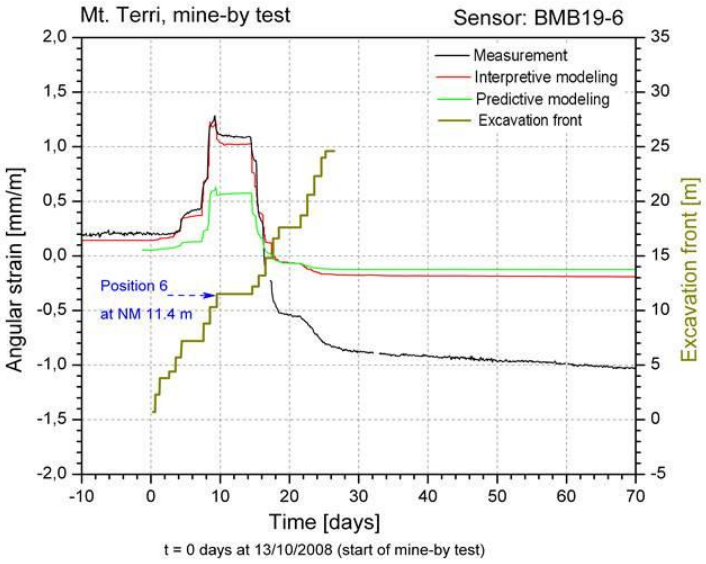

Fig. 4-10: Evolution of strain, comparison of measured and calculated data for chain inclinometer measurement BMB19-6

4.3 Thermo-hydro-mechanical rock response to heating

To study the thermo-hydro-mechanical effects of the thermal transient phase on the clay host rock of a deep repository, ANDRA (the French National Radioactive Waste Management Agency) performs an in-situ heating test called TED experiment. This experiment is the second one carried out in the Meuse/Haute-Marne Underground Research Laboratory focusing on determining the thermo-hydro-mechanical behaviour of the Callovo-Oxfordian claystone. The aim of the TED experiment is to measure the temperature, deformation, and pore-pressure field evolution around heaters and to back-analyze the thermo-hydro-mechanical properties of the Callovo-Oxfordian claystone. The TED experiment was also designed to study the evolution of the excavation damaged zone due to heating. The analyses of the TED experiment results will help to calibrate the numerical models that will be applied to the French disposal cell concept (ANDRA, 2005). A detailed description of the heater experiment is given in (Conil et al., 2012).

4.3.1 Rock characterization by laboratory experiments

A first step to characterize the THM behaviour of the clay rock is to perform laboratory investigations on drill core samples taken from observation and heater boreholes to obtain an image of the local properties and of possible local heterogeneities. 14 samples from different boreholes have been delivered for investigation. Table 4-2 gives an overview of sample identification and reference data.

Tab. 4-2: Reference data of the drill core samples

Sample ID	Borehole	Depth	Local coordinates	
		m	X / m	Z / m
EST 33791	TED 1210	14.75 – 15.05	0.046	0.575
EST 33734	TED 1212	13.79 – 14.08	2.629	-1.000
EST 33837	TED 1213	14.17 – 14.45	0.048	1.260
EST 33705	TED 1214	12.60 – 12.92	0.659	0.870
EST 33863	TED 1215	13.25 – 13.55	-1.252	-0.015
EST 33681	TED 1216	14.20 – 14.50	3.649	0.008
EST 33765	TED 1217	12.90 – 13.20	-3.162	0.260
EST 33769	TED 1217	15.40 – 15.70	-3.162	0.300
EST 33885	TED 1219	13.36 – 13.66	-0.572	-0.090
EST 33889	TED 1219	15.36 – 15.66	-0.572	-0.130
EST 34666	TED 1201	5.66 – 5.96	0	0
EST 34674	TED 1201	9.66 – 9.98	0	0
EST 34708	TED 1202	5.48 – 5.80	-2,65	0
EST 34715	TED 1202	9.43 – 9.73	-2,68	0

The laboratory investigations include measurements of

- thermal conductivity
- thermal diffusivity
- specific heat capacity
- density
- differential thermal analysis (DTA)
- carbonate content
- linear thermal expansion and
- IR-spectroscopy

Special attention has been paid to the effect of anisotropy. The rock properties of the Callovo-Oxfordian clay are known to show an anisotropic behaviour. Thus, measurements on drill core samples have been performed in different directions to the bedding of the clay with the aim to determine the factor of anisotropy (Buntebarth, 2009). As a reference for borehole location, Fig. 4-11 gives an overview of the boreholes in the TED experimental area.

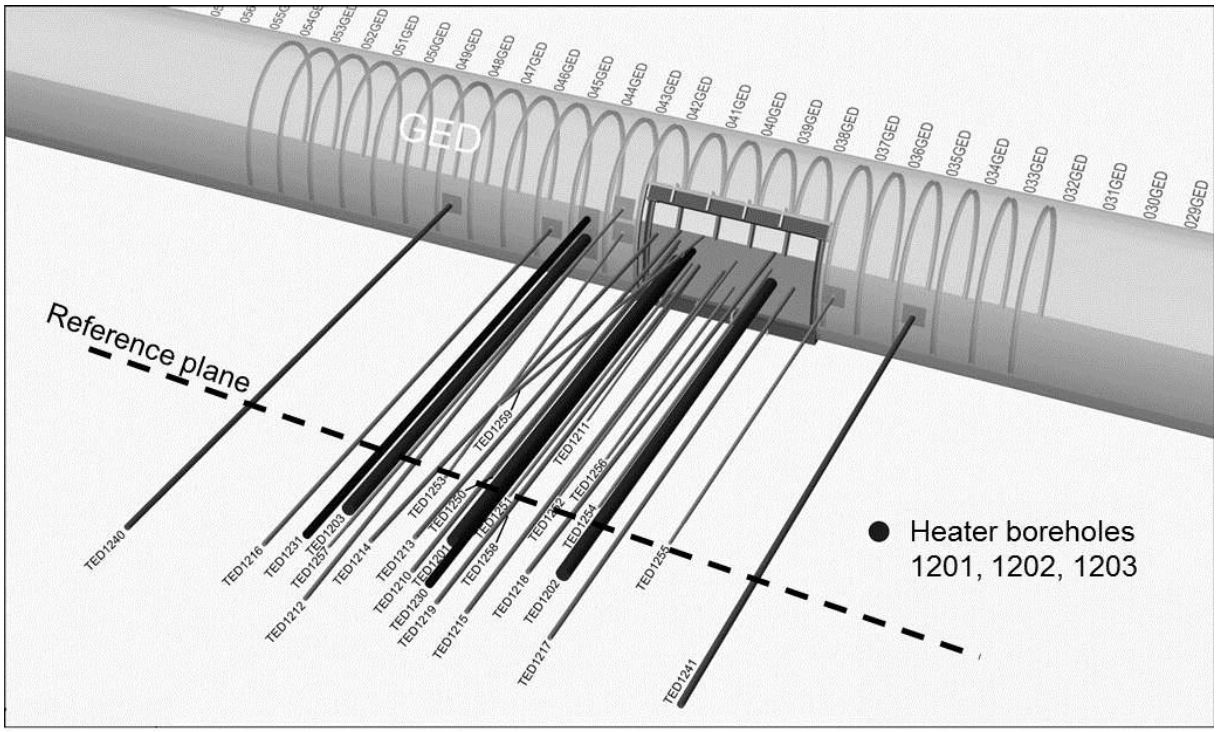

Fig. 4-11: Location of boreholes in the TED area (modified after Conils, 2012)

Thermal conductivity

Thermal conductivity and thermal diffusivity have been measured at an uniaxial pressure of p = 2.0 MPa. The measurements were carried out by applying the divided-bar method with a measurement accuracy of about ± 1.5% (Buntebarth, 2009). The samples had a thickness of 9–11 mm and had been prepared in different directions, parallel and perpendicular to the bedding with regard to the marks given by the deliverer. All samples kept their structure during the test. A small water loss of 0.5 % maximum was observed.

First, the thermal conductivity was determined at 10 different samples at a temperature of about 38°C. All of them were taken from a vertical reference plane at a depth of about 14 m (Fig. 4-11, Tab. 4-2). The results of the thermal conductivity measurements are plotted at their local coordinates on the vertical reference plane. Fig. 4-12 shows the individual results of the measurements together with the mean values parallel and perpendicular to the bedding as well as the factor of anisotropy.

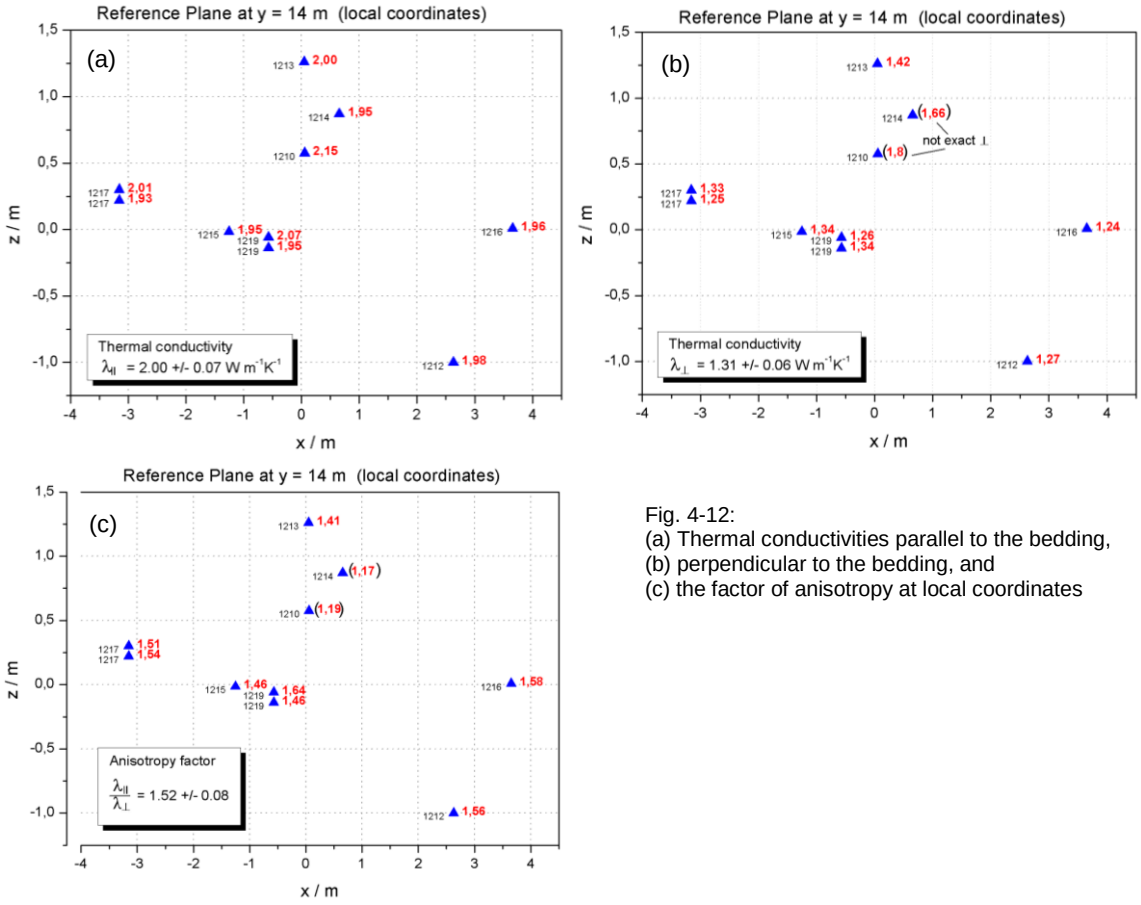

Fig. 4-12:
(a) Thermal conductivities parallel to the bedding,
(b) perpendicular to the bedding, and
(c) the factor of anisotropy at local coordinates

It has to be mentioned that for calculating the mean value for λ (⊥), the values for boreholes 1210 and 1214 were excluded as the direction of measurement was not perpendicular to the bedding but somewhere in between parallel and perpendicular. This is also reflected by the conductivity values, which are higher than all the other λ (⊥) and lower than all λ (||) values. Those two values were also excluded for calculating the factor of anisotropy.

The aim of measuring different samples from several boreholes was to check whether the rock thermal conductivity in the TED area is homogeneous or if local heterogeneities exist. Comparing all measured values (Fig. 4-12), no significant heterogeneities were found – at least not for the reference plane. The scattering of the measured values is considerably low, indicating that the thermal conductivity is rather uniform.

In the following measurement campaign, samples that were not from the reference plan were measured in order to check for heterogeneities in the third dimension. In addition, these samples were used to determine the dependence of the thermal conductivity on the temperature and water content. Fig. 4-13 gives an overview of all measurements at 38°C. The two horizontal lines are the mean values of the thermal conductivity calculated from the samples taken from the reference plane only (grey area, 14 m depth). The values obtained from the samples of the heater boreholes at different depths (5.5 m and 9.5 m) are plotted in the white area. Except for one, all the values are below the mean value of the reference plane values.

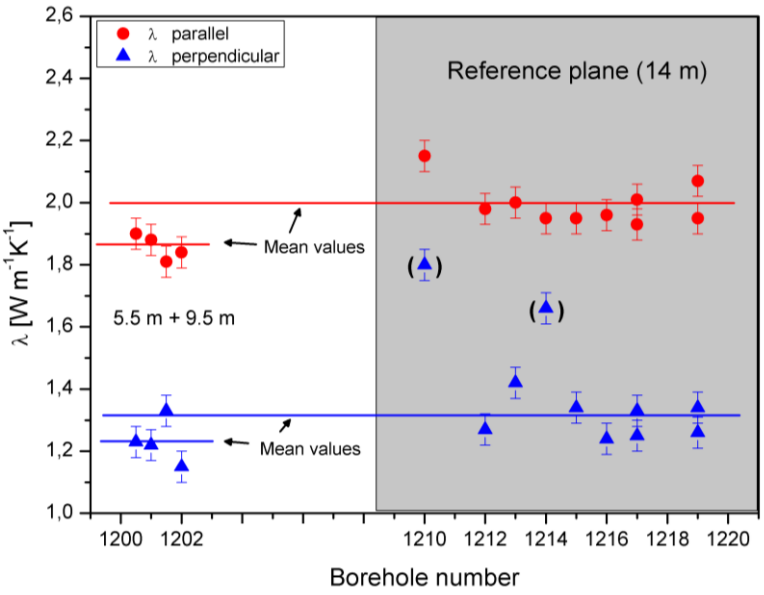

Looking at all values, it seems as if the values at lower depths are slightly lower than those from the reference plane, especially for those parallel to the bedding. Table 3 gives an overview of the mean values obtained at different depths.

Fig. 4-13: Thermal conductivity values obtained at 38°C from samples taken from the reference plane and from the heater boreholes

Tab. 4-3: Mean values of thermal conductivity

	λ (∥) W m^{-1}K^{-1}	λ (⊥) W m^{-1}K^{-1}	f_A
14 m reference plane	2.00 ± 0.07	1.31 ± 0.06	1.52 ± 0.08
5.5 m + 9.5 m	1.86 ± 0.04	1.23 ± 0.07	1.51 ± 0.10
All samples	1.96 ± 0.09	1.28 ± 0.07	1.52 ± 0.08

Figure 4-14a and 4-14b show the dependence of the thermal conductivity on temperature and water content. As can be seen from figure 4-14a, the temperature dependence is very low. Looking at the scattering of the results, especially looking at the temperature range up to 100°C, one could even say that the thermal conductivity is more or less independent of temperature.

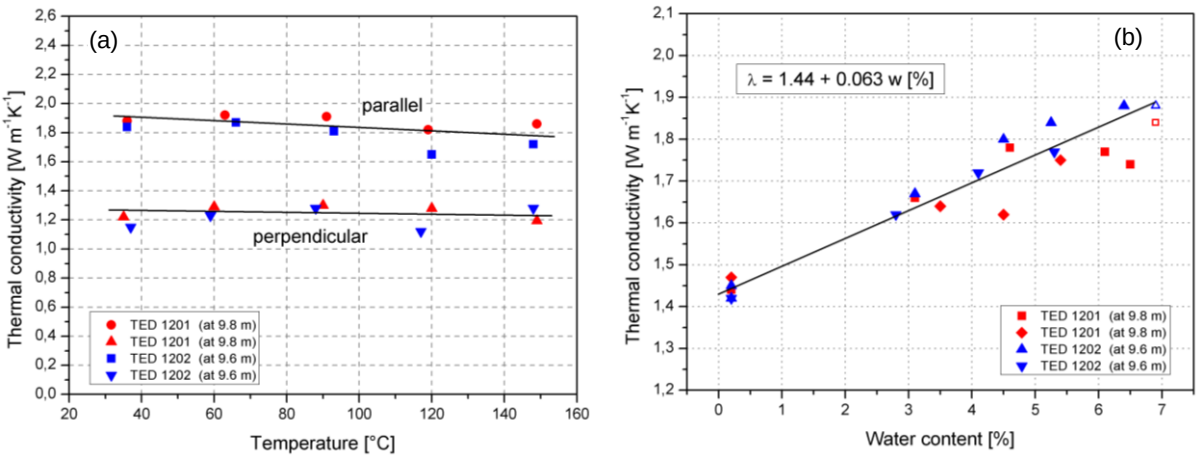

Fig. 4-14: (a) Thermal conductivity versus temperature parallel and perpendicular to the bedding, (b) thermal conductivity versus water content parallel and perpendicular to the bedding.

In contrast to this, it is obvious that the thermal conductivity heavily depends on water content (Fig. 4-14b). Thinking of slightly de-saturated zones near the heaters or the drifts, the dependence on water content described in equation (4-4) may be applied during the numerical simulations.

$$\lambda = 1.44 + 0.063 \cdot w \qquad (4\text{-}4)$$

With λ = thermal conductivity [W m^{-1} K^{-1}] and w = water content [%]

Thermal diffusivity

The thermal diffusivity is proportional to the thermal conductivity. The same pressures and temperature were used as in the thermal conductivity tests. The accuracy of the measurements is ± 10%.

The factor of anisotropy is very similar to the one of thermal conductivity (reference plane). As far as the values of borehole TED1210 and TED1214 are concerned, the same remark as for the thermal conductivity is valid. Figures 4-15a,b,c show the values at their local coordinates in the reference plane. At least for the reference plane, no significant heterogeneities were found. The scattering of the measured values is rather small, which indicates that the thermal diffusivity is rather uniform.

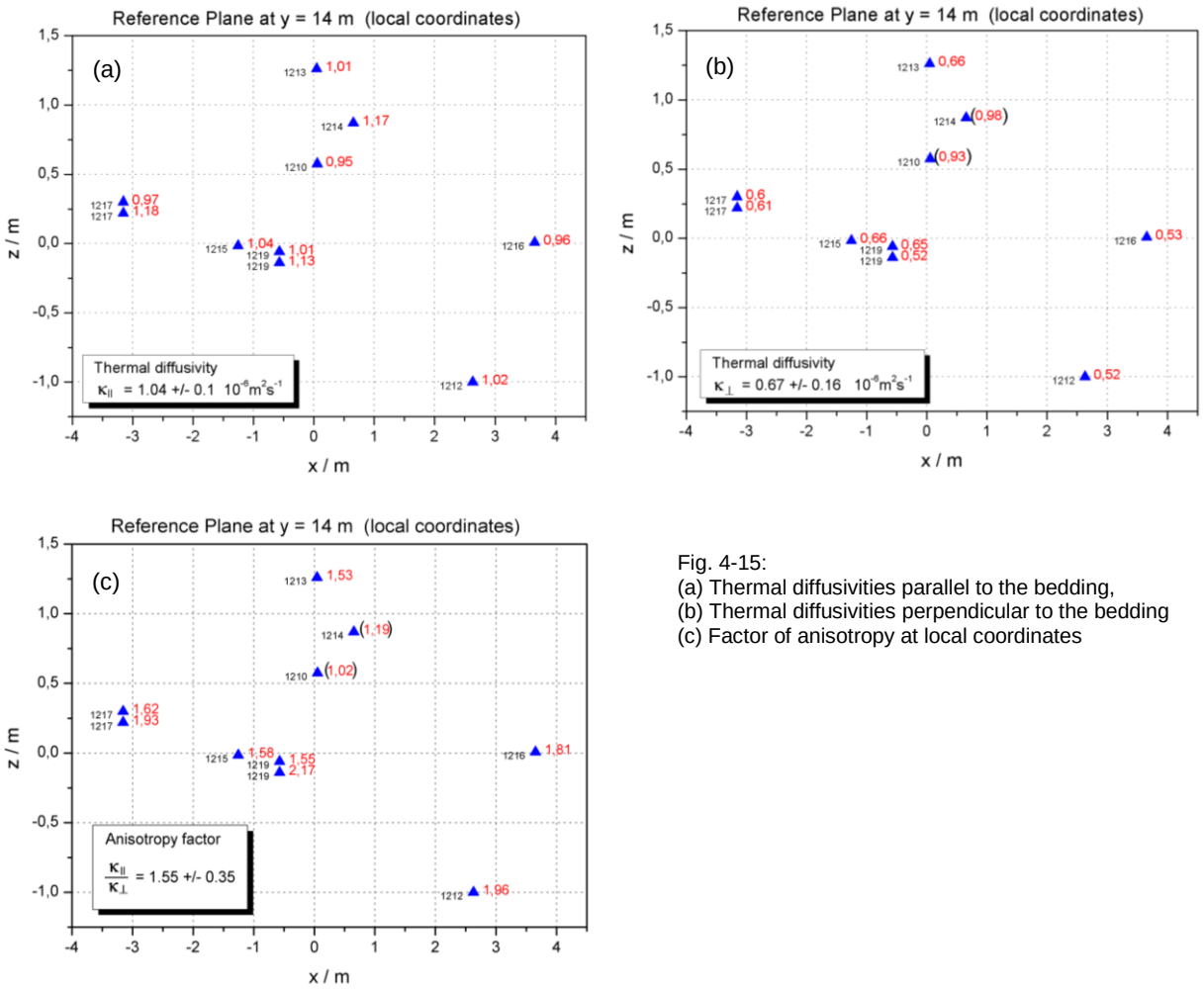

Fig. 4-15:
(a) Thermal diffusivities parallel to the bedding,
(b) Thermal diffusivities perpendicular to the bedding
(c) Factor of anisotropy at local coordinates

Taking into account the values of the samples from the heater borehole at a depth different from the reference plane, it was found that these values are all below the mean value of the

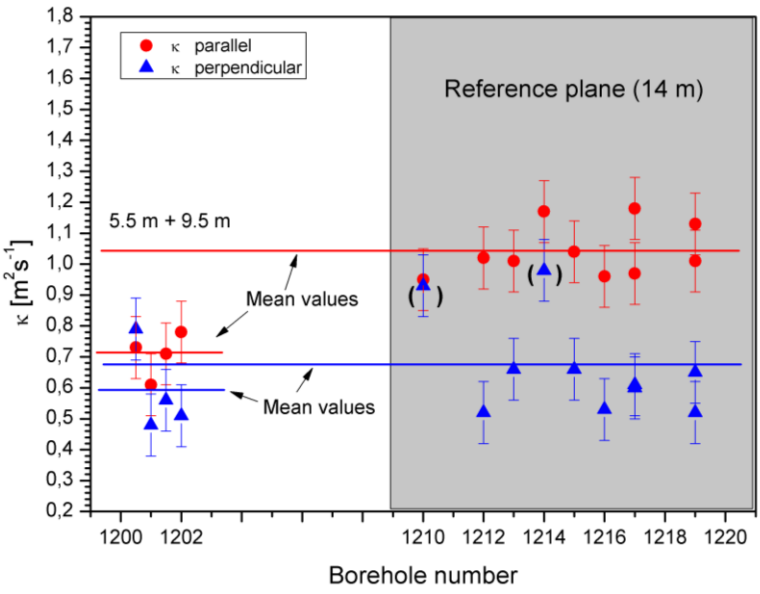

reference plane. This is similar to the findings for the thermal conductivity but more significant, at least for the samples measured parallel to the bedding (Fig. 4-16).

Fig. 4-16: Thermal diffusivity values at a termperature of 38°C of samples taken from the reference plane and from the heater boreholes.

Table 4-4 gives an overview of the different mean values obtained at different depths.

Tab. 4-4: Mean values of thermal diffusivity

	κ (‖) $m^2 s^{-1}$	κ (⊥) $m^2 s^{-1}$	f_A
14 m reference plane	**1.04** ± 0.09	**0.67** ± 0.16	**1.64** ± 0.35
5.5 m + 9.5 m	**0.71** ± 0.07	**0.59** ± 0.14	**1.25** ± 0.25
All samples	**0.95** ± 0.18	**0.64** ± 0.16	**1.53** ± 0.36

In figure 4-17, the temperature dependence of the thermal diffusivity is shown as obtained from the samples taken from the heater boreholes out of the reference plane. The scattering is higher than for the thermal conductivity, especially for the samples measured parallel to the bedding. In contrast to the thermal conductivity a small temperature dependence was found, even in the temperature range up to 100°C.

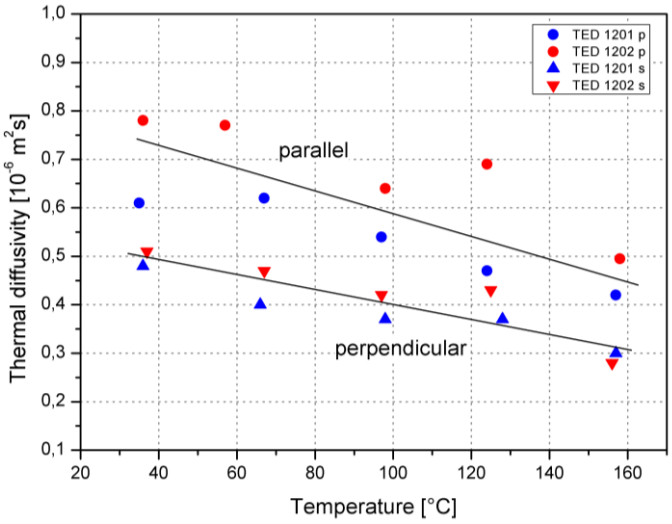

Fig. 4-17: Thermal diffusivity versus temperature

Specific heat capacity

The specific heat capacity was measured by a heatflux-difference calorimeter (Netzsch Typ 404). The measured values of the specific heat capacity are compiled in table 4-5. The values were obtained at a temperature of 20°C. At this temperature, the water loss during the measurement is negligible and the values are assumed to represent the specific heat capacity of the clay-water mixture.

Tab. 4-5: Measured values of specific heat capacity at T = 20°C

Sample ID	Borehole	c_p
		J kg^{-1}K^{-1}
EST 33791	TED 1210	646
EST 33734	TED 1212	885
EST 33837	TED 1213	840
EST 33705	TED 1214	861
EST 33863	TED 1215	588
EST 33681	TED 1216	1106
EST 33765	TED 1217	693
EST 33769	TED 1217	671
EST 33885	TED 1219	724
EST 33889	TED 1219	769
EST 34674	TED 1201	1150
EST 34715	TED 1202	1060

The mean values obtained from table 4-5 are:

Reference plane 14 m $c_p = 778 \pm 50$ J kg^{-1}K^{-1}
All samples $c_p = 828 \pm 190$ J kg^{-1}K^{-1}

Density

All samples prepared for thermal conductivity measurements parallel and perpendicular to the bedding were used to measure the densities. The results are given in table 4-6.

Tab. 4-6: Measured densities of all samples prepared

Sample ID	Borehole	Density (‖)	Density (⊥)
		kg m^{-3}	kg m^{-3}
EST 33791	TED 1210	2420	2420
EST 33734	TED 1212	2380	2360
EST 33837	TED 1213	2380	2390
EST 33705	TED 1214	2400	2415
EST 33863	TED 1215	2340	2350
EST 33681	TED 1216	2340	2380
EST 33765	TED 1217	2370	2370
EST 33769	TED 1217	2370	2350
EST 33885	TED 1219	2390	2360
EST 33889	TED 1219	2390	2380
EST 34674	TED 1201	2380	2390
EST 34715	TED 1202	2370	2400

The mean value for all samples is:

$\varphi = 2378 \pm 23$ kg m^{-3}

Differential thermal analysis (DTA)

For the DTA, about 10g of the core sample were pulverized in a mortar, about 200 mg of which were analysed. Claystones are not very hard and can easily be ground. All 10 samples show several identical, very pronounced reactions at the following temperatures:

99 – 111°C: Release of water from clay minerals (illite/montmorillonite), endothermal
574 – 585°C: Conversion of montmorillonite, mica minerals (illite), and chlorite, endothermal
838 – 866°C: Decomposition of calcite, siderite, ankerite, and mica (illite), endothermal
900 – 905°C: Decomposition of chlorite, exothermal

Using weak endothermal reactions as a criterion, the 10 samples that were analysed can be categorized into 3 groups, which differ in their carbonate compositions. These are samples with:

1. Calcite and siderite (between 930°C and 940°C and at approx. 870°C)
2. Siderite (very week endothermal calcite reaction between 930°C and 940°C, thus siderite only)

3. Calcite, siderite, and ankerite (additional reaction at 780°C: decomposition of $MgCO_3$ components from the ankerite)

Group 1 comprises the samples: TED 1212, 1217.2, 1219.1 (Fig. 4-18a)
Group 2 comprises the samples: TED 1215, 1216, and 1217.1 (Fig. 4-18b)
Group 3 comprises the samples: TED 1210, 1213, 1214, and 1219.2 (Fig. 4-18c)

This categorization does not mean that carbonates that were not identified are not present but that their contents are so low that they cannot be detected. To be able to detect the carbonate content in the DTA, core sample TED 1210 was treated with hydrochloric acid, dried, and subsequently analysed. In addition to the exothermal reactions, which take place at temperatures between 200°C and 500°C and under ambient pressure, only the montmorillonite/illite/chlorite reactions are measured in the carbonate-free DTA (Fig. 4-18d). The reactions are oxidation and rearrangement of water and cations in the phyllosilicates. The carbonates may also contain ferrous dolomite instead of ankerite. The difference cannot be detected with this method.

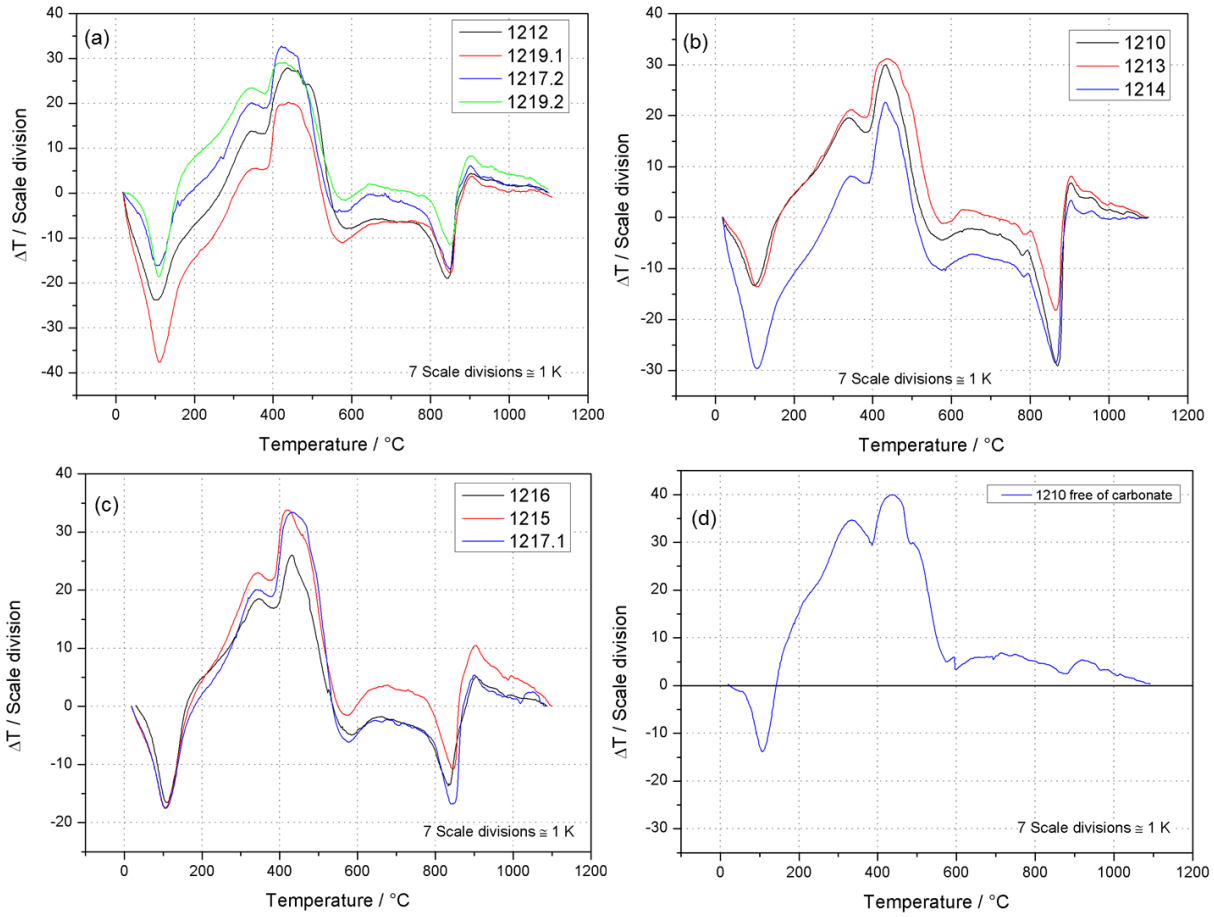

Fig. 4-18: (a): DTA of core samples high in calcite/siderite content, (b) DTA of core samples high in siderite content, (c) DTA of core samples high in calcite/siderite/ankerite content, (d) DTA of core sample TED1210, but free of carbonate.

Carbonate content

When the sample is treated with hydrochloric acid, the carbonates are broken down and carbon dioxide is released. This reaction is used to measure an increase in pressure in a closed chamber. The closed glass chamber has a volume of approximately 600 cm³; the differential pressure manometer has a graduation of 10 Pa. The chamber contains 30 ml of 3% HCl and the sample. The sample is placed in a sample holder, which can be rotated from the outside

so that the sample falls into the acid. The pressure increase caused by the chemical reaction is calibrated against pure calcite and has a resolution of α = 20 Pa/mg$CaCO_3$.

This method can detect calcite, which is easily soluble, and possibly ankerite/dolomite. Siderite does not react as quickly, and, as the reaction lasts only a few seconds, siderite can only be partly registered at most. Pyrite could also be analysed, but only traces of pyrite exist and only in a few samples as shown by the streak (powder colour) when the sample is dragged across a streak plate. The method is highly temperature-sensitive. Heating of the acid to accelerate the reaction is thus not possible. Hence, it is necessary to conduct the experiments in as little time as possible.

Approximately 10 g of the samples under study are crushed and mixed. Approximately 0.5 g of the mixture is ground to a fine powder in an agate mortar. Between 30 and 50 mg of this lot are placed in the chamber. Three measurements, which are subsequently averaged, are performed on each lot.

The carbonate contents of the samples vary considerably. However, only a single sample was taken from each core sample; the homogeneity within a core sample was not investigated. The calcite contents of the samples are shown in table 6. The contents vary between 7 and 47% $CaCO_3$. For two samples a $CaCO_3$ content of more than 40% was determined, which seems to be rather high. Although the carbonate contents vary considerably, an influence on the thermal properties λ, κ, and c_p and thus a correlation between carbonate content and thermal properties was not observed.

Tab. 4-7: Calcite contents and densities of the samples

Sample ID	Borehole	$CaCO_3$	Density
		%	kg m^{-3}
EST 33791	TED 1210	43	2.42
EST 33734	TED 1212	27	2.36
EST 33837	TED 1213	28	2.39
EST 33705	TED 1214	47	2.415
EST 33863	TED 1215	13	2.35
EST 33681	TED 1216	31	2.38
EST 33765	TED 1217	7	2.37
EST 33769	TED 1217	9	2.35
EST 33885	TED 1219	17	2.36
EST 33889	TED 1219	11	2.38
EST 34674	TED 1201	22	2.39
EST 34715	TED 1202	26	2.40

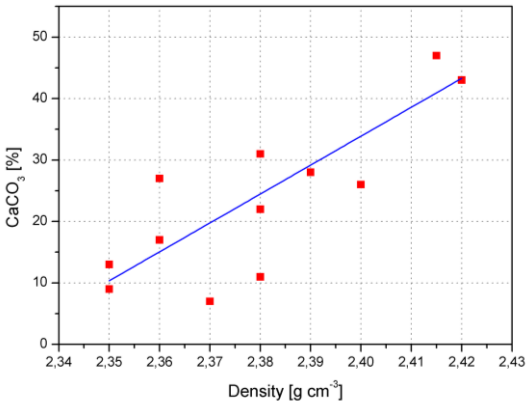

Fig. 4-19: Correlation of density and carbonate content

A comparison of the densities with the carbonate contents shows that rocks high in carbonate have a higher density at ρ = 2400 kg m^{-3} compared with ρ = 2380 kg m^{-3} for rocks with a lower carbonate content. The table shows the densities of core samples that were taken perpendicular to the drill axis because they comprise more layers than those taken parallel to the drill axis. The correlation of calcite content and density is shown in figure 12.

Thermal expansion

The linear thermal expansion was measured with a NETZSCH dilatometer. The sample length was 25-50 mm and the diameter was 3–10 mm. A thermo element measures the data directly at the sample. The heating rate is 2 K/min at temperatures of 10–320°C.

The thermal expansion was measured on 2 samples from the heater borehole and the thermal expansion coefficient was determined (Tab. 4-8).

Tab. 4-8: Thermal expansion coefficient

Sample ID	Borehole	α (||) 10^{-6} K^{-1}	α (⊥) 10^{-6} K^{-1}
EST 34674	TED 1201	9.0	18.9
EST 34715	TED 1202	11.9	16.7
Mean value		**10.5**	**17.8**

The factor of anisotropy is f_A = **0.6** and is thus the opposite of the factor determined for thermal conductivity and diffusivity.

IR Spectroscopy

The infrared spectroscopy measurements were carried out with a PERKLIN-ELMER device type 1650. The material of investigation was mixed with 250 mg KBr and compressed to a small pellet. The spectral area investigated was between wave numbers 4000 cm^{-1} and 400 cm^{-1} which refers to wavelengths in the range of 2.5 µm to 25 µm.

The two investigated samples from the two heater boreholes have an identical mineral composition (Fig. 4-20, Tab. 4-9). The characteristic absorption bands of clay minerals are within the wave number range of 3700 to 3430 cm^{-1}. These bands are related to montmorillonite, Illite, halloysite and metahalloysite. The bands between 2520 and 1430 cm^{-1} are caused by calcite and ankerite. The absorption at 1620 cm^{-1} is caused by dolomite with higher amplitude at 2520 cm^{-1}, which indicates a higher calcite content in the sample from borehole 1202. The absorption at 1030 to 912 cm^{-1} is due to the minerals Halloysite and metahalloysite as well as illite and muscovite. Between 874 and 712 cm^{-1} calcite and quartz was identified.

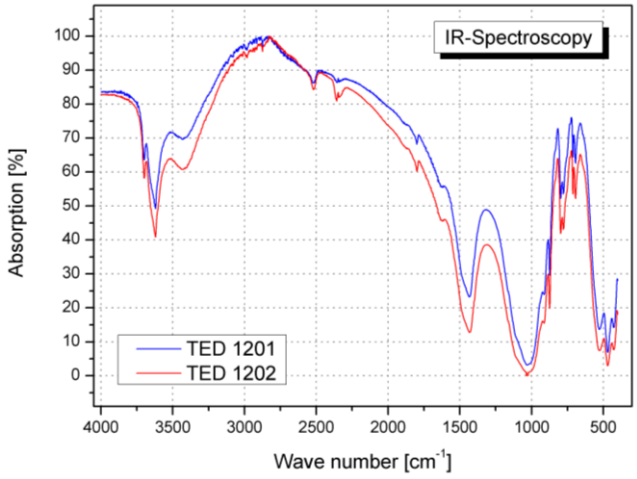

Fig. 4-20: IR spectroscopy results

Tab. 4-9: Absorption bands related to minerals identified

Wave number (cm^{-1})	Mont-morillonite	Halloy-site	Metahal-loysite	Illite	Musco-vite	Calcite	Dolomite	Ankerite	Quartz
3698	x	x	x						
3620		x	x	x					
3430		x	(x)						
2520						x			
1800						x			
1622-18							x		
1434-30						x	x	x	
1032-28		x	x	x	x		x		
912		x	x						
874						x		x	
798									x
778									x
712						x			
694		x							
528-26					x				
470	x				x				
428-26					x			x	

4.3.2 Heater test

A second step to characterize the THM behaviour of the clay stone is to perform a back-analysis of an in-situ test and of the measured values of THM parameters in observation boreholes. The design of the in-situ heater test is shown in Fig. 4-11. The heater test set-up consists of 3 heater boreholes and 21 instrumented observation boreholes. Each heater is 4 m long and generates a thermal power of 1500 W. The distance between the heaters is 2.6 m in order to approximate the geometry of the planned disposal cells. The surrounding boreholes were strategically located to take into account the anisotropic THM behaviour of the claystone (Fig. 4-11). There are 12 boreholes for pore pressure measurements, 9 boreholes for temperature measurements, and 2 boreholes for deformation measurements. To optimize and simplify the inverse problem analysis, special attention was paid to the reduction of uncertainties regarding the sensors' locations in the boreholes. The incorrect determination of sensor locations in the previous thermal experiment was found to be a very problematic issue for analysis and parameter determination (Garitte et al., 2010).

The central heater was activated on January 25, 2010, starting with a relatively low heating power of 150 W. Subsequently, the heating power was increased to 300 W and finally to 600 W. Each step was about four months long. After one year, the two surrounding heaters were activated, and the same heat load was applied. Before proceeding to the next heating step, permeability tests were performed in all pressure measurement boreholes to investigate the impact of the heat on the permeability of the rock.

One possibility to identify the THM parameters of the claystone is to perform a series of forward simulations by adjusting the THM input parameters until the calculation results fit best to the values measured at the different sensor locations. Given the large number of sensors to consider, and based on experience from former experiments at the Meuse/Haute-Marne and Mont Teri underground research labs (Garitte et al., 2010; Jobmann & Polster, 2007; Wileveau et al., 2007), doing this fitting process manually is a long and laborious task. Thus, an automatic parameter identification process as already described in section 2.2 was applied .

Model description

In view of calculation time, the geometric model size and mesh discretization of the model have to be chosen carefully because dozens of simulations are needed for the calibration procedure. At the same time, the boundary conditions have to be placed far enough so that they have only insignificant influence on the results. Therefore, different model sizes and discretization levels were tested to find a model that shows the best compromise between accuracy of the results and adequate calculation time.

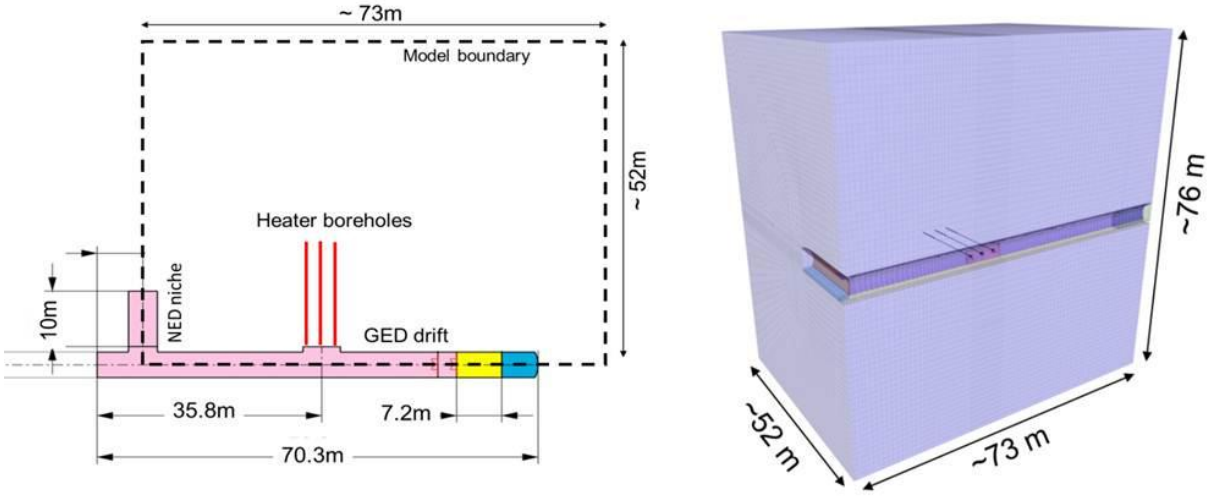

Fig- 4-21: Model domain and numerical mesh

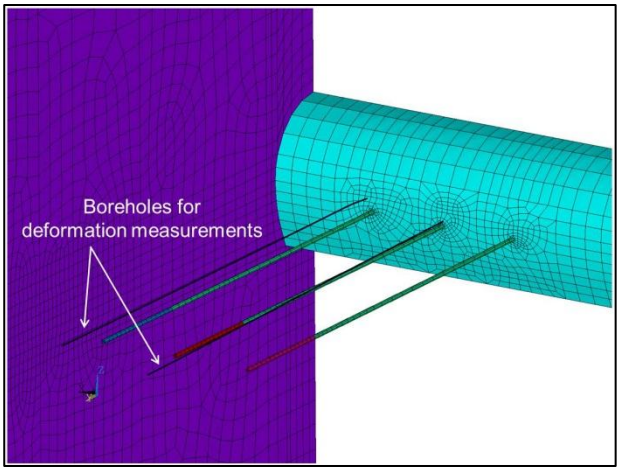

Fig. 4-22: Location of considered boreholes in the model

Good convergence behaviour in the mechanical analysis is achieved by ensuring that the sweep meshing capabilities of ANSYS produce brick only meshes that have controlled element edge length conditions. The total model domain and the mesh are shown in Figure 4-21. In total, 300.000 elements were used. The model domain contains the tunnel and the niche at the URL with shotcrete surfaces, the three boreholes with the heaters, and two observation boreholes intended for mechanical deformation measurements (Fig. 4-22). The latter act as hydraulic sinks in the domain and have therefore been considered in the model. For FEM modelling, 8 node solid elements which have temperatures, hydraulic heights, and displacements as degrees of freedoms were used.

Constitutive models

The process of the THM coupled simulations is based on the solution of the thermal-hydraulic and nonlinear mechanical analyses using forward coupling at discrete time steps. All analyses are coupled with explicit forward schemata; i.e., material parameters and loads in the next step are updated depending on the results of the previous steps. The following important couplings are taken into account: update of pore pressure as a result of temperature change (T→H) including effects on stress strain fields from thermal expansion (T→M); update of hydraulic conductivity depending on the stress state as well as on plastic strain (damage, fracturing) (M→H); update of pore pressure as a result of stress-induced deformation (M→H); and update of effective stresses as a result of pore pressure changes (H→M).

The following couplings with second order influence were neglected: degree of water saturation and effect of convection (H→T) and stress strain effects on thermal conductivity (M→T). The following balance equations and transport laws were used:

- Equation of motion and equilibrium (mechanical nonlinear analysis)
- Equation of energy balance (thermal analysis)
- Equation of fluid-mass balance (hydraulic analysis)
- Fourier's Law of heat conduction
- Darcy's Law of fluid flow in a porous medium

For numerical solution of heat-flow problems, the code uses the equation of energy balance and transport laws, which are derived from Fourier's Law of heat conduction. The energy balance equation can be written in the following differential expression:

$$- \text{grad } q^t + q^t_v = \rho\, c\, dT/dt \qquad (4\text{-}5)$$

where q^t is the heat-flux vector [W/m^2], q^t_v is the volumetric heat-source intensity [W/m^3], ρ is the density [kg/m^3], c is the specific heat at constant volume [J / kg·K], T is the temperature [°C] and t is the time [s]. Transport of heat is taken into account by heat conduction. The relation between heat flux and temperature gradient (Fourier's Law) for anisotropic case can be written in the following form:

$$q^t = -\lambda \text{ grad } T \qquad (4\text{-}6)$$

Where λ is the thermal conductivity tensor [W / m·K]. The forward coupling to the mechanical stress calculation is carried out via the thermal expansion coefficient α_s. Thermal-strain increments ε^T associated with the free expansion corresponding to temperature change ΔT:

$$\Delta\varepsilon^T = \alpha_s \, \Delta T \delta \tag{4-7}$$

Where α_s is the coefficient of linear thermal expansion [1/K], ΔT is the temperature difference [K], and **δ** the Kronecker delta. For numerical solution of fluid-flow problems, the equation of fluid-mass balance and Darcy's law of fluid transport in a porous medium are used. The fluid-mass balance equation can be given in the following form:

$$\text{grad } q^f + q^f_v = d\zeta/dt \tag{4-8}$$

where q^f is the specific discharge vector [1/s], q^f_v is the volumetric fluid source intensity [1/s], ζ is the variation of fluid volume per unit volume of porous material due to diffusive fluid mass transport, and t is time [s]. The relation between the specific discharge vector and the pore pressure is defined by Darcy's law. For the anisotropic case, it can be given in the form:

$$q^f = -k / \mu(T) \; grad(P_p - \rho_f g \, z) \quad \text{or} \quad q^f = -k \, \rho_f g / \mu(T) \; grad(h) \tag{4-9}$$

Where k is the permeability tensor [m^2], $\mu(T)$ is the temperature-dependent fluid viscosity [Pa·s], P_p is the pore pressure, ρ_f is the fluid density [kg/m^3], g is the gravity acceleration [m·s^{-2}], and $h=P_p/g\rho_f + z$ is the hydraulic head [m]. Single-phase flow is considered in the simulation. The anisotropic permeability tensor depends on the stress state as well as on the plastic strain.

$$k_i = k_{\sigma,i} + k_{\varepsilon,i} \qquad \text{for } i=x, y, z \tag{4-10}$$

An exponential relation between intrinsic permeability and stress state is introduced for permeability parallel to bedding plane $k_{\sigma,x} = k_{\sigma,y}$ and perpendicular to bedding plane $k_{\sigma,z}$ as follows (Millard et al., 2005) :

$$k_{\sigma,x} = k_{\sigma,y} = k_{\sigma,p} = k_{0,p} \times \left(\frac{\sigma_z}{\sigma_0} \right)^{-n_p} \qquad k_{\sigma,z} = k_{\sigma,n} = k_{0,n} \times \left(\frac{\sigma_{m,h}}{\sigma_0} \right)^{-n_n} \tag{4-11}$$

Where σ_0 = 1.0 MPa, σ_z is the vertical stress, $max\ k_{\sigma,x} = max\ k_{\sigma,y} = 100\ k_{0,p}$ *(für* $\sigma_z \rightarrow 0$*)*, $k_{0,p}$, n_p, $k_{0,n}$, n_n are parameters to be adjusted, $\sigma_{m,h}=(\sigma_x + \sigma_y)/2$ is the mean value of horizontal stresses and $max\ k_{\sigma,z} = 100\ k_{0,n}$ *(für* $\sigma_{m,h} \rightarrow 0$*)*. Permeability change caused by plasticity is considered as linearly dependent on the sum of plastic strains in the plane perpendicular to the considered direction:

$$\begin{aligned} k_{\varepsilon,x} &= k_\varepsilon \, (\varepsilon_y^+ + \varepsilon_z^+), \quad k_{\varepsilon,x} \le k_{\varepsilon,max} \\ k_{\varepsilon,y} &= k_\varepsilon \, (\varepsilon_x^+ + \varepsilon_z^+), \quad k_{\varepsilon,y} \le k_{\varepsilon,max} \\ k_{\varepsilon,z} &= k_\varepsilon \, (\varepsilon_x^+ + \varepsilon_y^+), \quad k_{\varepsilon,z} \le k_{\varepsilon,max} \end{aligned} \tag{4-12}$$

Where ε_x^+, ε_y^+, ε_z^+ are plastic strains in directions x, y, z and $\varepsilon_i^+ = \varepsilon_i^{pl}$ for $\varepsilon_i^{pl} \ge 0$ and $\varepsilon_i^+ = 0$ for $\varepsilon_i^{pl} < 0$. k_ε is the permeability, and $k_{\varepsilon,max}$ is the maximum permeability. Changes in the variation of pore pressure P_p are linearly related to changes in fluid content ξ, volumetric strain ε_v and temperature T by the following constitutive law (Narasimhan, 2006):

$$\frac{1}{M}\frac{\partial P}{\partial t} = \frac{\partial \zeta}{\partial t} - \alpha \frac{\partial \varepsilon_v}{\partial t} + \beta \frac{\partial T}{\partial t} \tag{4-13}$$

Where M is the Biot modulus [Pa], α is the Biot coefficient [-], $\varepsilon_v = \varepsilon_{v,thermic} + \varepsilon_{v,elastic} + \varepsilon_{v,plastic}$ and β the undrained thermal coefficient [1/K] defined as:

$$\beta = 3\,[\alpha_s\,(\alpha - n) + \alpha_{f,fact}\,\alpha_f(T)\,n] \qquad (4\text{-}14)$$

Where α_s is the linear thermal expansion coefficient for grains [1/K], $\alpha_f(T)$ is the temperature-dependent linear thermal expansion coefficient for fluid [1/K], n is the porosity, and $\alpha_{f,fact}$ is the factor of $\alpha_f(T)$, which was introduced as a parameter for sensitivity analysis and calibration that allows the consideration of different types of pore fluids.

Due to the bedding of the Callovo-Oxfordian clay, it is very important to take into account the anisotropy of elastic mechanical behaviour and hydraulic conductivity behaviour. In addition, a Mohr-Coulomb based elasto-plastic behaviour was defined for the rock matrix as well as for the bedding plane. The behaviour considers shear and tensile failure including softening after the initial strength values are violated.

Initial and boundary conditions

When calibrating complex non-linear time-depended problems, the model initialization is very important. The impacts of tunnel excavation and heater placement on the temperature and pore pressure fields were covered by explicitly modelling every excavation and heater placement with regard to their excavation schedule. The whole model domain is initialized at starting time t = -605 days (t = 0 was set as the start of the heating) with a constant temperature of 21.5°C, constant hydraulic height (438.33 m), and initial anisotropic total stress. The boundary conditions for thermal and hydraulic analysis were defined at the model surfaces as fixed or perfectly insulated. For the mechanical analysis, zero displacements were applied normal to the surface at the sides as well as at the lower boundary of the model. The upper boundary was loaded with a pressure that represents the weight of the upper layers. Prior to the excavation of all the tunnels (at t = -606.17 days), the initial stress state was defined as shown in Figure 4-23 (Vymlatil & Schlegel, 2013, Conil, 2012).

Later on, the boundary conditions were adjusted during the excavating and drilling of boreholes by introducing new boundary conditions on free surfaces of excavation caverns and boreholes (measured tunnel temperature and zero pore pressure on free surfaces). The tunnel and niche excavation was done in 115 steps (time -604 ... -234.5 days) by deactivating and activating tunnel and lining elements. The same procedure was used to simulate the drilling of the three heater boreholes where clay was deactivated and heater elements activated at the installation times of the heaters. The influence of the two observation boreholes next to the heater boreholes were taken into account as well. On their longitudinal axes, zero pore pressure was set from the time of drilling.

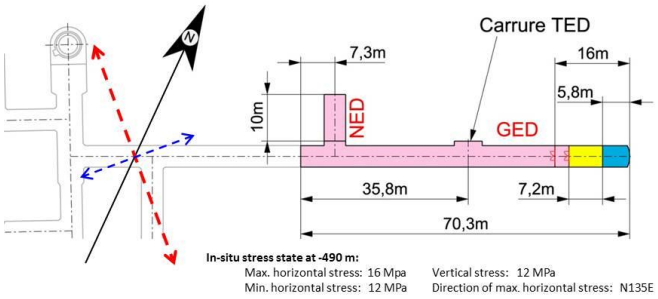

Fig. 4-23: Initial stress state

Temperature evolution

The basic THM simulation carefully modelled the experiment including the tunnel excavation, the heater boreholes, and all heating phases. The thermal analysis only slightly depends on hydraulic or mechanical processes but is the driving force for all the hydro-mechanical processes in the experimental area. Therefore, the thermal rock material properties were calibrated separately at the beginning to ensure a good representation of the temperature evolution in the model. Fig. 4-24 shows the location of the temperature sensors as a top view onto the horizontal x-y-plane. The sensors are located in eight observation boreholes at different distances to the test drift. The three thick lines represent the locations of the heaters. The initial input parameters taken as starting values for the parameter identification were obtained from laboratory investigations on core samples and are given in Table 4-10.

Tab. 4-10: Initial and final thermal properties of the back analysis

Input parameter		Initial values	Final values
Density	ρ (kg m^{-3})	2378	2333
Horizontal thermal conductivity	λ (W m^{-1}K^{-1})	2.00	2.02
Vertical thermal conductivity	λ (W m^{-1}K^{-1})	1.31	1.37
Specific heat capacity	c (J kg^{-1}K^{-1})	828	695

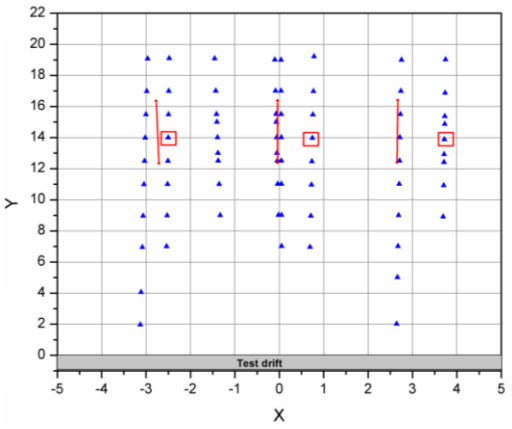

Fig. 4-24:
Location of temperature sensors and heaters (top view)

For comparison, the best design parameter set found after 40 simulation runs controlled by optiSLang is given in the table as well. It shows that the final values of the numerical back analysis of the in-situ test are quite close to the initial ones found in the laboratory. Figure 4-25 (left) shows a comparison of the measured and calculated “best design” temperature evolutions for three selected sensors. The locations of these sensors are marked in Figure 4-21 with a square. The good fitting is evident. In Figure 4-25 (right) the differences between measured and calculated values are given for the eight sensors located at a distance of 14 m from the test drift (reference plane, grey line in Figure 4-24). The differences are less than 0.8 K. This was a sound basis for the following identification of the pore water pressure evolution in the experimental area.

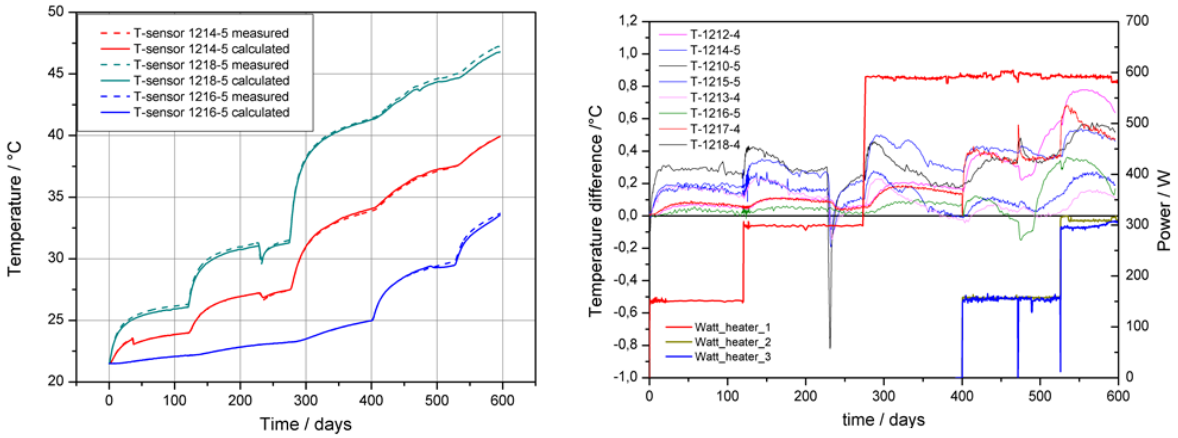

Fig. 4-25: Comparison of measured and calculated temperature evolutions for three selected sensors (left) and differences between measured and calculated values given for the eight sensors (right) located in the reference plane at a distance of 14 m to the test drift (grey line in Figure 4-24).

Porewater pressure evolution

The location of each pore pressure sensor is shown in Figure 4-26. The measured values of all total pore pressure sensors yield an inconsistent pressure distribution in the test area (Vymlatil & Schlegel, 2013). The measured values of some of the sensors seem to be implausible. Thus, for the sensitivity analysis and for the parameter identification process, only those sensors were selected that deliver plausible and consistent results. These are the sensors 1251, 1252, 1253, 1255, 1258, and 1259 numbered 1,2,3,5,8,9 in the following. Due to several uncertainties regarding the effects of prior excavations and the fact that the main focus of the parameter identification is on the effect of the heating on the host rock, the analysis was limited to the heating test itself. This means that the analysis starts with the start of the first heating phase (t=0). Any pore pressure effects prior to the heating were neglected so that only the pore pressure difference resulting from the heating was analysed.

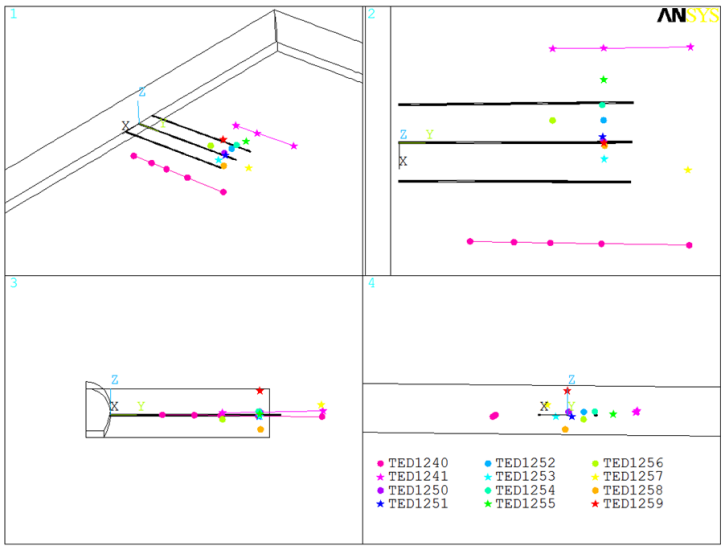

Fig. 4-26: Overview of pore pressure sensor locations in TED area.

After the boundary conditions had been adjusted with the help of the initial best guesses for all rock parameters, the design (parameter set) seemed plausible. This design, together with windows of uncertainty of about ±20%, was used to perform a sensitivity analysis. The input parameters are listed in Table 4-11. All parameters not listed in Table 4-11 were taken as constant and listed in Tables A2.4 to A2.6 in appendix 2.

Tab. 4-11: Input parameters and their ranges defined for the sensitivity analysis

Input parameter		Name	Min-Value	Max-Value
Elastic parameters (transversal isotropy)	E_p (Pa)	*E_p*	6.58E+09	9.88E+09
	E_n (Pa)	*E_n*	4.59E+09	6.88E+09
	ν_p (-)	*PR_p*	0.24	0.36
	ν_{np} (-)	*PR_np*	0.24	0.36
	G_{np} (Pa)	*G_np*	2.16E+09	3.24E+09
Friction angle (rock matrix)	φ_g (°)	*Phig*	20.00	30.00
Dilatancy angle (rock matrix)	ψ_g (°)	*Psig*	8.00	12.00
Cohesion (rock matrix)	c_g (Pa)	*Cg*	3.60E+06	5.40E+06
Tension cut off (rock matrix)	σ_t (Pa)	*Sigt*	1.04E+06	1.56E+06
Coefficient of residual strength (rock matrix)	$\varphi_{gr,fact}$ (-)	*PhirFact*	0.56	0.84
	$c_{gr,fact}$ (-)	*CrFact*	0.32	0.48
	$\sigma_{tr,fact}$ (-)	*SigtrFact*	0.32	0.48
Dilatancy angle (bedding)	φ_1 (°)	*Phi1*	16.00	24.00
Cohesion (bedding)	c_1 (Pa)	*C1*	1.20E+06	1.80E+06
Tension cut-off (bedding)	σ_{t1} (Pa)	*Sigt1*	4.00E+05	6.00E+05
Coefficient of residual strength (bedding)	$\varphi_{r1,fact}$ (-)	*Phir1Fact*	0.56	0.84
	$c_{r1,fact}$ (-)	*Cr1Fact*	0.32	0.48
	$\sigma_{tr1,fact}$ (-)	*Sigtr1Fact*	0.32	0.48
Parameters of the permeability function	$k_{0,p}$ (m^2)	*Perm_K_0_p*	5.20E-19	7.80E-19
	n_p (-)	*Perm_N_p*	0.640	1.000
	$k_{0,n}$ (m^2)	*Perm_K_0_n*	1.20E-20	1.80E-20
	n_n (-)	*Perm_N_n*	0.128	0.192
	k_ε (m^2)	*Perm_K_eppl*	8.00E-15	1.20E-14
	$k_{\varepsilon,max}$ (m^2)	*Perm_K_max_eppl*	8.00E-17	1.20E-16
Scaling factor of thermal expansion (Fluid)	$\alpha_{f,factor}$ (-)	*Alpha_f_fact*	0.90	1.10
Porosity	n (-)	*n*	0.13	0.19
Thermal expansion coefficient (rock matrix)	α_s ($°C^{-1}$)	*Alpha_s*	1.13E-05	1.70E-05
Biot-Modul	M (Pa)	*M*	3.92E+09	5.88E+09
Biot-coefficient	α (-)	*Alpha*	0.60	0.95

For the sensitivity analysis, 80 designs were generated using optiSLang's Latin Hypercube sampling (Will, 2006). The responses of the sensitivity analysis are integral and discrete values of pore pressures obtained from time history signals at all measured points. From each signal, total values of pore pressure were used at time 0 and relative values (related to time 0) at times 0, 121, 275, 400, 526, 653, 1001, 1271, and 1500 days. These points represent the start and peak values of the relative pore pressure for each phase. As an example, the response times used are shown in Figure 4-27 for sensor 1258.

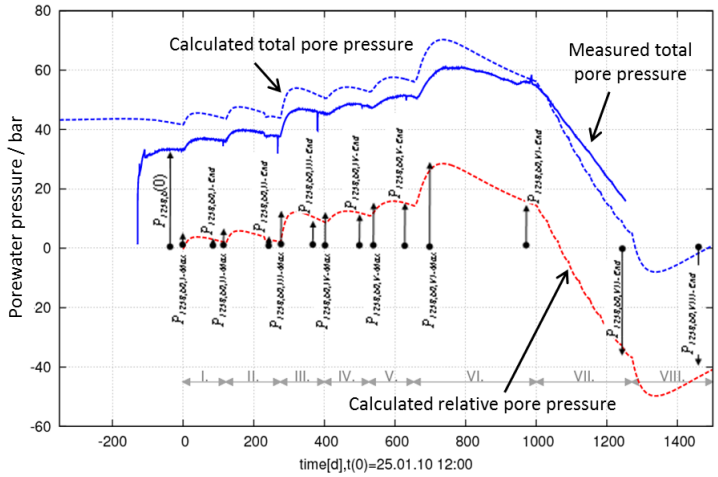

Fig. 4-27: Example of used response values for sensor 1258

For parameter identification the following objective function was defined, with N being the sensor number (Vymlatil & Schlegel, 2013):

$$\Phi = \sum_{i \in N} \Phi_{125i,Int} + \sum_{i \in N} \Phi_{125i,Max} + \sum_{i \in N} \Phi_{125i,End} \qquad N = \{1,2,3,5,8,9\} \tag{4-15}$$

The first term represents the integral differences within each phase defined as:

$$\Phi_{125i,Int} = \sum_{Ph \in S_{Int}} \Psi_{125i,Int,Ph} \Phi_{125i,Int,Ph} \qquad S_{Int} = \{\text{I, II, III, IV, V, VI, VII, VIII}\} \tag{4-16}$$

The second term represents the peak values within each heating phase defined as:

$$\Phi_{125i,Max} = \sum_{Ph \in S_{Int}} \Psi_{125i,Max,Ph} \Phi_{125i,Max,Ph} \qquad S_{Max} = \{\text{I, II, III, IV, V, VI}\} \tag{4-17}$$

The third term represents the end values within each heating phase defined as:

$$\Phi_{125i,End} = \sum_{Ph \in S_{End}} \Psi_{125i,End,Ph} \Phi_{125i,End,Ph} \qquad S_{End} = \{\text{I, II, III, IV, V, VI, VII, VIII}\} \tag{4-18}$$

The difference equations for all Φ-terms are listed in tables A2.1 to A2.3 in appendix 2. The longer the heater test runs, the smaller are the disturbing influences on the sensor signals due to the prior excavations. This means that the prognosis quality increases with each new heating phase. To take this into consideration, weighting factors ψ were introduced for each phase. Their values are listed in tables A2.1 to A2.3 in appendix 2.

The "best design" of the parameter identification represents the smallest value of the objective function Φ with regard to equations 4-15 to 4-18. For illustration, the difference values and integral difference values used in the objective function are shown in Figure 4-28.

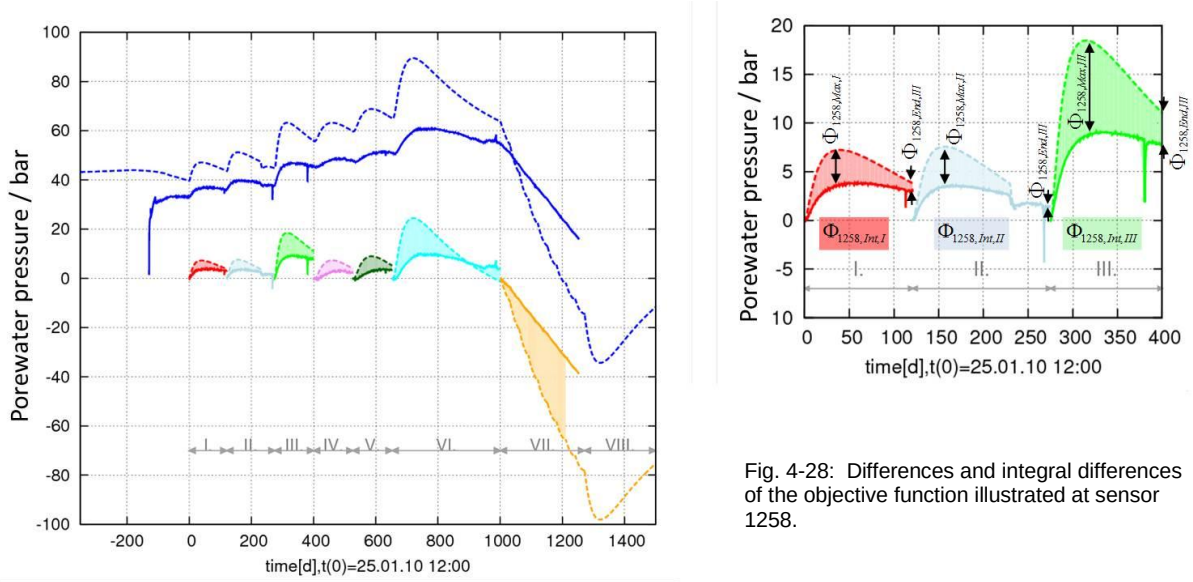

Fig. 4-28: Differences and integral differences of the objective function illustrated at sensor 1258.

Parameter analysis

The aim of the parameter analysis was to investigate the dependencies and correlations between input and response values. Another aim was to identify the most suitable range within which the individual input values of a parameter should be varied and to analyse the corresponding range of the response values. An additional advantage of this kind of sensitivity analysis is the possibility to evaluate the model quality. This means that the results indicate whether the system behaviour is adequately represented by the model and thus by the constitutive laws applied.

For the sensitivity analysis, a total amount of 80 simulation runs ("designs") were performed. The input parameters for the sensitivity analysis are listed in table 4-11. The response parameters used are described above. Table 4-12 gives an overview about all relevant parameters and their individual importance for the explanation of the sensor readouts expressed as "Coefficient of Prognosis (CoP)" (Most & Will, 2011). All parameters identified as relevant were selected as variable parameters for the parameter identification process. Looking at table 4-12, it becomes clear that at t=0 (start of heating), the following parameters are of major importance:

Perm_N_p and *Perm_K_0_p*	(Parameters of the permeability function, eq. 4-11)
cg and *phig*	(Cohesion and friction angle of the clay rock matrix)
M	(Biot-modul)

During the heating phases, the following parameters became more important:

n	(Porosity)
Alpha_f_fact	(Factor of thermal fluid expansion)
Perm_N_n and Perm_K_0_n	(Parameters of the permeability function, eq. 4-11)

Taking sensor 1251 as an example, it can be seen that the porewater pressure increase at the beginning of each heating phase is significantly influenced by porosity and fluid expansion; i.e., by coupled TH effects. The subsequent decrease in the pore pressure seems significantly influenced by the mechanical parameters cohesion and friction angle. This indicates that the decrease in pore pressure is mainly controlled by stress and permeability changes and corresponding drainage, which justifies the use of the new implemented stress-dependant permeability function.

Tab. 4-12: Bedeutsamkeit der einzelnen Parameter für die Simulationsergebnisse in den einzelnen Phase an den einzelnen Sensoren (CoP-Matrix).

	Alpha	M	Alpha_s	n	Alpha_1_fact	Perm_K_max_eppl	Perm_K_eppl	Perm_N_n	Perm_K_0_n	Perm_N_p	Perm_K_0_p	Sigd1Fact	Cr1Fact	PhirFact	Sigd1	C1	E_p	E_n	PR_p	PR_np	G_np	Phig	Psig	Cg	Sigt	Phir1Fact	CrFact	SigtrFact	Phi1	Total	
AbsPress1251_0	2%	2%								10%	2%			4%							2%	27%		26%		9%	4%		3%	90%	TED1251
RelPress1251_I_Max	2%	6%		38%	11%		1%		1%	12%	3%			1%								5%		7%		2%	2%			93%	
RelPress1251_I_End				11%	5%		4%			6%		3%							2%	2%				3%			5%			42%	
RelPress1251_II_Max	1%	10%		36%	12%		2%			12%	2%					1%				1%		3%		4%		1%	3%			87%	
RelPress1251_II_End		3%		19%	3%		4%		1%	5%						2%											13%			49%	
RelPress1251_III_Max		7%		37%	10%		2%			12%	3%							1%				5%		7%		2%	3%		1%	91%	
RelPress1251_III_End		1%	1%	29%	5%		1%			22%	4%											1%		2%			9%			75%	
RelPress1251_IV_Max	3%	5%		37%	9%		1%			11%	2%							2%				3%		4%		1%	7%			85%	
RelPress1251_IV_End	2%	2%	1%	30%	5%					19%	4%							1%				2%				1%	8%			77%	
RelPress1251_V_Max	3%	5%		34%	7%					17%	3%							1%				5%		4%		3%	3%		1%	86%	
RelPress1251_V_End	3%	3%	1%	31%	5%					23%	4%							1%				2%				2%	4%			81%	
RelPress1251_VI_Max	2%	4%		31%	7%					16%	4%							1%				9%		6%		5%	4%		2%	89%	
RelPress1251_VI_End	4%	4%		24%	4%					18%	4%										3%					3%	7%			69%	
RelPress1251_VII_End				14%	4%					21%	5%			2%								18%		17%		7%	4%		1%	94%	
RelPress1251_VIII_End				8%	3%					29%	6%			2%								17%		18%		7%	4%		1%	92%	
AbsPress1252_0	2%	3%								50%	11%			1%							1%	9%		9%		3%	1%		1%	92%	TED1252
RelPress1252_I_Max	7%	12%	1%	43%	13%					11%	2%							2%				2%		2%						94%	
RelPress1252_I_End		3%		22%	5%		2%			16%												9%		10%		4%	4%			76%	
RelPress1252_II_Max	2%	5%		34%	10%					24%	3%							1%				2%		4%		1%	1%			89%	
RelPress1252_II_End		3%		25%	8%					17%												3%		7%		3%	7%			75%	
RelPress1252_III_Max	2%	4%		35%	11%					31%	6%											1%		2%			1%			93%	
RelPress1252_III_End		2%		29%	8%		1%			36%	6%											2%		4%			2%			88%	
RelPress1252_IV_Max	2%	4%		33%	10%					31%	5%							1%				1%		2%			2%			92%	
RelPress1252_IV_End	1%	2%		30%	7%					37%	6%					0%		1%				2%		2%			3%			91%	
RelPress1252_V_Max	2%	3%		35%	9%					34%	6%							1%						2%			1%			93%	
RelPress1252_V_End	1%	2%		31%	6%					41%	7%					1%								1%		0%	2%			93%	
RelPress1252_VI_Max	2%	2%		31%	8%					41%	8%							0%						1%						94%	
RelPress1252_VI_End	2%	2%		31%	8%					37%	7%							1%								1%			2%	91%	
RelPress1252_VII_End				21%	6%					53%	12%											1%		2%						95%	
RelPress1252_VIII_End				12%	4%					60%	14%											2%		3%						95%	
AbsPress1253_0	3%	3%					1%			43%	9%			1%							1%	13%		12%		5%	2%		2%	93%	TED1253
RelPress1253_I_Max	5%	12%		42%	13%					12%	2%							2%				2%		2%			1%			93%	
RelPress1253_I_End		2%		25%	3%		3%			21%	2%					1%	1%							5%			6%			70%	
RelPress1253_II_Max	3%	8%		40%	10%		1%			19%	3%							1%				1%		2%			2%			90%	
RelPress1253_II_End		5%		30%	4%		2%			16%	2%	2%				2%		3%						4%			5%		3%	78%	
RelPress1253_III_Max	3%	6%		37%	10%		1%			28%	5%							1%						2%			1%			94%	
RelPress1253_III_End		2%		27%	5%					42%	8%							1%						3%			2%		2%	90%	
RelPress1253_IV_Max	2%	4%		34%	8%					33%	7%							1%						3%			2%		1%	94%	
RelPress1253_IV_End	1%	3%		28%	6%					40%	7%							2%						2%			2%		2%	92%	
RelPress1253_V_Max	2%	3%		31%	7%					37%	7%							1%						2%			2%		1%	94%	
RelPress1253_V_End	1%	3%		26%	6%					40%	8%							2%						2%		1%	3%		1%	94%	
RelPress1253_VI_Max	2%	3%		30%	8%					40%	9%							1%				1%		2%					1%	95%	
RelPress1253_VI_End	3%	4%		27%	6%					40%	7%							2%								1%	2%			91%	
RelPress1253_VII_End				17%	5%					54%	12%											3%		4%		1%				95%	
RelPress1253_VIII_End				9%	3%					59%	13%											4%		6%		2%	1%			95%	
AbsPress1255_0		2%							1%	52%	13%			1%				1%			1%	8%		7%		3%	1%		3%	91%	TED1255
RelPress1255_I_Max	54%	14%								1%				1%				4%		4%	4%	5%		8%		1%				92%	
RelPress1255_I_End				13%	4%					16%	2%			2%								15%		18%		4%				74%	
RelPress1255_II_Max				12%	4%					15%	2%			2%				1%				14%		17%		4%	3%			74%	
RelPress1255_II_End				14%	6%					29%	4%											7%		10%		3%	5%			79%	
RelPress1255_III_Max	2%	6%		25%	9%					16%	2%			2%				1%				6%		9%		1%	3%			83%	
RelPress1255_III_End	1%	4%		22%	8%					27%	4%							1%				5%		7%		2%	4%			85%	
RelPress1255_IV_Max	2%	4%		29%	10%		1%			30%	5%			1%								3%		4%			2%			91%	
RelPress1255_IV_End	1%	2%		26%	7%		1%			40%	7%											2%		3%			2%			91%	
RelPress1255_V_Max	2%	3%		29%	8%					38%	8%											1%		2%			1%			93%	
RelPress1255_V_End	1%	2%		24%	6%					47%	9%											1%		2%			1%			94%	
RelPress1255_VI_Max	3%	4%		31%	9%		1%			40%	8%													1%						95%	
RelPress1255_VI_End	1%	1%		24%	6%					55%	11%							0%												96%	
RelPress1255_VII_End	7%	14%		44%	13%					2%												4%		3%						88%	
RelPress1255_VIII_End	1%	5%		37%	11%					25%	6%											3%		3%						91%	
AbsPress1258_0	7%	12%		4%	1%			7%	34%	6%	2%						2%	8%				4%		1%		2%			2%	91%	TED1258
RelPress1258_I_Max	5%	8%		40%	13%					23%	6%													1%						96%	
RelPress1258_I_End	1%			36%	11%			1%	6%	30%	8%											2%		2%		1%	1%			96%	
RelPress1258_II_Max	3%	5%		40%	12%				2%	26%	7%											1%		1%						96%	
RelPress1258_II_End				35%	11%			1%	6%	28%	6%											2%		2%		0%	1%			96%	
RelPress1258_III_Max	4%	6%		41%	12%				1%	28%	6%													1%						96%	
RelPress1258_III_End	1%	2%		38%	11%				4%	32%	7%											1%		1%						96%	
RelPress1258_IV_Max	3%	5%		45%	13%				3%	22%	5%											1%		1%						96%	
RelPress1258_IV_End	2%	2%		42%	12%				5%	26%	6%											1%		1%						96%	
RelPress1258_V_Max	3%	5%		47%	13%				3%	20%	5%											1%		1%						96%	
RelPress1258_V_End	2%	3%		41%	12%			1%	5%	25%	6%													1%						96%	
RelPress1258_VI_Max	5%	8%		48%	13%				2%	17%	4%							1%												96%	
RelPress1258_VI_End	1%	1%		40%	11%			1%	7%	27%	6%											1%								96%	
RelPress1258_VII_End	6%	15%		40%	11%					22%	5%																			97%	
RelPress1258_VIII_End		2%		35%	10%				2%	41%	9%																			98%	
AbsPress1259_0		5%		12%	3%			5%	18%	19%	5%						5%	9%				3%					1%		2%	85%	TED1259
RelPress1259_I_Max	3%	9%		42%	12%				1%	22%	6%																			96%	
RelPress1259_I_End				34%	10%			1%	8%	36%	10%																			96%	
RelPress1259_II_Max	2%	4%		37%	12%				4%	32%	9%																			97%	
RelPress1259_II_End				31%	10%				9%	39%	10%																			96%	
RelPress1259_III_Max	2%	5%		38%	12%				2%	31%	8%																			97%	
RelPress1259_III_End	2%	2%		35%	10%				3%	37%	9%																			97%	
RelPress1259_IV_Max	3%	4%		40%	11%				2%	30%	8%																			97%	
RelPress1259_IV_End	2%	3%		38%	11%				3%	32%	8%																			97%	
RelPress1259_V_Max	3%	5%		40%	12%				2%	29%	7%																			97%	
RelPress1259_V_End	3%	3%		39%	11%				3%	32%	8%																			97%	
RelPress1259_VI_Max	4%	6%		42%	12%					23%	6%																			96%	
RelPress1259_VI_End	2%			37%	11%				5%	33%	8%																			96%	
RelPress1259_VII_End	17%	37%		10%	4%			2%	19%									2%		2%	1%								1%	94%	
RelPress1259_VIII_End	7%	17%		38%	10%					20%	3%																			94%	

CoP = 0%

0% < CoP < 5%

5% ≤ CoP < 10%

10% ≤ CoP < 20%

20% ≤ CoP < 40%

40% ≤ CoP < 60%

60% ≤ CoP < 80%

80% ≤ CoP < 100%

For measurement points 1258 and 1259, which are located far from the heaters, the most important parameters are the factors of the permeability function and the porosity; i.e., only the hydraulic parameters. The mechanical parameters, which are listed on the right side of the table, are of almost no importance. This is plausible as at this distance, the thermally induced stresses and thus the mechanical impacts are not as significant as in direct vicinity of the heaters, as can be seen at sensor 1251. Generally, the high values of the total CoP of normally more than 85% listed in the rightmost column of table 4-12, underpins the high representativeness of the constitutive model used to simulate the main THM-coupled processes in the clay rock.

The main goal of the parameter identification process was to find a best fit between the simulation results and the measured values of the pore pressure at the different sensor locations. An evolutionary optimization tool implemented in the optiSlang software was used to identify the so-called “best design” or the best parameter set. Prior to optimization, a parameter reduction was performed by using only input parameters with COPs > 5%. Thus, the final reduced variable space has 13 uncertain parameters (see Table 4-13). It should be noted that the reduction to parameters showing significant sensitivity to response values, which are used in the objective function, is very important. For insensitive parameters, any optimizer would choose only arbitrary values because they will not have significant influence on the objective function.

With this variable parameter set a best fit was obtained for all sensor readout analysed during the heating test. The input parameters of the “best design” are listed in table 4-13. All parameters not listed in Table 4-13 were considered to be constant and listed in tables A2.4 to A2.6 in appendix 2. For illustration, the anisotropic stress dependencies of the permeability are shown in Figure 4-29. The curves have been calculated using the new quation 4-11.

Tab. 4-13: Input parameter of the best design

Input parameter		Name	Best Design
Elastic parameter (transversal Isotropy)	E_n (Pa)	*E_n*	5.111E+09
Friction angle (rock matrix)	φ_g (°)	*Phig*	22.38
Cohesion (rock matrix)	c_g (Pa)	*Cg*	4.033 E+06
Coefficient of residual strength (rock matrix)	$\varphi_{gr,fact}$ (-)	*PhirFact*	0.627
	$c_{gr,fact}$ (-)	*CrFact*	0.313
Parameter of permeability function	$k_{0,p}$ (m^2)	*Perm_K_0_p*	4.9475e-19
	n_p (-)	*Perm_N_p*	1.0627
	$k_{0,n}$ (m^2)	*Perm_K_0_n*	1.25e-20
	n_n (-)	*Perm_N_n*	0.1682
Thermal expansion factor (fluid)	$\alpha_{f,factor}$ (-)	*Alpha_f_fact*	0.97
Porosity	n (-)	*n*	0.129
Biot-Modul	M (Pa)	*M*	3.639E+09
Biot-coefficient	α (-)	*Alpha*	0.723

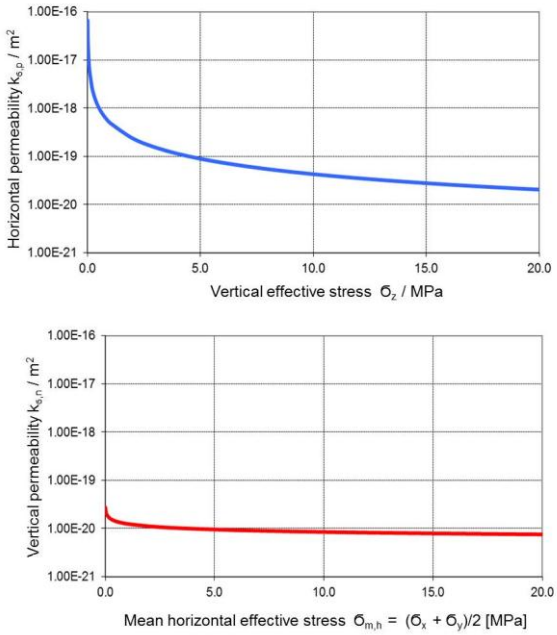

Fig. 4-29: Vertical and horizontal permeabilities depending on stress (best design)

As an example, figures 4-30 and 4-31 show a comparison between the measured values and the simulation results based on the best design for sensor 1252, which is between two heaters and sensor 1240.1, which is located next to the three heaters (Fig. 4-26). A comparison of all other sensors is given in (Schlegel & Vymlatil, 2013).

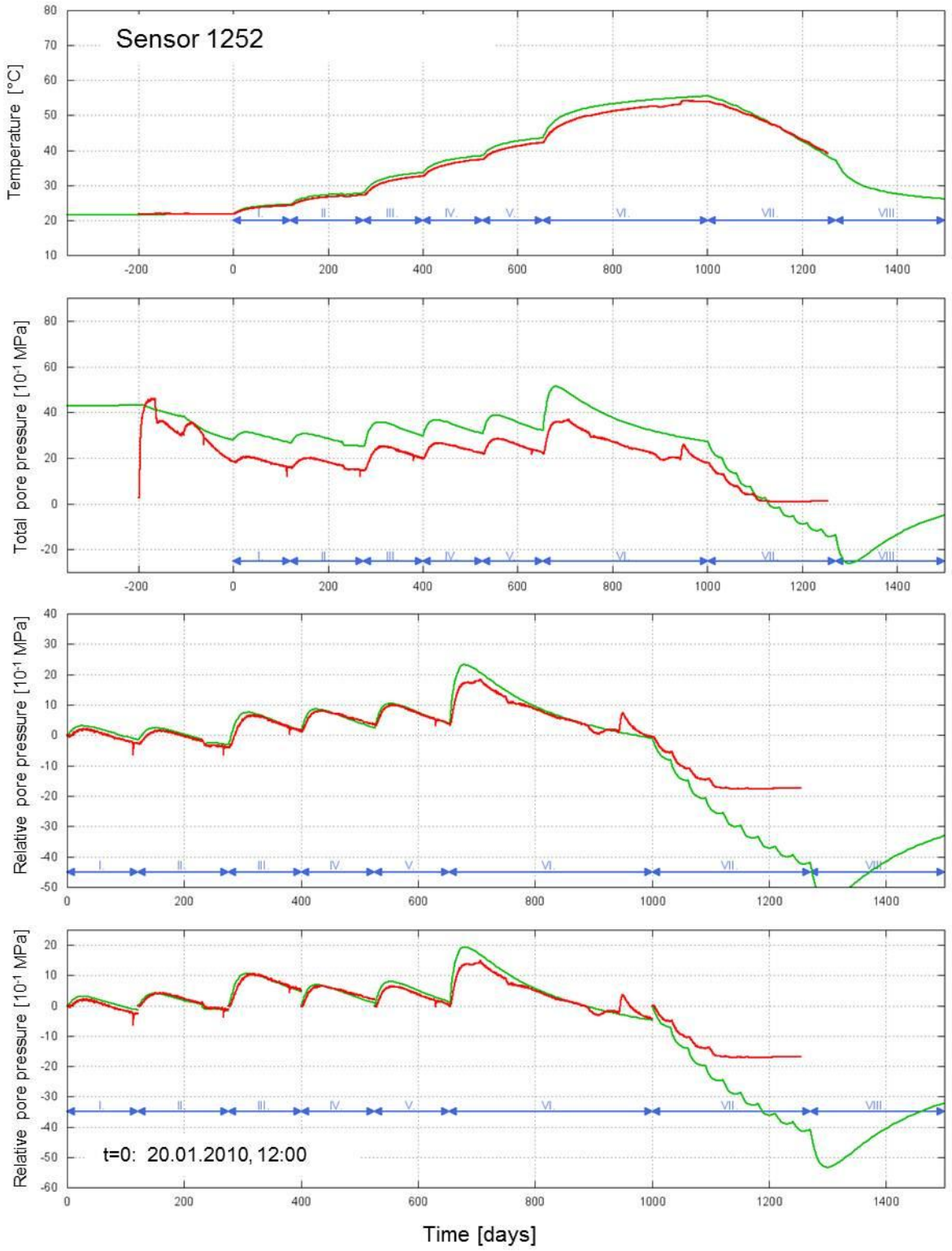

Fig. 4-30: Comparison of measured and simulated values of sensor 1252 regarding temperature, pore pressure, and relative pore pressure related to the individual heating phases.

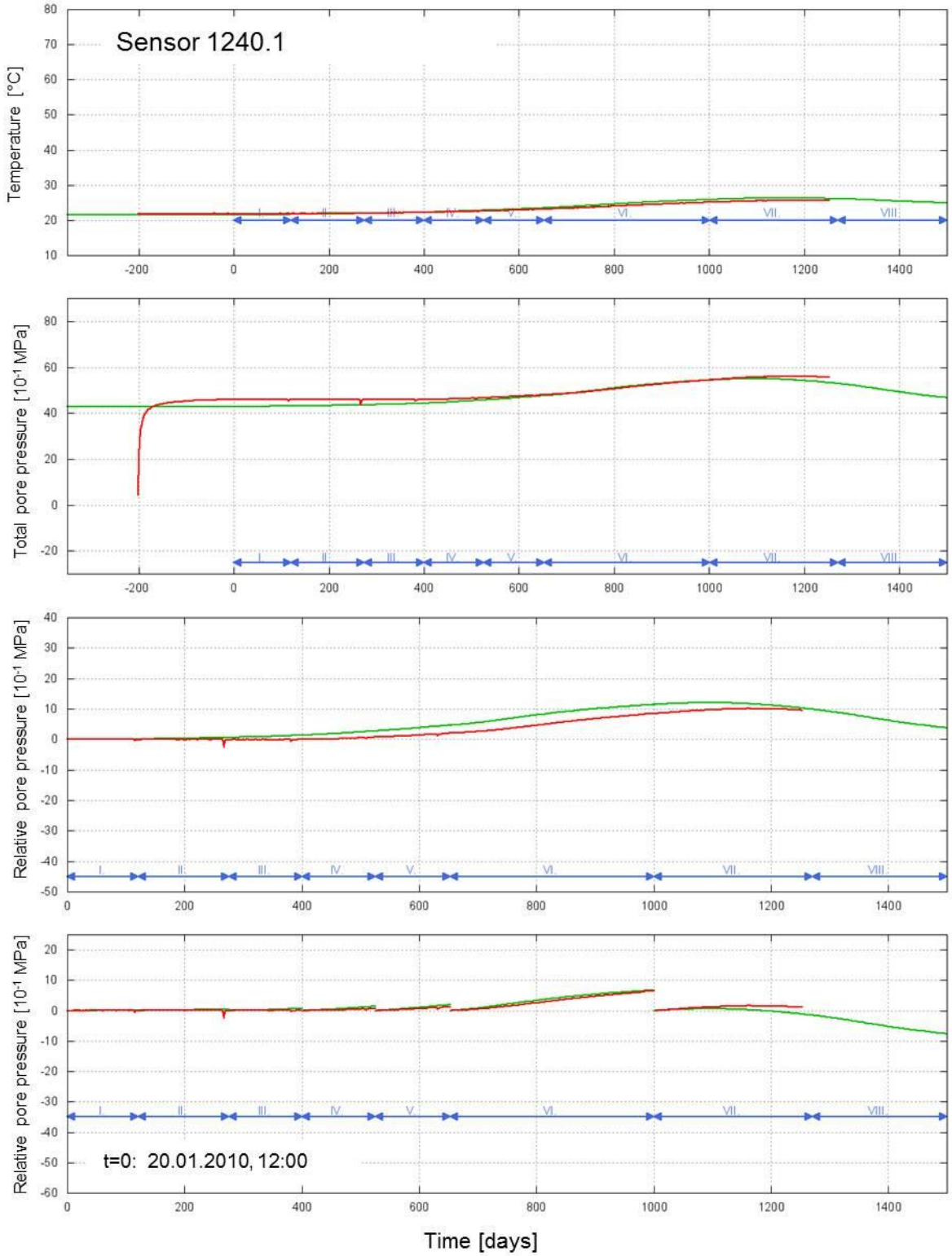

Fig. 4-31: Comparison of measured and simulated values of sensor 1240.1 regarding temperature, pore pressure, and relative pore pressure related to the individual heating phases.

The comparison shows that the simulation results meet the relative pore water pressure values normalized to the start of the heating phases. This means that the thermally induced effects are well represented in the numerical model. The good fit of the measured and simulated relative pore pressures also indicates that both, the pore pressure increase at the

beginning of the heating phases as well as the changing gradients of pore pressure decrease at the end of each phase can be reproduced. It should be noted that at sensor 1252, the measured total pore pressure during the cooling phase does not go below zero, which is due to sensor limitations. The negative pore pressures in the simulation results seem to be plausible. Drainage was induced due to thermal pore water expansion and thus increasing hydraulic gradient. Cooling after drainage led to low-pressure resulting in suction. Looking at the fitting quality in figures 4-30 and 4-31, it should be noted that there are still some remaining deviations. Since the optimum fit to all sensor readouts has already been found, any improvement of fitting quality of a single sensor would decrease the fitting quality of all the other sensor readouts. Looking at the CoP values given in table 4-12, it can be stated that the system behaviour in general can be explained to about 85%, which is very good.

Figure 4-32 shows the distribution of pore pressure and plastic strains in the test area after 1000 days of heating. The pore pressure distribution reflects well the high pressurized area in direct vicinity of the heater and the low pressure area next to the gallery indicating the main drainage direction toward the gallery. With regard to the plastic strains, it can be stated that the plastified areas around the openings (boreholes and gallery) are limited to the direct vicinity of the openings even after about three years of heating.

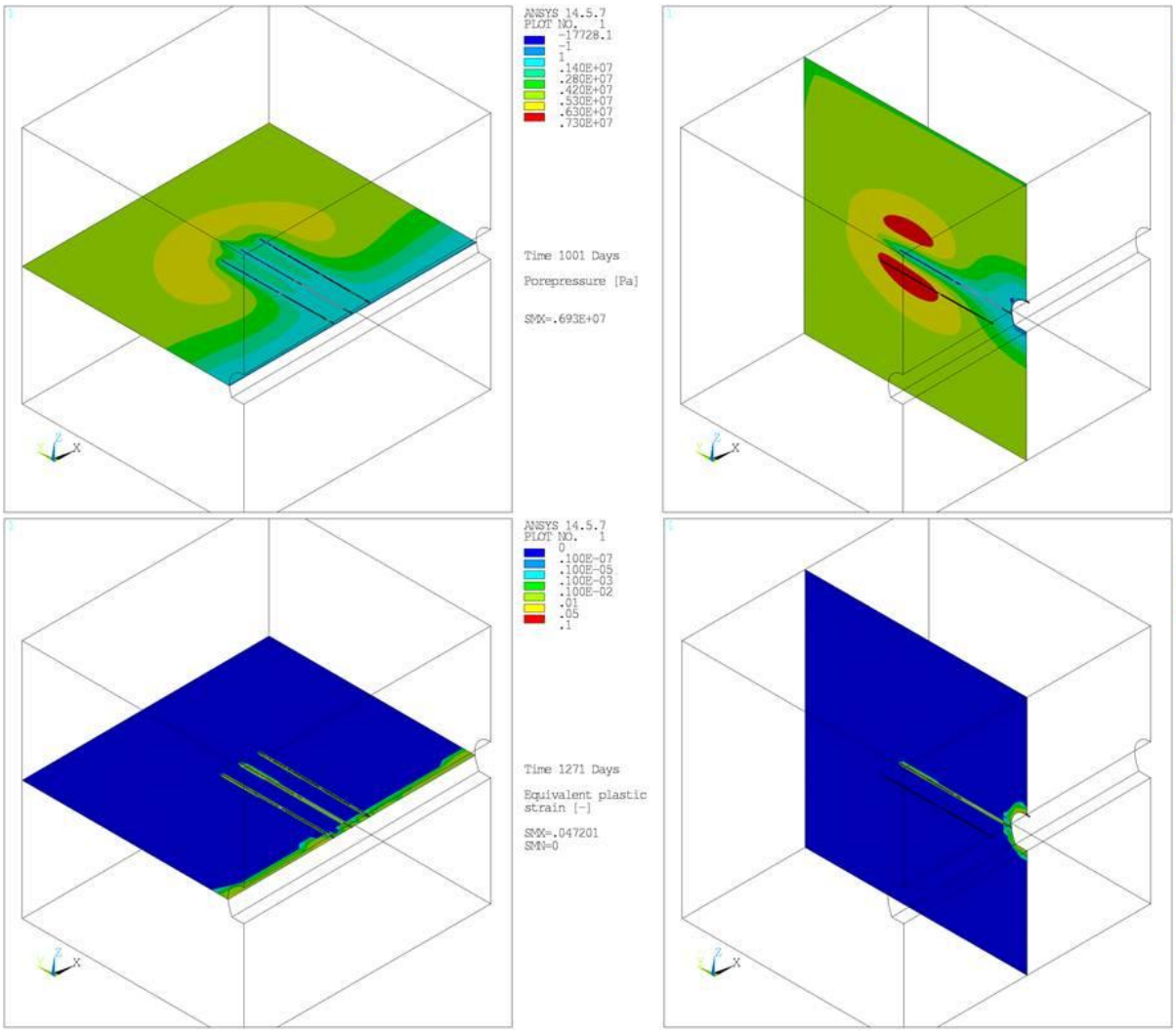

Fig. 4-32: Distribution of pore pressure and plastic strains after 1000 days, at the end of the heating phases.

Figure 4-33 illustrates the evolution of the rock permeability at two observation points in the numerical model. The temperature evolution leads to an increase in the plastic strains, which

results in a permeability increase calculated with equation 4-11. The permeability increase is significant indicating a strong impact on the hydraulic system next to the heaters.

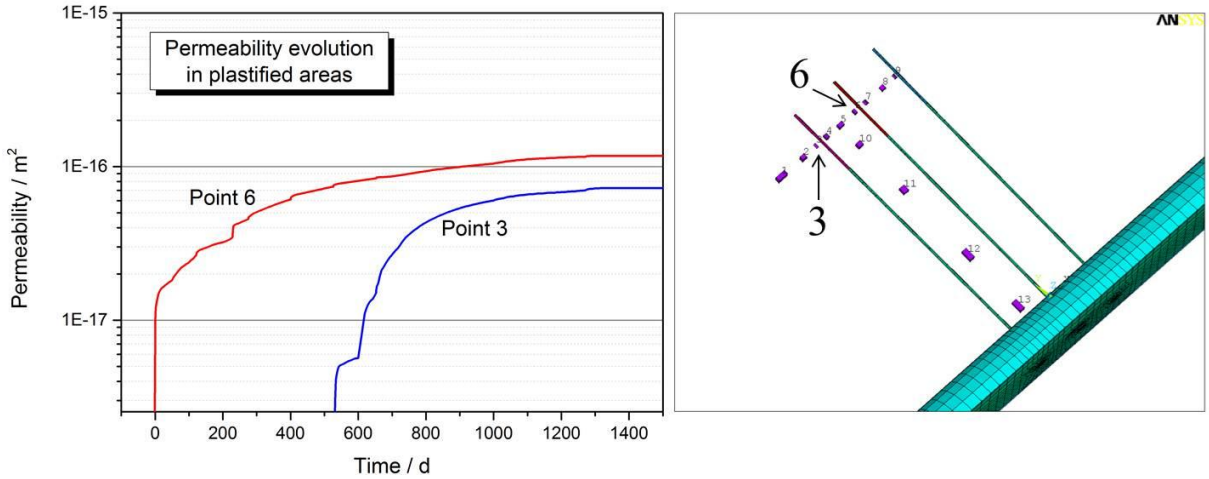

Fig. 4-33: Permeability evolution at two observation points in the plastified areas around the heaters due to increasing plastic strains.

The horizontal and vertical permeabilities obtained from this kind of parameter identification are plotted in Figure 4-34 for the observation points shown in Figure 4-33. The increased horizontal permeabilities due to the heating at the observation points in the plastified areas around the heaters are plotted as well for comparison (pink values). The location of the heaters related to the location of the observation points are illustrated by green lines. The corresponding mean values are written next to the curves. These mean values are in good agreement with the in-situ permeability measurements performed by ANDRA. This indicates that the hydraulic system is adequately described by the model. It should be noted that the permeability increase due to increasing plastic strains cover a range of about three orders of magnitude, which is a large range.

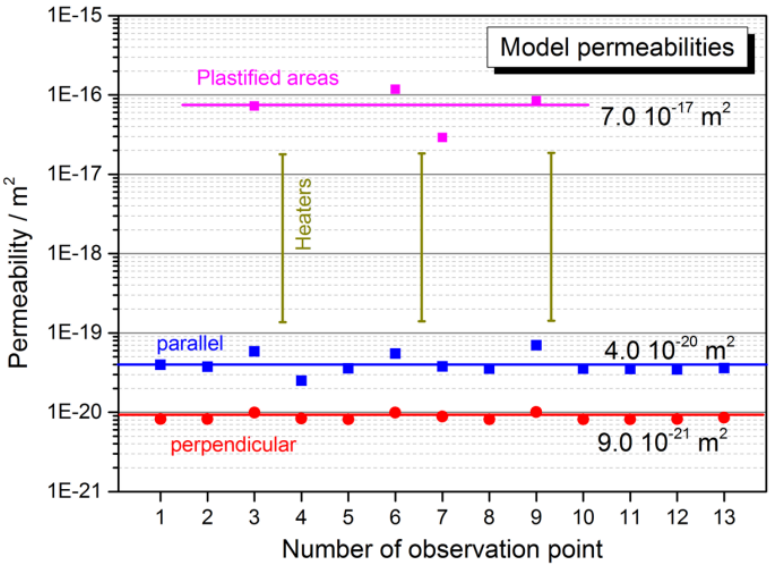

Fig. 4-34: permeabilities identified parallel and perpendicular to the bedding and in plastified areas.

With regard to the inhomogeneous initial condition of the heater test that could not be represented by the model and the remaining uncertainties about installation of technical equipment, especially the sensor contacts to the rock mass, the comparison of the measured and simulated time series of temperature and (relative) porewater pressure showed that the model developed and the constitutive laws applied are suited to simulate the observed coupled THM physical processes and thus the host rock behaviour in response to an artificial heating.

5 Conclusions

Buffer investigations

The thermal conductivity of bentonite was investigated in the laboratory by preparing samples of bentonite with different admixtures. It could be demonstrated that the admixtures used are able to increase the thermal conductivity of a buffer material in case there is a need for a better heat dissipation in the disposal concept.

In addition to thermal effects, the mechanical stress effects due to the swelling of the bentonite were investigated using numerical simulations. Two kinds of constitutive laws for the swelling were tested in order to analyse the stress evolution within the TBT experiment at the Äspö URL. With one of them, a parameter set could be identified that allows the simulation of the radial stresses within a realistic range observed in the experiment and that can be regarded as a sufficient assessment of the stress within the experiment. However, the axial stresses still show contradictions. In addition to measurement uncertainties, one reason could be the disturbing effects from the adjoining Canister Retrieval Test, which could not be taken into account in the numerical analysis. No unequivocal sensitive parameters for the entire model could be defined. Reasons could be an insufficient number of parameter sets or, more probable, an incomplete consideration of all physical effects or disturbances in the numerical model. This still needs further investigation.

Finally, a discrete element mechanical material model for bentonite was developed. The parameter for the particles and their bond behaviour were calibrated so that the macroscopic mechanical properties of a particle assembly are similar to a real sample.

EDZ investigations

Opalinus clay samples were artificially damaged in order to analyse the permeability evolution during fissure closing. A continuous decrease in permeability was determined during increase in confining pressure, and a mathematical expression was identified in terms of a potential function. The permeability reduction was roughly two orders of magnitude down to a confining pressure of 3 MPa. In contrast to this, a decrease in confining pressure did not result in an increase in permeability indicating a sealing process of the cracks during pressurization.

In parallel to this, a permeability-effective porosity relationship for the Opalinus clay was developed based on the theory of fractals, which allows the description of rock mass properties using fractal dimensions. This relationship links the geometric pore size parameters, the fractal dimension, and the permeability of a material. A calibration for Opalinus clay was obtained by analysing permeability and effective porosity measurements of artificially cracked samples as described above. For these cracked Opalinus clay samples, a fractal dimension of D=2.80 was obtained, which is similar to previous determinations of D for fractured rock mass. The permeability-porosity relation was applied to the EDZ of a vertical 50-m-deep emplacement borehole in Opalinus clay at a German generic repository site. The necessary geometric size parameters were calculated using the PFC computer code. The calculated permeabilities varied between 10^{-17} m^2 and 10^{-13} m^2, with a mean of $1.7 \cdot 10^{-14}$ m^2, which is in line with previous in-situ determinations of Opalinus clay permeabilities in the EDZ around a drift at the Mont Terri rock laboratory. The aim of the work presented here was to demonstrate a methodology for calculating permeabilities from the pore size parameters and fractal dimension of fissured rock mass.

Host rock investigations

A temperature increase due to disposed of radioactive waste would generally accelerate metamorphic processes. As an example, the most reactive process, i.e., the illitisation of smectites upon temperature increase has been investigated. It was found that the influence

on illitisation reactions is negligible since the temperature and particularly the time span of higher temperatures is too small.

With regard to organic compounds in the clay host rock, the extent to which the heat released by the waste canisters artificially accelerates maturing and, thus, oil formation has been investigated. The results show that the increase in maturing would be far below measurable limits and needs not be considered in a safety analysis.

Quantifiable conclusions about the retention properties of claystones at increased temperatures are drawn from experimentally determined values about the sorption behaviour of elements or radionuclides. The results show that, if the temperature of the claystone increases, sorption for europium, nickel, and the trivalent transuranic elements can be expected to increase. A decrease in sorption capacity can only be expected for caesium. All in all, it can be said that the sorption capacity and, thus, the retention capacity increase with increasing temperatures.

With regard to hydro-mechanical effects, a mine-by test performed at the Mt. Terri rock laboratory has been analysed using numerical simulations. The results show that the chosen modelling approach captures the in-situ observed effects quite well. The pore pressure evolution, namely the onset and rate of pressure increase as well as the rapid pore pressure decrease, is in good accordance to in-situ observations. Nevertheless, the magnitude of maximum pore pressure is overestimated by the model. This is assumed to be most likely due to earlier beginning fracture-initiation in-situ prior to modelling. The modelling approach assuming lower rock stiffness is able to reproduce the elastic rock response. But even assuming low strength behaviour of the rock, the remaining plastic deformation after stress release is still slightly underestimated by the model.

The analysis of the heater test at the Meuse/Haute-Marne URL was aimed at identifying physical rock parameters. The anisotropic thermal and hydraulic parameters obtained are in good agreement with the results of laboratory and in-situ measurements. The new implemented constitutive law allowed a suitable description of the permeability evolution in direct vicinity of the heater boreholes. It can be stated that the system behaviour in general can be explained to about 85%, which is very good. The comparison of the measured and simulated time series of temperature and porewater pressure showed that the model developed and the constitutive laws applied are suited to simulate the observed THM-coupled physical processes and thus the host rock behaviour in response to an artificial heating.

6 References

Akesson, M. (2012). *Temperature Buffer Test.* Technical Report, SKB and Clay Technology.

Andra. (2005). *Dossier 2005: Andra research on the geological disposal of high-level long-lived radioactive waste – Results and perspectives.* Tech. rep., ANDRA.

Archie, G. (1942). The electrical resistivity log as an aid in determining some reservoir characteristics. *Trans. AIME (Amer. Inst. Min. Met. Engrs.), 146*, 54-61.

Bagde, M., Raina, A., & Chakraborty, A. J. (2002). Rock mass characterization by fractal dimension. *Engineering Geology, 63*, 141-155.

Bastiaens, W., F., B., & Li, X. (2007). SELFRAC: Experiments and conclusions on fracturing, self-healing and self-sealing processes in clays. *Physics and Chemistry of the Earth, 32*, 600-615.

Billaux, D. (2009). *Damage around a canister under heating.* Technical Report, Itasca, Ecully.

Billaux, D., Dedecker, F., & Cundall, P. (2004). A novel approach to studying rock damage: the three dimensional Adaptive Continuum/Discontinuum Code. In Schubert (Hrsg.), *Final Proc. EUROCK 2004 & 53rd Geomechanics Colloquium VGE*, (S. 723-728).

Blümling, P., Bernier, F., Lebon, P., & Martin, D. (2007). The excavation damaged zone in clay formations, time-dependent behaviour and influence on performance assessment. *Physics and Chemistry of the Earth, 32*, 588-599.

Bock, H. (2008). *RA Experiment: Updated Review of the Rock Mechanics Properties of the Opalinus Clay of the Mont Terri URL based on Laboratory and Field Testing.* Technical Report, QS Consult.

Börgesson, L., Johannesson, L.-E., Sanden, T., & Hernelind, J. (1995). *Modelling of the physical behaviour of water saturated clay barriers; laboratory tests, material models and finite element applications.* Tech. rep., SKB.

Bossart, P., Trick, T., Meier, P., & Mayor, J. (2004). Structural and hydrogeological characterisation of the excavation-disturbed zone in the Opalinus Clay (Mont Terri Project, Switzerland). *Applied Clay Science, 26*, 429-448.

Buehler, C., Heitz, D., Trick, T., & Frieg, B. (2003). In-situ self-healing of the EDZ as a consequence of loading. - Impact of the Excavation Disturbed or Damaged Zone (EDZ) on the performance of radioactive waste geological repositories. *Proc of a European Commission CLUSTER conference*, (S. 231-236). Luxemburg.

Buntebarth, G. (2009). *Thermophysikalische Messungen an Tonstein-Kernproben aus Messbohrungen.* Tech. rep., Geophysikalisch-Technisches Büro, Clausthal-Zellerfeld.

Carman, P. (1956). *Flow of gases through porous media.* Butterworth Scientific Publication.

Conil, N., Armand, G., Garitte, B., Jobmann, M., Jellouli, M., Fillipi, M., et al. (2012). In situ heating test in the Callovo Oxfordian clay : Measurement and interpretation. *Clays in Natural and Engineered Barriers for Radioactive Waste Confinement, 5th International meeting, Montpellier, France.*

Cundall, P., & Strack, O. (1979). A discrete numerical model for granular assemblies. *Geotechnique, 29*(1), 47-65.

Davy, C., Skoczylas, F., Barnichon, J., & Lebon, P. (2007). Permeability of macro-cracked argillite under confinement - Gas and water testing. *Physics and Chemistry of the Earth, 32*, 667-680.

Dedecker, F., Cundall, P., Billaux, D., & Groeger, T. (2006). Evaluation of damage-induced permeability using a three-dimensional Adaptive Continuum/Discontinuum Code (AC/DC). *Physics and Chemistry of the Earth*.

Deutloff, O., Teichmüller, M., Teichmüller, R., & Wolf, M. (1980). Inkohlungsuntersuchungen im Mesozoikum des Massivs von Vlotho im Niedersächsischen Tektogen. *N. Jb. Geol. Paläont. Mh., 6*, 321-341.

DGED (1985). Indirekter Zugversuch an Gesteinsproben - Spaltzugversuch. Techn. Prüfvorschriften für Boden und Fels im Straßenbau TP BF-StB, Teil C10, Empfehlung Nr. 10. *Indirekter Zugversuch an Gesteinsproben - Spaltzugversuch. Techn. Prüfvorschriften für Boden und Fels im Straßenbau TP BF-StB, Teil C10, Empfehlung Nr. 10(10)*.

Garitte, B., Vaunat, J., Gens, A., & Armand, G. (March 29 2010). 3D Interpretation of an in-situ heating test in the Callovo-Oxfordian mudstone. *Clays in Natural & Engineered Barriers for Radioactive Waste Confinement, Nantes, France.*

Grob, H. (1972). Schwelldruck im Belchentunnel. *Proc. Int. Symp. für Untertagebau, Luzern, S. 99-119*, (S. 99-119).

Häfner, F., Kornjaew, A., Pohl, A., & Voigt, H. (1996). Permeabilitäts- und Porositätsmessungen an Gesteinsproben mit dem instationären Zweikammerverfahren. *Erdöl Erdgas Kohle, 112(10)*, 401-404.

Huang, W., Longo, J., & Pevear, D. (1993). An experimentally derived kinetic model for smectite-to-illite conversion and its use as a geothermometer. *Clays Clay Miner, 41*, 162-177.

IbeWa (2011). *Bestimmung der Gaspermeabilität von Formsteinproben für veränderliche Fließwege - Endbericht.* Messbericht, IbeWa.

Itasca (2005). *FLAC3D Manuals.*

Jobmann, M., & Billaux, D. (2010). Fractal model for permeability calculation from porosity and pore radius information and application to excavation damaged zones surrounding waste emplacement boreholes in opalinus clay. *International Journal of Rock Mechanics \& Mining Sciences, 47*, 583-589.

Jobmann, M., & Buntebarth, G. (2009). Influence of graphite and quartz addition on the thermo–physical properties of bentonite for sealing heat-generating radioactive waste. *Applied Clay Science, 44*, 206-210.

Jobmann, M., & Polster, M. (2007). The response of Opalinus clay due to heating – a combined analysis of in-situ measurements, laboratory investigations and numerical calculations. *Clay in natural and engineered barriers for radioactive waste confinement, Conference Proceedings, Tours, France.*

Jobmann, M., Amelung, P., & Uhlig, L. (2007). *Berechnungen von Paläotemperaturen und Vitrinitreflexionen im Niedersächsischen Becken und die Anwendung dieser Methodik auf generische Endlager.* Tech. rep., DBE TECHNOLOGY.

Jobmann, M., Amelung, P., & Uhlig, L. (2007). *Untersuchungen zur sicherheitstechnischen Auslegung eines generischen Endlagers im Tonstein in Deutschland - GENESIS - Anlagenband Geologie der Referenzregionen im Tonstein.* Tech. rep., DBE TECHNOLOGY.

Jobmann, M., Pöhler, M., & Polster, M. (2009). Thermomechanische Auslegung und Entwicklung eines Referenz-Endlagerkonzeptes zur Einlagerung wärmeentwickelnder radioaktiver Abfälle im Tonstein in Deutschland. *Bergbau, 12*.

Jobmann, M., Wilsnack, T., & Voigt, H.-D. (2010). Investigation of damage-induced permeability of Opalinus clay. *International Journal of Rock Mechanics \& Mining Sciences, 47*, 279-285.

Johannesson, L. (2008). *Backfilling and closure of the deep repository – Phase 3 pilot test to verify engineering feasibility, Geotechnical investigations made on unsaturated backfill materials.* Tech. rep., SKB.

Katz, A., & Thompson, A. (1984). Fractal sandstone pores, implications for conductivity and pore formation. *Physical Review Letters, 54*(12).

Konietzky, H. (2000). *Entwicklung einer Berechnungsroutine für Quellen für das Programm FLAC.* interner bericht, Itasca.

Kozeny, J. (1927). Über die kapillare Leitung des Wassers im Boden - Aufstieg, Versickerung und Anwendung auf die Bewässerung. *Sitz. Ber. Akad. Wiss. Wien, Mat. Nat. (Abt. IIa), 136a*, 271-306.

Liu, C., Zachara, J., Qafoku, O., & Smith, S. (2003). Effect of temperature on Cs sorption and desorption in subsurface sediments at the Hanford Site, USA. *Environ. Sci. Technol., 37*, 2640-2645.

Mandelbrot, B. (1977). *Fractals - form, chance and dimensions.* Freeman.

Mathier, J., Egger, P., & Descoeudres, F. (1999). *Sondierbohrung Benken. Felsmechanische Untersuchungen an Bohrkernen (Teil 2).* Tech. rep., NAGRA.

Mengel, K. (2006). *Einfluss der Temperaturerhöhung auf die mineralogischen und anorganisch-chemischen Eigenschaften von Kreide-Tonformationen (Apt).* Tech. rep., TU Clausthal.

Millard, A., Rejeb, A., Chijimatsu, M., Jing, L., De Jonge, J., Kohlmeier, M., et al. (2005). Numerical study of the THM effects on the near-field safety of a hypothetical nuclear waste repository—BMT1 of the DECOVALEX III project. Part 2: Effects of THM coupling in continuous and homogeneous rocks. *International Journal of Rock Mechanics \& Mining Sciences, 42*, 731-744.

MolTech. (2008). Molecular Technology 2008. World of crystals, Crystal quartz (SiO2) and Fused Silica. *Molecular Technology 2008. World of crystals, Crystal quartz (SiO2) and Fused Silica*.

Most, T., & Will, J. (2011). Sensitivity analysis using the Metamodel of Optimal Prognosis. *Sensitivity analysis using the Metamodel of Optimal Prognosis*.

Nagra (2002). *Projekt Opalinuston, Synthese der geowissenschaftlichen Untersuchungsergebnisse.* Tech. rep., NAGRA.

Narasimhan, T. (2006). Coupled equations for transient water flow, heat flow,and deformation in hydrogeological systems. *J. Earth Syst. Sci, 115*(2), 219-228.

Pacovsky, J., Svoboda, J., & Zapletal, L. (2007). Saturation development in the bentonite barrier of the Mock-Up-CZ geotechnical experiment. *Physics and Chemistry of the Earth, 32*, 767-779.

Pape, H., & Schopper, J. (1987). Fractal description of the Falkenberg granite micro-fissure system as derived from petrophysical and microscopical investigations. *Geol. Jb., E39*, 149-166.

Pape, H., & Schopper, J. (1988). *Relations between physically relevant geometrical properties of a multi-fractal porous system.* (K. Unger, Hrsg.) Elsevier.

Pape, H., Clauser, C., & Iffland, J. (1999). Permeability prediction based on fractal pore-space geometry. *Geophysics, 64*, 1447-1460.

Pape, H., Clauser, C., & Iffland, J. (2000). Variation of permeability with porosity in sandstone diagenesis interpreted with a fractal pore space model. *Pure and Applied Geophysics, 157*, 603-619.

Pape, H., Riepe, L., & Schopper, J. (1981). Transactions of the 7th European Logging Symposium, Paris. *Communications, 17*, 1-11.

Pape, H., Riepe, L., & Schopper, J. (1982). A pigeonhole model for relating permeability to specific surface. *The Log Analyst: Errata: The Log Analyst 23 No. 2: 50 ff., 23*(1 and 2), 5-13.

Pape, H., Riepe, L., & Schopper, J. (1983). Paper 20. *Proceedings of the RILEM/CNR International Symposium, Milan.*

Pape, H., Riepe, L., & Schopper, J. (1984). The role of fractal quantities as specific surface and tortuosities for physical properties of porous media. *Particle Characterization*, *1*, S. 66-73.

Pape, H., Riepe, L., & Schopper, J. (1987). Interlayer conductivity of rocks, a fractal model of interface irregularities for calculating interlayer conductivity of natural porous mineral systems. *Colloids and Surfaces, 27*, 97-122.

Pape, H., Riepe, L., & Schopper, J. (1987). Theory of self-similar network structures in sedimentary and igneous rocks and their investigation with microscopical and physical methods. *Journal of Microscopy, 184*, 121-147.

Popp, T., Salzer, K., & Minkley, W. (2008). Influence of bedding planes to EDZ-evolution and the coupled THM properties of Opalinus Clay. *Physics and Chemistry of the Earth, 33*, 5374-5387.

Pytte, A., & Reynolds, R. (1989). The thermal transformation of smectite to Illite. In *Naer MC \& McCulloh, T.H. (eds.): Thermal History of Sedimentary Basins, Chapter 8:133-140.* Springer, New York.

Rautioaho, E., & Korkiala-Tanttu, L. (2009). *Betomap: Survey of bentonite and tunnel backfill knowledge, State-of-the-art.* VTT Working Papers, VTT Technical Research Centre of Finland.

Schirmer, S. (2013). *Numerical simulation of a biaxial and a uniaxial compression test (Brazilian Test) to determine material parameters using the discrete element method.* internal Report, DBE TECHNOLOGY GmbH.

Studer, J., Amman, W., Meier, P. M., & Glauser, E. (1984). *Verfüllen und Versiegeln von Stollen, Schächten und Bohrlöchern, Band 1 + Band 2 Anhänge.* Tech. rep., Nagra.

Sweeney, J. J., & Burnham, A. K. (1990). Evaluation of a Simple Model of Vitrinite Reflectance Based on Chemical Kinetics. *American Association of Petroleum Geologists Bulletin, 74*, 1559-1570.

Sweeney, J., & Burnham, A. (1989). A chemical kinetic model of vitrinite maturation and reflectance. *Geochimica et Cosmochimica Acta, 53*, 2649-2657.

Tertre, E., Berger, G., Castet, S., Loubet, M., & Giffaut, E. (2005). Experimental sorption of Ni, Cs and Ln onto a montmorillonite up to 150°C. *Geochimica et Cosmochimica Acta, 69*(21), 4937-4948.

Tertre, E., Berger, G., Simoni, E., Castet, S., Giffaut, E., Loubet, M., et al. (2006). Europium retention onto clay minerals from 25 to 150°C: Experimental measurements, spectroscopic features and sorption modelling. *Geochimica et Cosmochimica Acta, 70*, 4563-4578.

Vasièek, R. (2007). *Impact of admixtures on thermal properties of bentonite.* unpublished.

Vietor, T., Armand, G., Nyonoya, S., Schuster, K., & Wieczorek, K. (2010). Excavation induced damage evolution during a mine-by experiment in Opalinus clay. *Clays in natural and engineered barriers for radioactive waste confinement, 4th international meeting, Nantes, France.*

Vymlatil, P., & Schlegel, R. (2013). *Parameteridentifikation für thermisch-hydraulisch-mechanisch gekoppelte Berechnungen eines Erhitzerversuches.* Technischer Bericht, Dynardo, Weimar.

Waples, D. (1980). Time and Temperature in Petroleum Formation: Application of Lopatin's Method to Petroleum Exploration. *The American Association of Petroleum Geologists Bulletin, 64*(6).

Wileveau, Y., Su, K., & Ghoreychi, M. (2007). A heating experiment in the argillites in the Meuse/Haute-Marne underground research laboratory. *11th International Conference on Environmental Remediation and Radioactive Waste Management (ICEM2007).*

Will, J. (2006). The Calibration of Measurement and Simulation as Optimization Problem. *NAFEMS Seminar: „Virtual Testing – Simulationsverfahren als integrierter Baustein einer effizienten Produktentwicklung.*

Yildizdag, K., Herklotz, M., Jobmann, M., Polster, M., Schonebeck, M., & Uhlig, L. (2008). *Investigation on the THM Behavior of a Heated Bentonite Barrier by Measurements and Numerical Calculations - MUSTER -.* Tech. rep., DBE TECHNOLOGY.

Zhang, C., Rothfuch, T., Dittrich, J., & Müller, J. (2008). *Investigations on self-sealing of indurated clay, part of the NF-PRO project.* Final Report, GRS.

Appendix 1

Table A1.1: Input parameters and their ranges

No	Parameter	Optislang-name	Initial value	Variation [%]	range	
					lower bound	upper bound
1	Density Bentonite	bento_dens	2000	5	1900	2100
2	Density Granite	granit_dens	2750		2613	2888
3	Density Sand	sand_dens	1800		1710	1890
4	Density Sand filter	sandfil_dens	1800		1710	1890
5	Young's Modulus Bentonite	bento_young	4.70E+09	50	1.00E+08	7.05E+09
6	Young's Modulus Granite	granit_young	5.50E+10		2.75E+10	8.25E+10
7	Young's Modulus Sand	sand_young	5.54E+07		2.77E+07	8.31E+07
8	Young's Modulus Sand filter	sandfil_young	5.54E+07		2.49E+07	8.31E+07
9	Fixed pore pressure boundary Sand 1	fixpp1	7.00E+05		2.00E+05	7.00E+05
10	Fixed pore pressure boundary Sand 2	fixpp2	2.00E+05		2.00E+05	7.00E+05
11	Fixed pore pressure boundary Sand 3	fixpp3	2.00E+05		2.00E+05	7.00E+05
12	Fixed pore pressure boundary Sand 4	fixpp4	2.00E+05		2.00E+05	7.00E+05
13	Fixed pore pressure boundary Sand 5	fixpp5	2.00E+05		2.00E+05	7.00E+05
14	Fixed pore pressure boundary Sand 6	fixpp6	2.00E+05		2.00E+05	7.00E+05
15	Fixed pore pressure boundary Sand 7	fixpp7	2.00E+05		2.00E+05	7.00E+05
16	Grob's Law: Maximum Swelling Deformation	MaxQuellDef	0.05	50	0.025	0.075
17	Grob's Law: Maximum Swelling Pressure	MaxQuellDruck	2.20E+07		1.10E+07	3.30E+07
18	Grob's Law: Parameter	GrobParam	-0.005		-0.0075	-0.0025
19	Intrinsic Permeability Bentonite1	bento1_int_perm	2.53E-19	20	4.83E-23	1.00E-18
20	Intrinsic Permeability Bentonite2	bento2_int_perm	3.19E-19		6.38E-23	1.00E-18
21	Intrinsic Permeability Sand	sand_int_perm	1.00E-18		2.51E-22	1.00E-18
22	Intrinsic Permeability Sand filter	sandfil_int_perm	1.00E-18		2.51E-22	1.00E-18
23	Porosity Bentonite1	bento1_poro	0.389	50	0.195	0.584
24	Porosity Bentonite2	bento2_poro	0.368		0.184	0.552
25	Porosity Sand	sand_poro	0.300		0.150	0.450
26	Porosity Sand filter	sandfil_poro	0.360		0.180	0.540
27	Specific Heat Capacity Bentonite	bento_spec_heat	1091	20	873	1309
28	Specific Heat Capacity Granite	granit_spec_heat	775		620	930
29	Specific Heat Capacity Sand	sand_spec_heat	900		720	1080
30	Specific Heat Capacity Sand filter	sandfil_spec_heat	900		720	1080
31	Thermal Expansion Coefficient Bentonite	bento_thexp	3.00E-05	20	2.40E-05	3.60E-05
32	Thermal Expansion Coefficient Granite	granit_thexp	7.00E-06		5.60E-06	8.40E-06
33	Thermal Expansion Coefficient Sand	sand_thexp	1.20E-05		9.60E-06	1.44E-05
34	Thermal Expansion Coefficient Sand filter	sandfil_thexp	1.20E-05		9.60E-06	1.44E-05
35	Heat Conductivity Bentonite	bento_wleitf	1.30	20	1.04	1.56
36	Heat Conductivity Granite	granit_wleitf	2.60		2.08	3.12
37	Heat Conductivity Sand	sand_wleitf	1.70		1.36	2.04
38	Heat Conductivity Sand filter	sandfil_wleitf	1.70		1.36	2.04

Table A1.2: Sensors considered in the objective function (Goudarzi, 2008)

Temperature	Axial stress	Radial stress
TB208	PB201	PB202
TB230	PB208	PB204
TB247	PB214	PB213
TB261	PB218	PB215
TB283	PB227	PB217
		PB226
		PB228

Table A1.3: Model parameter Sensitivity 2, highlighted in red are changes to the first analysis.

No	Parameter	optislang-name	Initial value	Variation [%]	range	
					lower bound	upper bound
1	Young's modulus Bentonite	bento_young	4.70E+09	50	1.00E+08	7.05E+09
2	Young's modulus Granite	granit_young	5.50E+10		2.75E+10	8.25E+10
3	Young's modulus Sand	sand_young	5.54E+07		2.77E+07	8.31E+07
4	Young's modulus Sand filter	sandfil_young	5.54E+07		2.49E+07	8.31E+07
5	Fixed pore pressure boundary Sand 1	fixpp1	7.00E+05		2.00E+05	7.00E+05
6	Fixed pore pressure boundary Sand 2	fixpp2	2.00E+05		2.00E+05	7.00E+05
7	Fixed pore pressure boundary Sand 3	fixpp3	2.00E+05		2.00E+05	7.00E+05
8	Fixed pore pressure boundary Sand 4	fixpp4	2.00E+05		2.00E+05	7.00E+05
9	Fixed pore pressure boundary Sand 5	fixpp5	2.00E+05		2.00E+05	7.00E+05
10	Fixed pore pressure boundary Sand 6	fixpp6	2.00E+05		2.00E+05	7.00E+05
11	Fixed pore pressure boundary Sand 7	fixpp7	2.00E+05		2.00E+05	7.00E+05
12	Grob's Law: Maximum Swelling Deformation	MaxQuellDef	0.05	50	0.025	0.075
13	Grob's Law: Maximum Swelling Pressure	MaxQuellDruck	1.00E+06		5.00E+05	1.5E+06
14	Grob's Law: Parameter	GrobParam	-0.005		-0.0075	-0.0025
15	Intrinsic Permeability Bentonite1	bento1_int_perm	2.53E-19	20	4.83E-23	1.00E-18
16	Intrinsic Permeability Bentonite2	bento2_int_perm	3.19E-19		6.38E-23	1.00E-18
17	Intrinsic Permeability Sand	sand_int_perm	1.00E-18		2.51E-22	1.00E-18
18	Intrinsic Permeability Sand filter	sandfil_int_perm	1.00E-18		2.51E-22	1.00E-18
19	Porosity Bentonite1	bento1_poro	0.389	50	0.195	0.584
20	Porosity Bentonite2	bento2_poro	0.368		0.184	0.552
21	Porosity Sand	sand_poro	0.300		0.150	0.450
22	Porosity Sand filter	sandfil_poro	0.360		0.180	0.540
23	Specific Heat Capacity Bentonite	bento_spec_heat	1091	20	873	1309
24	Specific Heat Capacity Granite	granit_spec_heat	775		620	930
25	Specific Heat Capacity Sand	sand_spec_heat	900		720	1080
26	Specific Heat Capacity Sand filter	sandfil_spec_heat	900		720	1080
27	Thermal Expansion Coefficient Bentonite	bento_thexp	3.00E-05	20	2.40E-05	3.60E-05
28	Thermal Expansion Coefficient Granite	granit_thexp	7.00E-06		5.60E-06	8.40E-06
29	Thermal Expansion Coefficient Sand	sand_thexp	1.20E-05		9.60E-06	1.44E-05
30	Thermal Expansion Coefficient Sand filter	sandfil_thexp	1.20E-05		9.60E-06	1.44E-05
31	Heat Conductivity Bentonite	bento_wleitf	0.80	20	0.24	1.56
32	Heat Conductivity Granite	granit_wleitf	2.60		2.08	3.12
33	Heat Conductivity Sand	sand_wleitf	1.15		0.48	2.04
34	Heat Conductivity Sand filter	sandfil_wleitf	1.15		0.48	2.04
35	Saturation threshold for swelling	swell_sat	0.81		0.799	0.820

Table A1.4: Sensors considered in the objective function

Temperature	Axial stress	Radial stress
TB208	PB208	PB202
TB230	PB227	PB204
TB247		PB213
TB261		PB215
TB283		

Figure A1.1: Best design parameters

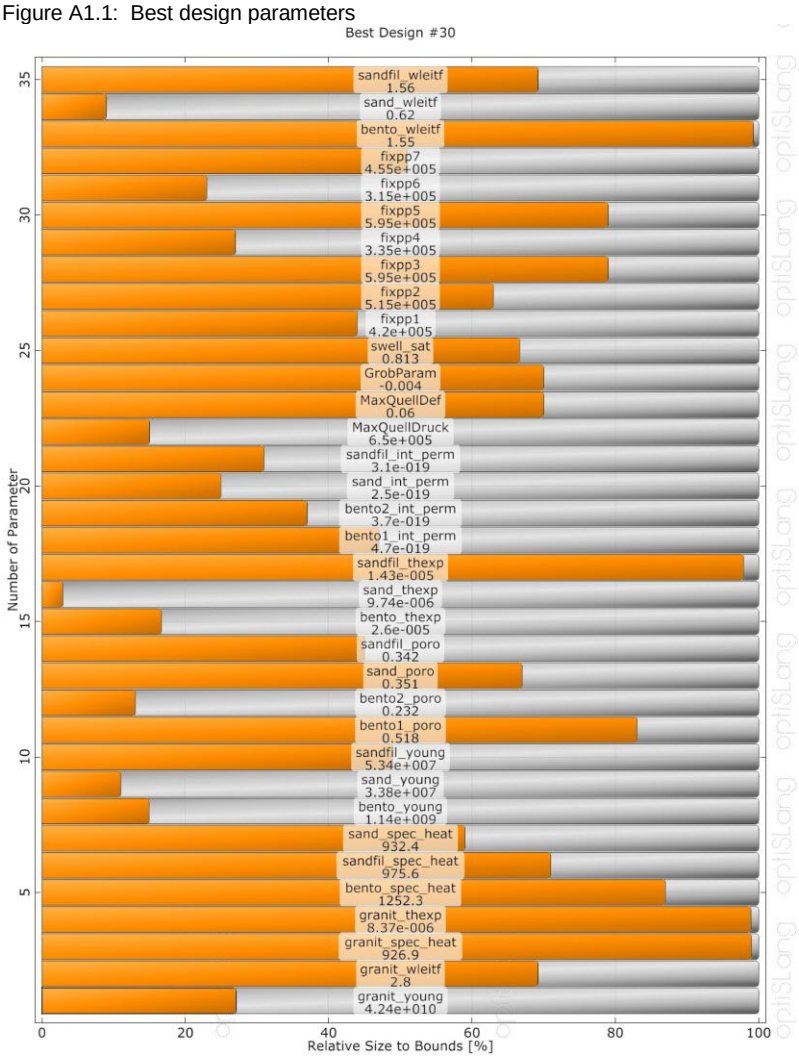

Appendix 2

Table A2.1: Integral differences at sensors 125i , i=1,2,3,5,8,9

	Phase	$\Phi_{125i,Int,Ph} =$	$\Psi_{125i,Int,Ph} =$
TEDTED 125i, für i=1,2,3,5,8,9	*I*	$=\left(\int_{0}^{121}\left\|p_{125i,m,\mathrm{I}}(t)-p_{125i,b,\mathrm{I}}(t)\right\|dt\right)/(121-0)$	=0.4 for i = 1,2,3,5,8,9
	II	$=\left(\int_{121}^{275}\left\|p_{125i,m,\mathrm{II}}(t)-p_{125i,b,\mathrm{II}}(t)\right\|dt\right)/(275-121)$	=0.6 for i = 1,2,3,5,8,9
	III	$=\left(\int_{275}^{400}\left\|p_{125i,m,\mathrm{III}}(t)-p_{125i,b,\mathrm{III}}(t)\right\|dt\right)/(400-275)$	=1.0 for i = 1,2,3,5,8,9
	IV	$=\left(\int_{400}^{526}\left\|p_{125i,m,\mathrm{IV}}(t)-p_{125i,b,\mathrm{IV}}(t)\right\|dt\right)/(526-400)$	=1.0 for i = 1,2,3,5,8 =0.4 for i = 9
	V	$=\left(\int_{526}^{653}\left\|p_{125i,m,\mathrm{V}}(t)-p_{125i,b,\mathrm{V}}(t)\right\|dt\right)/(653-526)$	=1.0 for i = 1,2,3,5,8 =0.4 for i = 9
	VI	$=\left(\int_{653}^{1001}\left\|p_{125i,m,\mathrm{VI}}(t)-p_{125i,b,\mathrm{VI}}(t)\right\|dt\right)/(1001-653)$	=1.0 for i = 1,8 =0.4 for i = 2,5 =0.0 for i = 3,9
	VII	$=\left(\int_{1001}^{End_{125i}}\left\|p_{125i,m,\mathrm{VII}}(t)-p_{125i,b,\mathrm{VIII}}(t)\right\|dt\right)/(End_{125i}-1001)$ End_{125i} = 1091 for i = 1,2,3,9 End_{125i} = 1241 for i = 5 End_{125i} = 1211 for i = 8	=1.0 for i = 1,2,3,5,8,9

Table A2.2: Peak differences at sensors 125i , i=1,2,3,5,8,9 within each heating phase

	Phase	$\Phi_{125i,Max,Ph} =$	$\Psi_{125i,Max,Ph} =$
TED 125i, für i=1,2,3,5,8,9	*I*	$=\left\|p_{125i,m,\mathrm{I}}(t_{max})-p_{125i,b,\mathrm{I}}(t_{max})\right\|$, $p_{125i,m,\mathrm{I}}(t_{max})=\max(p_{125i,m,\mathrm{I}}(t))$, for $0<t\leq 50$	0.4 for i = 1,2,3,5,8,9
	II	$=\left\|p_{125i,m,\mathrm{II}}(t_{max})-p_{125i,b,\mathrm{II}}(t_{max})\right\|$, $p_{125i,m,\mathrm{II}}(t_{max})=\max(p_{125i,m,\mathrm{II}}(t))$, for $0<t\leq 50$	0.6 for i = 1,2,3,5,8,9
	III	$=\left\|p_{125i,m,\mathrm{III}}(t_{max})-p_{125i,b,\mathrm{III}}(t_{max})\right\|$, $p_{125i,m,\mathrm{I}}(t_{max})=\max(p_{125i,m,\mathrm{I}}(t))$, for $0<t\leq 50$	1.0 for i = 1,2,3,5,8,9
	IV	$=\left\|p_{125i,m,\mathrm{IV}}(t_{max})-p_{125i,b,\mathrm{IV}}(t_{max})\right\|$, $p_{125i,m,\mathrm{I}}(t_{max})=\max(p_{125i,m,\mathrm{I}}(t))$, for $0<t\leq 50$	1.0 for i = 1,2,3,5,8 0.4 for i = 9
	V	$=\left\|p_{125i,m,\mathrm{V}}(t_{max})-p_{125i,b,\mathrm{V}}(t_{max})\right\|$, $p_{125i,m,\mathrm{I}}(t_{max})=\max(p_{125i,m,\mathrm{I}}(t))$, for $0<t\leq 50$	1.0 for i = 1,2,3,5,8 0.4 for i = 9
	VI	$=\left\|p_{125i,m,\mathrm{VI}}(t_{max})-p_{125i,b,\mathrm{VI}}(t_{max})\right\|$, $p_{125i,m,\mathrm{I}}(t_{max})=\max(p_{125i,m,\mathrm{I}}(t))$, for $0<t\leq 50$	1.0 for i = 1,8 0.4 for i = 2,5 0.0 for i = 3,9

Table A2.3: Differences at the end of each heating phase at sensors 125i , i=1,2,3,5,8,9

	Phase	$\Phi_{125i,End,Ph} =$	$\Psi_{125i,End,Ph} =$
TED 125*i*, für *i*=1,2,3,5,8,9	*I*	$= \lvert p_{125i,m,\mathrm{I}}(121) - p_{125i,b,\mathrm{I}}(121) \rvert$	0.4 for *i* = 1,2,3,5,8,9
	II	$= \lvert p_{125i,m,\mathrm{II}}(275) - p_{125i,b,\mathrm{II}}(275) \rvert$	0.6 for *i* = 1,2,3,5,8,9
	III	$= \lvert p_{125i,m,\mathrm{III}}(400) - p_{125i,b,\mathrm{III}}(400) \rvert$	1.0 for *i* = 1,2,3,5,8,9
	IV	$= \lvert p_{125i,m,\mathrm{IV}}(526) - p_{125i,b,\mathrm{IV}}(526) \rvert$	1.0 for *i* = 1,2,3,5,8 0.4 for *i* = 9
	V	$= \lvert p_{125i,m,\mathrm{V}}(653) - p_{125i,b,\mathrm{V}}(653) \rvert$	1.0 for *i* = 1,2,3,5,8 0.4 for *i* = 9
	VI	$= \lvert p_{125i,m,\mathrm{VI}}(1001) - p_{125i,b,\mathrm{VI}}(1001) \rvert$	1.0 for *i* = 1,8 0.4 for *i* = 2,5 0.0 for *i* = 3,9
	VII	$= \lvert p_{125i,m,\mathrm{VII}}(End_{125i}) - p_{125i,b,\mathrm{VII}}(End_{125i}) \rvert$ End_{125i} = 1091 for *i* = 1,2,3,9 $End_{125\,i}$ = 1241 for *i* = 5 $End_{125\,i}$ = 1211 for *i* = 8	1.0 for *i* = 1,2,3,5,8,9

Table A2.4: Thermal parameters for TED analysis

Parameter			**Value**
Claystone (Callovo-Oxfordien)			
Density	ρ	$kg \cdot m^{-3}$	2332.9
Thermal conductivity in *X* direction	λ_x	$W \cdot m^{-1} \cdot K^{-1}$	2.020
Thermal conductivity in *Y* direction	λ_y	$W \cdot m^{-1} \cdot K^{-1}$	2.020
Thermal conductivity in *Z* direction	λ_z	$W \cdot m^{-1} \cdot K^{-1}$	1.371
Specific heat capacity	c	$J \cdot kg^{-1} \cdot K^{-1}$	694.69
Shotcrete			
Density	ρ	$kg \cdot m^{-3}$	2200.0
Thermal conductivity	λ	$W \cdot m^{-1} \cdot K^{-1}$	2.000
Specific heat capacity	c	$J \cdot kg^{-1} \cdot K^{-1}$	800.00
Heater			
Density	ρ	$kg \cdot m^{-3}$	4000.0
Thermal conductivity	λ	$W \cdot m^{-1} \cdot K^{-1}$	1.600
Specific heat capacity	c	$J \cdot kg^{-1} \cdot K^{-1}$	1000.00
Air			
Density	ρ	$kg \cdot m^{-3}$	1.12
Thermal conductivity	λ	$W \cdot m^{-1} \cdot K^{-1}$	0.025
Specific heat capacity	c	$J \cdot kg^{-1} \cdot K^{-1}$	1007.00

Table A2.5: Hydraulic parameters for TED analysis

Parameter			**Value**	
Density (water)	ρ_w	kg·m^{-3}	1000.0	Mat. parameter
Dynamic viscosity (water)	μ_w	N·s·m^{-2}	Equation 4-9	
Thermal expansion coefficient (water)	α_w	1/K	**Fehler! Verweisquelle konnte nicht gefunden werden.**Equation 4-14	
Factor of the thermal expansion coefficient (water)	$\alpha_{f,factor}$	-	1.000	Mat. parameter
Claystone (Callovo-Oxfordien)				
Constants for permeability function	$k_{0,p}$	m^2	5.87E-19	Mat. parameter
	n_p	-	1.07871	Mat. parameter
	$k_{0,n}$	m^2	1.50E-20	Mat. parameter
	n_n	-	0.15363	Mat. parameter
	k_ε	m^2	9.92E-15	Mat. parameter
	$k_{\varepsilon,max}$	m^2	1.18E-16	Mat. parameter
Porosity	n	-	0.1646	Mat. parameter
Expansion coefficient (rock matrix)	α_s	1/K	1.415E-05	Mat. parameter
Biot modulus	M	Pa	3.9E9	Mat. parameter
Biot constant	α	-	0.65	Mat. parameter
Shotcrete				
Hydraulic conductivity		m·s^{-1}	3.00E-13	Mat. parameter
Specific storage coefficient		m^{-1}	1.00E-06	Mat. parameter
Heater				
Hydraulic conductivity		m·s^{-1}	3.00E-05	Mat. parameter
Specific storage coefficient		m^{-1}	1.00E-04	Mat. parameter
Air				
Hydraulic conductivity		m·s^{-1}	3.00E-05	Mat. parameter
Specific storage coefficient		m^{-1}	1.00E-04	Mat. parameter

Table A2.6: Mechanical parameters for TED analysis

Parameter			**Value**	
Claystone (Callovo-Oxfordien) – Elasticity parameters (tranversal isotropy)				
Young's modulus (horizontal)	E_p	Pa	8.230E+09	Mat. parameter
Young's modulus (vertical)	E_n	Pa	5.731E+09	Mat. parameter
Poisson's ratio (horizontal)	ν_p	-	0.3	Mat. parameter
Poisson's ratio (vertikal)	ν_{np}	-	0.3	Mat. parameter
Shear modulus (vertical)	G_{np}	Pa	2.700E+09	Mat. parameter
Claystone (Callovo-Oxfordien) - isotropic Mohr-Coulomb (strength values for rock matrix)				
Angle of friction	φ_g	°	28.79	Mat. parameter
Dilatancy angle	ψ_g	°	10.0	Mat. parameter
Cohesion	c_g	Pa	3.794+06	Mat. parameter
Tensile strength limit	σ_t	Pa	1.3E+06	Mat. parameter
Residual strength values as	$\varphi_{gr,fact}$	-	0.840	Mat. parameter

coefficients related to strength values	$c_{qr,fact}$	-	0.444	Mat. parameter
	$\sigma_{tr,fact}$	-	0.4	Mat. parameter
Claystone (Callovo-Oxfordien) - anisotropic Mohr-Coulomb (strength values for bedding)				
Angle of friction	φ_1	°	23.54	Mat. parameter
Dilatancy angle	ψ_1	°	10	Mat. parameter
Cohesion	c_1	Pa	1.5E+06	Mat. parameter
Tensile strength limit	σ_{t1}	Pa	0.5E+05	Mat. parameter
Residual strength values as coefficients related to strength values	$\varphi_{r1,fact}$	-	0.7	Mat. parameter
	$c_{r1,fact}$	-	0.4	Mat. parameter
	$\sigma_{tr1,fact}$	-	0.4	Mat. parameter
Shotcrete				
Young's modulus		Pa	40.50E+09	Mat. parameter
Poisson's ratio		-	0.20	Mat. parameter